UNIVERSITAT POLITÈCNICA
DE CATALUNYA
BARCELONATECH

Nonlinear analysis of electro-acoustic frequency-selective devices for communications

David Garcia Pastor

ADVERTIMENT La consulta d'aquesta tesi queda condicionada a l'acceptació de les següents condicions d'ús: La difusió d'aquesta tesi per mitjà del repositori institucional UPCommons (http://upcommons.upc.edu/tesis) i el repositori cooperatiu TDX (http://www.tdx.cat/) ha estat autoritzada pels titulars dels drets de propietat intel·lectual **únicament per a usos privats** emmarcats en activitats d'investigació i docència. No s'autoritza la seva reproducció amb finalitats de lucre ni la seva difusió i posada a disposició des d'un lloc aliè al servei UPCommons o TDX. No s'autoritza la presentació del seu contingut en una finestra o marc aliè a UPCommons (*framing*). Aquesta reserva de drets afecta tant al resum de presentació de la tesi com als seus continguts. En la utilització o cita de parts de la tesi és obligat indicar el nom de la persona autora.

ADVERTENCIA La consulta de esta tesis queda condicionada a la aceptación de las siguientes condiciones de uso: La difusión de esta tesis por medio del repositorio institucional UPCommons (http://upcommons.upc.edu/tesis) y el repositorio cooperativo TDR (http://www.tdx.cat/?locale-attribute=es) ha sido autorizada por los titulares de los derechos de propiedad intelectual **únicamente para usos privados enmarcados** en actividades de investigación y docencia. No se autoriza su reproducción con finalidades de lucro ni su difusión y puesta a disposición desde un sitio ajeno al servicio UPCommons No se autoriza la presentación de su contenido en una ventana o marco ajeno a UPCommons (*framing)*. Esta reserva de derechos afecta tanto al resumen de presentación de la tesis como a sus contenidos. En la utilización o cita de partes de la tesis es obligado indicar el nombre de la persona autora.

WARNING On having consulted this thesis you're accepting the following use conditions: Spreading this thesis by the institutional repository UPCommons (http://upcommons.upc.edu/tesis) and the cooperative repository TDX (http://www.tdx.cat/?locale- attribute=en) has been authorized by the titular of the intellectual property rights **only for private uses** placed in investigation and teaching activities. Reproduction with lucrative aims is not authorized neither its spreading nor availability from a site foreign to the UPCommons service. Introducing its content in a window or frame foreign to the UPCommons service is not authorized (framing). These rights affect to the presentation summary of the thesis as well as to its contents. In the using or citation of parts of the thesis it's obliged to indicate the name of the author.

UNIVERSITAT POLITÈCNICA
DE CATALUNYA

Ph.D. Thesis

NONLINEAR ANALYSIS OF ELECTRO-ACOUSTIC FREQUENCY-SELECTIVE DEVICES FOR COMMUNICATIONS

Author: David Garcia Pastor

Advisors: Juan Carlos Collado Gomez, Ph.D.
Associate Professor
Universitat Politècnica de Catalunya (UPC)

Jordi Mateu Mateu, Ph.D.
Associate Professor
Universitat Politècnica de Catalunya (UPC)

Components and Systems for Communications Research Group
Department of Signal Theory and Communications
Universitat Politècnica de Catalunya

Barcelona, December 2020

“Jardinera, tú que entraste
en el jardín de mi amor,
de las flores que tú riegas
dime cuál es la mejor.
La mejor es una rosa
que se viste de color,
del color que se le antoja,
y verde verde tiene la hoja.
Tres hojitas tiene verdes
y las demás encarnadas,
y a ti te escojo niña mía
por ser la más resalada.”

Canción de corro

“Cuentan de un sabio que un día
tan pobre y mísero estaba,
que sólo se sustentaba
de unas hierbas que cogía.
¿Habrá otro, entre sí decía,
más pobre y triste que yo?;
y cuando el rostro volvió
halló la respuesta, viendo
que otro sabio iba cogiendo
las hierbas que él arrojó.”

Pedro Calderón de la Barca

Abstract

Nowadays, mobile devices have become a key technology in our lives, making us become part of a connected world, in which millions of mobile handsets are sold every year. In order to satisfy the user demands, many mobile communication standards are working together in the same device (LTE-A, 5G-NR, IEEE Wireless LAN Standards, etc.). High data rates are demanded for different wireless services working on a very crowded frequency spectrum, where all the devices and systems need to operate at the same time without detrimental of mutual interference.

Although this major objective has to be faced from different perspectives, such as new modulations and new networking protocols, the radio frequency (RF) and microwave components, forming the communication chain in a transceiver, play a significant role on the whole system performance.

Passive devices, like filters, contribute to the signal degradation due to passive intermodulation (PIM). PIM can be generated by the lack of mismatch between metallic contacts, oxidation, or basically, by the inherent nonlinear material properties used on the fabrication of the devices. Although the impact of PIM is lower than the distortion introduced by active devices, for current wireless services and their demanding requirements, any type of nonlinear generation is certainly an issue.

Acoustic wave (AW) devices have become a fundamental technology for portable handsets supporting current wireless communication networks. Bulk Acoustic Wave (BAW) has become the main technology nowadays for high frequency filters. This technology allows a high degree of miniaturization, easily making more than 40 filters per device, and also gives other advantages as low insertion losses and multiple frequency operation. Despite these major advantages, BAW resonators exhibit a nonlinear behavior, i.e., they may suffer of intermodulation and harmonic distortion, which might become a real bottle neck for the full expansion of

the technology in the ever increasing stringent requirements.

The aim of this thesis is focused on characterizing this nonlinear limitation, quite present in acoustic resonators, by defining the origin of different nonlinear manifestations in BAW resonators, and providing new nonlinear models to reduce the computational time required to simulate those undesired effects.

The first part of this work explains the basic knowledge about acoustic propagation and piezoelectricity, presenting the linear and nonlinear constitutive equations, including the typical nonlinear manifestations appearing in those devices. Then, the typical circuit models for AW devices and, more specifically its applicability to BAW devices, is presented.

The second part of this work is focused on the nonlinear analysis of BAW resonators, by measuring different nonlinear manifestation of 8 different BAW devices, identifying the origin of the nonlinear effects and demonstrating that this unique hypothesis is consistent with those manifestations for all the measured resonators.

Resum

Avui en dia, els dispositius mòbils s'han convertit en una tecnologia clau a les nostres vides, fent-nos formar part d'un món connectat, en el qual es venen milions de telèfons mòbils cada any. Per tal de satisfer les demandes dels usuaris, molts estàndards de comunicacions mòbils treballen junts en el mateix dispositiu (LTE-A, 5G-NR, IEEE Wireless LAN Standards, etc.). Es requereixen altes velocitats de transmissió de dades per als diferents serveis de comunicació sense fils, treballant en un espectre de freqüències molt concorregut, on tots els dispositius i sistemes han de funcionar al mateix temps sense interferir-se mútuament.

Tot i que aquest objectiu principal s'ha d'afrontar des de diferents perspectives, com ara noves modulacions i nous protocols de xarxa, els components de radiofreqüència i de microones, que formen la cadena de comunicacions en un transceptor, tenen un paper important en el rendiment de tot el sistema.

Els dispositius passius, com els filtres, contribueixen a la degradació del senyal a causa de la intermodulació passiva (PIM). La PIM es pot generar per el desajust entre contactes metàl·lics, l'oxidació o, bàsicament, per les propietats no lineals inherents dels materials que s'utilitzen en la fabricació dels dispositius. Tot i que l'impacte de la PIM és inferior a la distorsió introduïda pels dispositius actius, per als serveis sense fils actuals i els seus requisits exigents, qualsevol tipus de generació no lineal és sens dubte un problema.

Els dispositius d'ona acústica (AW) s'han convertit en una tecnologia fonamental per a telèfons mòbils treballant a les xarxes de comunicació sense fils actuals. La tecnologia Bulk Acoustic Wave (BAW) s'ha convertit avui en dia en la principal tecnologia per filtres d'alta freqüència. Aquesta tecnologia permet un alt grau de miniaturització, podent fabricar més de 40 filtres per dispositiu i també ofereix altres avantatges com baixes pèrdues d'inserció i el funcionament a freqüències múltiples. Malgrat aquests avantatges, els ressonadors BAW presenten un comportament no lineal considerable, per exemple, poden sofrir generació d'intermodulació i distorsió harmònica, cosa que podria convertir-se en un autèntic coll d'ampolla per a la plena expansió de la tecnologia amb requisits, cada vegada, més estrictes.

L'objectiu d'aquesta tesi es centra en la caracterització d'aquesta limitació no lineal, força present en els ressonadors acústics, definint l'origen de diferents manifestacions no lineals en els ressonadors BAW i proporcionant nous models no lineals per reduir el temps de càlcul necessari per simular aquells efectes no desitjats.

La primera part d'aquest treball explica els coneixements bàsics sobre la propagació acústica i la piezoelectricitat, presentant les equacions constitutives lineals i no lineals, incloses les manifestacions no lineals típiques que apareixen en aquests dispositius. A continuació, es presenten els models de circuits típics per a dispositius AW i, més concretament, la seva aplicabilitat a dispositius BAW.

La segona part d'aquest treball es centra en l'anàlisi no lineal de ressonadors BAW, mesurant diferents manifestacions no lineals de 8 dispositius BAW diferents, identificant l'origen dels efectes no lineals i demostrant que aquesta hipòtesi única es consistent amb aquestes manifestacions per tots els ressonadors mesurats.

Acknowledgements

I have decided to start writing this section during one of the most difficult moments of our lives. I am confined in my home due to the COVID-19 global crisis. We are all living exceptional moments. And these moments have made me think deeply in the important things in my life.

First of all, I would like to dedicate this thesis to my parents, Jose Maria and Yolanda. Because during all their life, they have worked a lot to see how their children succeed. If now I am writing these lines, is due to all their efforts, sacrifices and their advice. Because it has not been an easy path. It has been a difficult path, with many good and bad moments. But thanks to all their support, I am closer to say: “Papa, mama, ya soy doctor”. Thanks, thanks and thanks. I have had the luck to be the son of the best parents that one could have.

Second one, I would like to dedicate these lines to my sister Noemi. Although being very different each other, we have been together during all our lives. And she has been my third fundamental pillar in my life. Thanks for being the best sister that a brother could have. And remember: “Ohana significa familia. Y la familia nunca te abandona, ni te olvida”.

Third one, and very important for me, I would like to dedicate this work to my grandparents, Victoriano, Florentina, Jose and Maria Antonia. I cannot express with words my feelings for them. Thanks for giving me all the love that a grandparent can give to his grandchild. And special thank to my two angels, you have been my stars during all this time without you, guiding me and protecting me from the sky. I love you yayo Victoriano and yaya Flores, I carry you deep in my heart.

During all my life, since one day a dog attacked me, I had panic when one of them was closer to me. But one day, when you entered home, you made me feel comfortable with you, and opened my mind with what a dog is. I would like to dedicate this thesis to Zor, my “little brother”. Because

you have given me one of the best years of my live.

Carlos Collado and Jordi Mateu, no doubt, because without their support and advice this thesis would not have been succeed. I have learned a lot from you, and you have been the best thesis advisers one could have. Thanks for giving me the opportunity of working with you in your research group, opening me the possibility to do all this work.

To Luiska, Carlos and Eric, for being the best friends one could have. We have all lived a lot of special moments, and I hope we stay together for much time. Because you have taught me what the word friendship means. To Carla and my “niece” Lia, one of the most beautiful people I have met during all my life. To Rafa and Carlos Suarez, because they have been fundamental pillars during all my university studies. Because without them, of course, nowadays I would not been writing these lines. And thanks for becoming, besides the best classmates one could have, very good friends.

To my cousins Mireia, Iker and Laia. Because sometimes, when I felt sad, you were at my side for making me smile. I will never forget our times in the beach, eating kebab or playing PS4. Because we are the granchildren of our grandparents, and we will be together all the life.

To Jose Luis, Chema, Mario, Carlos Udaondo, Marta, Jordi Hernandez and all EETAC people supporting me during all this time. I would like to thank you for all the good moments lived during this period of my life.

Finally, I want to express my gratitude to Qorvo. Inc, for making possible this Ph.D. thesis. Thanks to Dr. Robert Aigner, for all the opportunities given, and the good moments lived, specially the funny moments in Japan eating sushi and fish food.

I could continue writing a long list of people I would be grateful, so, in the end, I would like to thank all people that had gave me their support and made me smile during all my life. Thanks.

DAVID

Contents

Acronyms

ADS	Advanced Design System
AW	Acoustic Wave
AlCu	Aluminum Copper
AlN	Aluminum Nitride
BAW	Bulk Acoustic Wave
BVD	Butterworth-Van Dyke
CA	Carrier Aggregation
CSC	Components and Systems for Communications
DUT	Device Under Test
EM	Electromagnetic
FBAR	Film Bulk Acoustic Resonator
FDD	Frequency-domain Defined Device
H	Harmonic distortion
H2	Second Harmonic
H3	Third Harmonic
HB	Harmonic Balance
HPF	High Pass Filter
IEEE	Institute of Electrical and Electronics Engineers
IL	Insertion Losses
IMD	Intermodulation distortion
IMD2	Second-order intermodulation distortion
IMD3	Third-order intermodulation distortion
IDT	Interdigital Transducer

KLM	Krimtholz, Leedom and Matthaei
LAN	Local Area Network
LPF	Low Pass Filter
LTE	Long Term Evolution
MIMO	Multiple Input, Multiple Output
MUX	Multiplexer
NR	New Radio
PA	Power Amplifier
QoS	Quality of Service
RF	Radio Frequency
RL	Return Losses
SA	Spectrum Analyzer
SAW	Surface Acoustic Wave
SDD	Symbolically-Defined Devices
SMR	Solidly Mounted Resonator
Si	Silicon
SiN	Silicon Nitride
SiO_2	Silicon Dioxide
TC-BAW	Temperature Compensated Bulk Acoustic Wave
UPC	Universitat Politècnica de Catalunya
VNA	Vector Network Analyzer
W	Tungsten
WI-FI	Wireless Fidelity
ZnO	Zinc Oxide

List of Tables

List of Figures

Chapter 1

Introduction

1.1 Motivation

From wood fires, drums and pigeons to the telegraph and the mobile phone. During all their history, people have looked for different ways to communicate between them for long distances. Those different ways of communication have evolved along the years, with the purpose of transmitting some type of message in the clearer and easier way.

The first mobile phone prototype appeared in 1973. The main objective of this device, created 47 years ago, was to provide a way to speak with another person whatever the place they were, allowing the user for a 30 minute call. Nevertheless, with a weight of 1.1 Kg, dimensions of 228.6x127x44.4 mm and a battery charge procedure lasting 10 hours, these drawbacks made not suitable to manufacture this first prototype. It was not until 1984 that the first mobile phone reached the market, starting a new revolutionary way of communication. Since that day, mobile handsets have evolved very quickly over the years. Currently, besides being a way of phoning, these devices allow the user to take pictures and recording videos, surf in the internet and many other different services.

Nowadays the tendency is to cover the maximum number of wireless applications in the same device, in order to provide the best user experience. With the fast expansion of the current predominant technologies (Long Term Evolution (LTE) Advanced, IEEE wireless local area network (LAN) standards, low-power wide-area networks, and so on) and the new incoming standards (5G New Radio (NR), IEEE 802.11ax), the mobile communication requirements are more stringent than ever.

Many transceivers are coexisting inside a single mobile handset in order to cover all those services. High power transmitted signals and out-of-band transmissions can be a source of interferences for a given communication service, and consequently, can provoke losing Quality of Service (QoS) or even making impossible the signal demodulation. The jamming signals can be mixed with the high power transmitted signal of a transceiver in the antenna or in the first filtering stage (duplexer or multiplexer), provoking harmonics and/or intermodulation products that may fall at the frequency of the receiver channel. That will happen if those passive devices are even slightly nonlinear and will cause desensitization of the receiver. This effect frames into the passive intermodulation (PIM) phenomena.

Inside those frequency combinations, third-order nonlinear products are the closest to the fundamental tones, falling within the device band and degrading the QoS of the whole system.

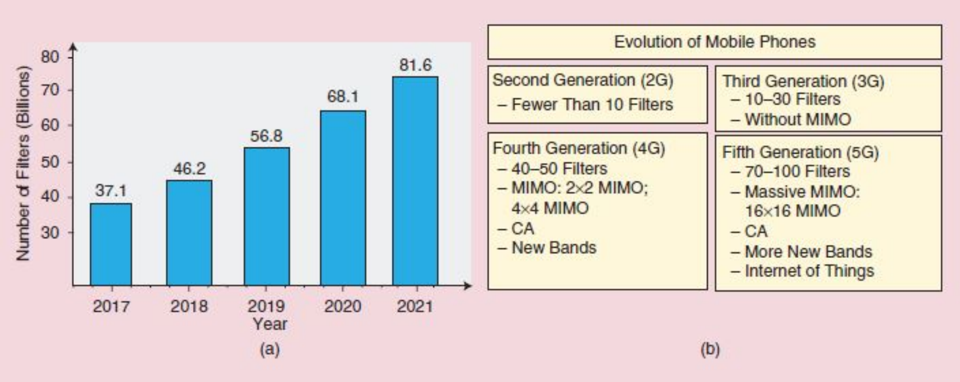

Figure 1.1: (a) Past and projected growth in the market for RF front-end filters in mobile devices from 2017 through 2021 [1]. (b) Comparison of mobile communication technologies classified according to development generations [2]. MIMO: multiple input, multiple output. [3]

The use of electromagnetic (EM) resonators has been very present in a large number of devices such filters, oscillators and tuned amplifiers. Actually, the use of these resonators is not suitable for the new devices from the point of view of integration, due to their size. In this type of resonators the size of the devices is usually directly related to the wavelength of the electromagnetic wave at a certain working frequency.

Acoustic-wave (AW) technology has been playing a crucial role on the development of the radiofrequency (RF) filtering stages of the current portable devices [4], allowing the inclusion up to 100 filters per device. With the use of acoustic resonators, the size of the devices can be reduced considerably. This type of resonators exhibits a phase velocity around five orders of magnitude lower than the electromagnetic wave velocity, due to the wave propagation in an acoustic medium. This implies that the wavelength is five orders of magnitude lower, and consequently, the size of the resonator. Figure 1.1 depicts how the number of filters sold is increasing along the years with the new incoming standards thanks to the AW technology.

There are two common configurations in order to implement electro-acoustic resonators: Bulk Acoustic Wave Resonators (BAW) and Surface Acoustic Wave Resonators (SAW). The main difference between those configurations is how the acoustic wave propagates along the piezoelectric layer, the material responsible of the electro-acoustic conversion. In SAW resonators, the acoustic wave is generated when an electric signal feeds the interdigital transducer (IDT) placed on a piezoelectric layer. This acoustic wave propagates along the surface of the piezoelectric material. In BAW resonators, the piezoelectric layer is sandwiched between two metal electrodes. When an electric field is applied to the electrodes, an acoustic wave propagating in the direction of the thickness is generated. Figure 1.2 depicts both resonator designs.

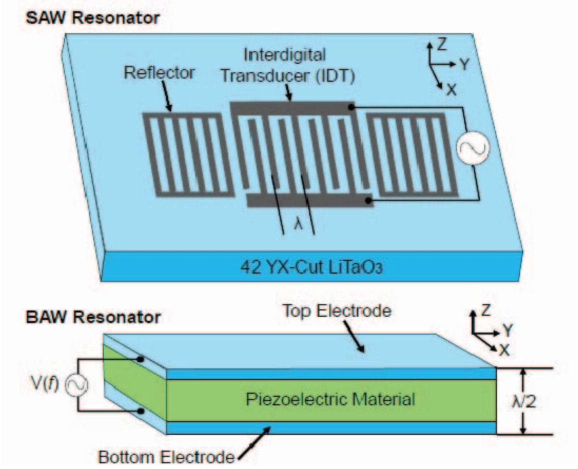

Figure 1.2: SAW and BAW resonators design [5].

Such differences on the configuration lead to difference on the operation frequency [6] and on the power handling capabilities. SAW devices due to the dependence between the fingers distance on the IDT and the wavelength of the resonant mode, can only be designed up to 2.5 GHz. At the same time, SAW resonators cannot work under high-power conditions due to the small cross-section of the fingers required for those frequencies.

Table 1.1: Comparison of SAW and BAW technology [6]

	SAW	BAW
Frequency range	up to 2.5 GHz	up to 10 GHz
Power Handling	$\sim$ 31 dBm	$\sim$ 36 dBm
Temperature Coefficient of Frequency (TCF)	-45 ppm/°C	-20 ppm/°C
Quality factor	$\sim$ 700	$\sim$ 2000
Compatibility with IC process	No	Yes

On the other hand, BAW technology is the only one that can achieve the RF filter requirements for future communication devices at higher frequencies in a reduced space. Table 1.1 depicts how BAW technology can work at higher frequencies than SAW, at the same time that offers, for example, higher power handling capacity, better Quality factor (Q) and less degree of frequency shifting with temperature changes. In conclusion, table 1.1 shows how BAW is providing better specifications for the new incoming scenarios.

But there is a drawback in their use: AW resonators are quite nonlinear devices, giving rise to intermodulation (IMD) generation and harmonic (H) distortion. Highly linear devices are required for the development and integration of the new incoming services, mitigating in this way the interferences generated in the own system. This demands full knowledge of the origin of the nonlinear sources. So, for that purpose, it is necessary the development of comprehensive nonlinear circuital models taking into account all the sources that could be potential PIM generators in BAW devices.

In the last decade, many distributed nonlinear models for BAW resonators that could be reproduced in commercial circuit simulators have been proposed. One of the first nonlinear circuital models was published in 1993 in [7]. Nevertheless, they proposed a general circuit model without identifying the origin of some nonlinearities in a given device. After that, a distributed model based on the Krimtholz, Leedom and Matthaei (KLM) model was published in 2009 [8], and it was the first distributed phenomenological approach to the nonlinear problem in a real BAW resonator. Nevertheless, this model was not able to discern between the specific origin of the nonlinear effects. The first nonlinear model based on the constitutive equations of the piezoelectric effect appeared two years later [9], [10]. This model was based on the well known Mason model, published by Warren Perry Mason in 1950 [11]. This work was extended 2 years later in [12] by including equations accounting for the thermal domain and considering thermal dependent variables into the constitutive equations.

In BAW resonators, one of the common materials used as the piezoelectric layer is Aluminum Nitride (AlN). Although those approaches used different circuital models, all of them made the assumption that the unique contributor to the nonlinear response was the AlN layer. However, those works only take into account nonlinear manifestations occurring in the vicinity of the resonant frequencies of the resonators presented, not considering nonlinear effects appearing at higher frequencies. So, full understanding of the origin of the nonlinear effects indeed requires the identification of all the sources contributing to the overall nonlinear manifestations. Later in this thesis we will detail of what we refer when mentioning overall nonlinear manifestations.

A full, comprehensive and accurate characterization of the devices to be modeled are mandatory for the success of this work. This step, crucial for the identification of the different nonlinear sources contributing to PIM generation, is not straightforward. Some aspects, such as the complexity of AW technology, and the accuracy and interpretation of the measurements, make that point difficult to deal with.

1.2 Scope of the Thesis and Structure

Scope of the thesis

The most significant limitation in terms of linearity occurring in passive BAW devices are the intrinsic nonlinear performance of the acoustic wave propagation and the self-heating effects producing desensitization of the receivers and detuning. These effects are even more harmful in some scenarios such as those using inter-band Carrier Aggregation (CA) schemes. Those techniques are common in 4G LTE-A systems and in the incoming 5G-NR, in which the different transmission and reception channels share the same antenna.

The main objective of this Ph. D. thesis is to build the foundations to find innovative solutions to reduce the current limitations in terms of linearity of the acoustic technology, in order to accelerate the design of a new generation of BAW devices and to contribute into the definition of future communication systems. Those foundations are to define comprehensive nonlinear models and to establish unique characterization methodologies.

To achieve this major objective, different sub-objectives are defined to have a clear idea of the problem to solve. These specific objectives are:

- Develop new models for the simulation of intrinsic nonlinear effects of BAW devices when they are driven by multi-tone signals, in order to reduce the complexity, and therefore, the high computational time that current models present.
- Design and implement on-wafer nonlinear measurement systems in order to measure all nonlinear manifestations of interest occurring in a BAW resonator.
- Characterize the nonlinear physical parameters (intrinsic effects) involved in the generation of PIM and harmonics to validate the developed models.
- Analyze the impact of temperature dependent nonlinear coefficients into the third-order intermodulation distortion (IMD3) response for Temperature Compensated BAW (TC-BAW) resonators.

Structure of the thesis

This thesis has been structured in five chapters.

Chapter 1 is describing a brief approach to the problem, bounding the main objectives and the scope of this doctoral thesis.

Chapter 2 introduces some fundamental concepts of piezoelectricity and acoustic propagation, which are specially relevant along the whole thesis. Then, as piezoelectric materials present a quite significant nonlinear behavior, we introduce the nonlinear constitutive equations defining these. Finally, the main effects of nonlinearities on the electrical response of those devices are discussed.

Chapter 3 describes the two fundamental linear circuital models for BAW resonators, and their main differences: the Butterworth-Van Dyke (BVD) and the Mason model. The chapter continues by presenting different nonlinear models based on those two fundamental linear models. Comparison between the different nonlinear models are presented and finally, the main advantages and drawbacks of each approach are concluded.

Chapter 4 is arranged in three different parts. The first part shows the steps required in order to do a proper nonlinear characterization procedure for AW devices. Those steps, being all of them a must in order to identify the materials involved in nonlinear generation, are carefully explained. This part also details on the measurement systems designed and assembled in order to be able to measure the different nonlinear spurious signals of a given resonator under study.

The second part starts with the nonlinear characterization procedure of eight different BAW resonators. This part focuses on the second-order nonlinearities, which are usually characterized by second harmonic (H2) generation. In particular, an accurate analysis of the contribution of each layer of the stack on the nonlinear performance is presented, by means of three different experiments: narrowband H2, broadband H2, and DC detuning. These experiments reveal a unique identification of the physical origin of the H2 generation.

The third part, tackles the third-order nonlinear manifestations, by performing a detailed characterization of third harmonic (H3) and IMD3 occurring in six different resonators. The characterization process carried out allows to identify the direct contribution and the remixing effects into the overall IMD3 and H3.

Chapter 5 outlines all the conclusions obtained during this work and the achieved goals. Finally, the future research lines are introduced.

Chapter 2

Theory of Piezoelectricity and Nonlinear Distortion

2.1 Introduction

Piezoelectricity (or piezoelectric effect) is the physical phenomena characteristic of a given material, in which, after a force or pressure is applied to it, an electric field is generated (direct piezoelectric effect). Piezoelectric materials also have the property of becoming mechanically deformed when an electric field is applied to them (inverse piezoelectric effect) [13]. The piezoelectric effect has been the one boosting the use of these materials for manufacturing electro-acoustic devices in communications. Along the last century, many books of acoustic waves in solids have been written. The main ones, and references for this chapter, are the books written by Royer [13], [14], Rosenbaum [15] and Auld [16], [17].

The aim of this chapter is to introduce some basic fundamental concepts of the acoustic propagation and the piezoelectricity, that will be specially relevant along the whole thesis. As a starting point, the one-dimensional acoustical equation of motion is presented. This equation defines how the different mechanical fields interact between them, and how an acoustic wave travels in a medium. Then, the constitutive equations that relate all the field magnitudes present in a piezoelectric material are presented. Those equations explain the amount of electrical energy transformed to acoustical energy, and the velocity of the acoustic wave propagating in the piezoelectric medium.

Since piezoelectric materials present quite significant nonlinear behavior, the constitutive equations are extended to consider the inherent nonlinear dependence between the different domains, leading to the so-called nonlinear constitutive equations [10], [18].

Finally, the main effects of nonlinearities on the electrical response of those devices are discussed , from detuning and saturation, to different “types” of PIM generation, like intrinsic direct generation, remixing effect or self-heating effects.

2.2 Constitutive Equations

2.2.1 One-dimensional Acoustical Equation of Motion

Isaac Newton published in 1687 one of the most important books in physic’s history. The book, titled *“PhilosophiæNaturalis Principia Mathematica”*, introduces three of the most relevant laws of physics, the Newton’s laws of Motion. These three laws clearly define the relation between a physical body and the different forces acting upon it.

Second Newton’s law states that a given force applied to a rigid object results in the body’s acceleration, being this movement proportional to the mass of the body

$$dF = m \cdot a. \tag{2.1}$$

As it is clearly related in [15], this external force is transmitted to all the internal parts of the body. This force causes some stress (T) in the internal structure, being this deformed. T measures the internal forces acting in the body divided by the area over which these act.

Figure 2.1 shows an isotropic volume in which two different forces are acting upon it. These two forces are represented by the stresses T and $-T$ respectively, and are defined as

$$dF = dA \cdot T, \tag{2.2}$$

where A is the area. A component T is parallel to the normal vector of the area ($\vec{A}$), this T is longitudinal.

Each T generates a mechanical wave propagating along the volume. The mechanical or acoustic propagation of this wave could be described thanks

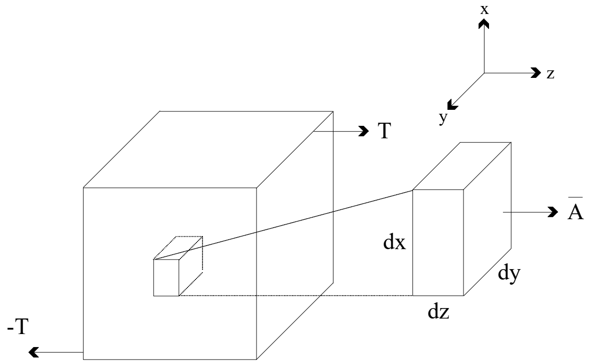

Figure 2.1: Orientation traction forces in an isotropic volume.

to four relations, by which the mechanical domain could be characterized. The first relation is based on Newton's Second law. In order to introduce that, the small material slab of figure 2.1, defined by dimensions dx, dy and dz, is considered . The area of this slab will be equal to

$$A = dx \cdot dy. \tag{2.3}$$

Now, let's rename T and $-T$ as T_A and T_B, respectively. If both stresses, T_A and T_B, are not equal, this results in a force on that slab, read by

$$dF = \mid T_B - T_A \mid \cdot dA = \frac{\partial T}{\partial z} \cdot dz \cdot dA. \tag{2.4}$$

Therefore, Newton's second law could be rewritten as

$$\frac{\partial T}{\partial z} \cdot dz \cdot A = \rho \cdot A \cdot \Delta z \cdot \frac{\partial^2 u}{\partial t^2}, \tag{2.5}$$

resulting in the final equation

$$\frac{\partial T}{\partial z} = \rho \cdot \frac{\partial^2 u}{\partial t^2}, \tag{2.6}$$

being ρ the mass density measured in Kg/m^3 and u the particle displacement, which relates to the particle velocity (v) as

$$v = \frac{\partial u}{\partial t}. \tag{2.7}$$

The internal particles of the body will suffer a mechanical displacement due to T. The mechanical displacement per unit of length is known as Strain (S):

$$S = \frac{\partial u}{\partial z}. \tag{2.8}$$

The fourth relation, and another important law in physic's world, was defined by Robert Hooke in 1660 [19]. This relation, known as Hooke's law or law of elasticity, defines the linear relation between the T and the S as

$$T = c \cdot S, \tag{2.9}$$

where c is the elastic constant of the material. Once the constitutive equations for the acoustical domain are defined, a systematic procedure to obtain the wave equation is done [15].

So, to start with this process, the first step is to make the time derivative of (2.8)

$$\frac{\partial S}{\partial t} = \frac{\partial^2 u}{\partial z \partial t}, \tag{2.10}$$

and using (2.7) in (2.10) we obtain

$$\frac{\partial S}{\partial t} = \frac{\partial v}{\partial z}. \tag{2.11}$$

The next step is to apply the time derivative of (2.9),

$$\frac{\partial T}{\partial t} = c \cdot \frac{\partial S}{\partial t}, \tag{2.12}$$

and combine it with (2.11)

$$\frac{\partial T}{\partial t} = c \cdot \frac{\partial v}{\partial z}. \tag{2.13}$$

Taking the time derivative of (2.13)

$$\frac{\partial^2 T}{\partial t^2} = c \cdot \frac{\partial^2 v}{\partial z \partial t} \rightarrow \frac{\partial^2 v}{\partial z \partial t} = \frac{1}{c} \cdot \frac{\partial^2 T}{\partial t^2}, \tag{2.14}$$

and using (2.6), results in

$$\frac{\partial^2 T}{\partial z^2} = \rho \cdot \frac{\partial^2 v}{\partial z \partial t} \rightarrow \frac{\partial^2 v}{\partial z \partial t} = \frac{1}{\rho} \cdot \frac{\partial^2 T}{\partial z^2}. \tag{2.15}$$

By equating (2.14) and (2.15), the one-dimensional wave equation for the acoustic domain is:

$$\frac{1}{\rho} \cdot \frac{\partial^2 T}{\partial z^2} = \frac{1}{c} \cdot \frac{\partial^2 T}{\partial t^2}. \tag{2.16}$$

From (2.16), we could know the phase velocity of the acoustic wave propagating along the material

$$v_a = \sqrt{\frac{c}{\rho}}. \tag{2.17}$$

2.2.2 Piezoelectric Constitutive Equations

The previous section defined how a mechanical wave propagates along a solid material. If the material is a piezoelectric slab, the mechanical wave will generate an electric field in it. Therefore, this type of material could be characterized by using the constitutive equations relating both, electrical and mechanical, domains. This section follows the nomenclature presented in [20], in which the piezoelectric constitutive relations are written as:

$$T = c^E S - eE, \tag{2.18}$$

$$D = eS + \varepsilon^S E. \tag{2.19}$$

The variables e and ε^S are the piezoelectric constant and the dielectric constant, respectively.

Grouping equations (2.18) and (2.19) in a single one, we obtain the constitutive equation for a piezoelectric medium, using the displacement vector D as independent variable, instead of E.

$$T = c^E \left(1 + \frac{e^2}{c^E \varepsilon^S}\right) S - \frac{e}{\varepsilon^S} D = c^D S - \frac{e}{\varepsilon^S} D, \tag{2.20}$$

where c^D is the stiffened elasticity or piezoelectrically stiffened elastic constant. This last equation is the one that will be used later by the Mason model. Knowing that, we can obtain the acoustic velocity in a piezoelectric medium using the stiffened elasticity in equation (2.17)

$$v^D = \sqrt{\frac{c^D}{\rho}} = \sqrt{\frac{c^E}{\rho}} \cdot \sqrt{1 + \frac{e^2}{c^E \varepsilon^S}} = v_a \cdot \sqrt{1 + \frac{e^2}{c^E \varepsilon^S}}. \tag{2.21}$$

The conversion efficiency of the piezoelectric material, and therefore, the total amount of electrical energy transformed to acoustical energy (or vice versa) is measured with the electromechanical coupling factor [20], written as

$$K^2 = \frac{e^2}{c^E \varepsilon^S}, \tag{2.22}$$

which depends only on the physical parameters of the material.

Some temperature effects appear in solids due to, for example, elastic reversible deformations, or directly some mechanical properties affected by internal or external temperature changes [18]. The thermal domain can be taken into account in the constitutive equations. The electro-thermo-mechanical constitutive equations based on the Electric Gibbs function, take into account the thermal phenomena in the piezoelectric material [11]. These constitutive equations, depicted in the Heckmann diagram shown in figure 2.2, are defined as

$$T = c^{E\theta} S - e^\theta E - \tau^E \theta, \tag{2.23}$$

$$D = e^\theta S + \varepsilon^{S\theta} E + \rho^S \theta, \tag{2.24}$$

$$\sigma = \tau^E S + \rho^S E + r^{ES} \theta, \tag{2.25}$$

where θ, σ, τ^E, ρ^S and r^{ES} are temperature, entropy, thermal pressure, pyroelectricity and heat capacity.

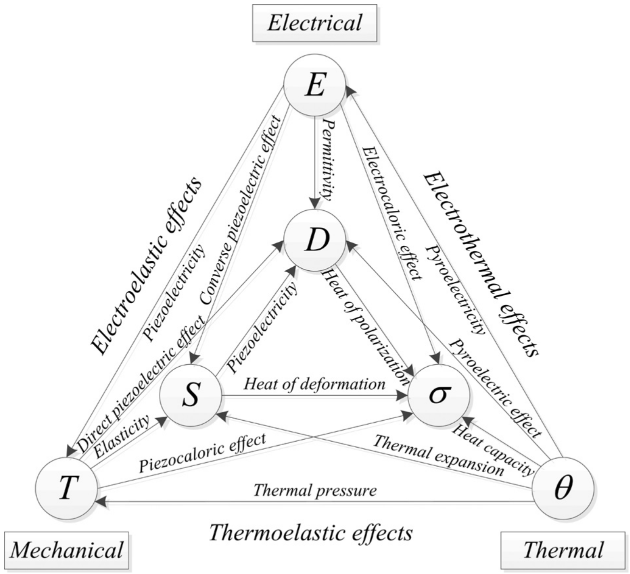

Figure 2.2: Heckmann diagram showing the relations between the electrical, thermal and mechanical domains in a crystal. [12]

The three previous constitutive equations comprehensively relate the three domains interacting in a piezoelectric subjected to a force or electric field. Now these equations will be extended to consider the inherent nonlinear dependence between these three domains.

2.3 Nonlinear Constitutive Equations

As it has been commented in the previous chapter, piezoelectric materials present a quite relevant nonlinear behavior, and this must be taken into account. The first nonlinear model based on the nonlinear constitutive equations for piezoelectric crystals was introduced in 2011 [10]. The model is quite robust and can represent with good agreement nonlinearities generated in real resonators. However, this model only considered the mechanical and the electrical domain for piezoelectric materials.

In 2013, a model considering the nonlinear electro-thermo-mechanical constitutive equations, extending the work of [10], was published [12]. The difference between these equations and the ones published in [10], was that [12] included all nonlinear phenomena appearing due to the thermal domain. Those new nonlinear constitutive equations are defined as

$$T = c^{E\theta} S - e^{\theta} E - \tau^{E} \theta + \Delta T_{NL}, \tag{2.26}$$

$$D = e^{\theta} S + \varepsilon^{S\theta} E + \rho^{S} \theta + \Delta D_{NL}, \tag{2.27}$$

$$\sigma = \tau^{E} S + \rho^{S} E + r^{ES} \theta + \Delta \sigma_{NL}, \tag{2.28}$$

where ΔT_{NL}, ΔD_{NL} and $\Delta \sigma_{NL}$ are the terms defining the nonlinear behavior of the piezoelectric layer, truncated to a third-order polynomial,

$$\begin{aligned}\Delta T_{NL} = & \frac{1}{2}(c_2^{E\theta} S^2 - \varphi_3 E^2 - \varphi_4 \theta^2) + \varphi_5 SE + \varphi_6 S\theta + \varphi_7 E\theta + \\ & + \frac{1}{6}(c_3^{E\theta} S^3 - e_3^{\theta} E^3 - \chi_5 \theta^3) - \chi_6 SE\theta ... + \\ & + \frac{1}{2}(\chi_7 SE^2 + \chi_8 S\theta^2 - \chi_9 S^2 E - \chi_{10} S^2 \theta - \chi_{11} E\theta^2 - \\ & - \chi_{12} E^2 \theta),\end{aligned} \tag{2.29}$$

$$\begin{aligned}\Delta D_{NL} = & \frac{1}{2}(\varepsilon_2^{S\theta} E^2 - \varphi_5 S^2 + \varphi_1 \theta^2) + \varphi_3 SE + \varphi_7 S\theta + \varphi_2 E\theta + \\ & + \frac{1}{6}(\varepsilon_3^{S\theta} E^3 + \chi_9 S^3 + \chi_1 \theta^3) + \chi_{12} SE\theta ... + \\ & + \frac{1}{2}(\chi_4 SE^2 + \chi_{11} S\theta^2 - \chi_7 S^2 E + \chi_6 S^2 \theta + \chi_2 E\theta^2 + \\ & + \chi_3 E^2 \theta),\end{aligned} \tag{2.30}$$

$$\begin{aligned}\Delta \sigma_{NL} = & \frac{1}{2}(r_2^{ES} \theta^2 + \varphi_2 E^2 - \varphi_6 S^2) + \varphi_7 SE + \varphi_4 S\theta + \varphi_1 E\theta + \\ & + \frac{1}{6}(r_3^{ES} \theta^3 + \chi_3 E^3 + \chi_{10} S^3) + \chi_{11} SE\theta ... + \\ & + \frac{1}{2}(\chi_{12} SE^2 + \chi_5 S\theta^2 + \chi_6 S^2 E - \chi_8 S^2 \theta + \chi_1 E\theta^2 + \\ & + \chi_2 E^2 \theta).\end{aligned} \tag{2.31}$$

Those nonlinear terms are mathematically defined by different second-order (c_2^E, φ_3, φ_5, ε_2^S, etc.) and third-order coefficients (c_3^E, ε_3^S, etc.).

These nonlinear constitutive equations are the basis for all the circuital models proposed along the whole thesis. Such circuital models will be fully detailed in chapter 3.

2.4 Basic Concepts of Nonlinearities

When manufacturers design and fabricate radio frequency (RF) devices, their objective is to obtain the greater performance and the better linear response as possible. But in reality this is not straightforward. All RF devices and systems present, to a greater or lesser extent, some degree of nonlinear behavior. As it has been mentioned previously, AW devices are a potential source of nonlinearities. This nonlinear behavior, being certainly an issue on BAW devices, could be manifested in many forms, as for example harmonic and intermodulation distortion generation.

This section recalls how nonlinear manifestations, generated inside a nonlinear device, affect and degrade the whole system performance [21].

2.4.1 Time Defined Nonlinear Equations

To introduce the time defined nonlinear equations, the case of a nonlinear two-port device under test (DUT) is considered, in which its input is fed by a signal $v_{in}(t)$ formed by a single tone $v_1(t)$ at ω_1

$$v_{in}(t) = v_1(t) = V_1 cos(\omega_1 t + \phi_1). \tag{2.32}$$

Due to the nonlinear behavior of the device, its output signal consist on the input signal affected by the behavior of the device, and some nonlinear components generated inside it. The nonlinear output signal up to a third-order is defined as

$$\begin{aligned} v_{out}(t) &= a_0 + a_1 \cdot v_{in}(t) + a_2 \cdot (v_{in}(t))^2 + a_3 \cdot (v_{in}(t))^3 = \\ &= a_0 + a_1 V_1 cos(\omega_1 t + \phi_1) + \frac{1}{2} a_2 V_1^2 + \frac{3}{4} a_3 V_1^3 cos(\omega_1 t + \phi_1) + \\ &+ \frac{1}{2} a_2 V_1^2 cos(2\omega_1 t + 2\phi_1) + \frac{1}{4} a_3 V_1^3 cos(3\omega_1 t + 3\phi_1). \end{aligned} \tag{2.33}$$

The nonlinear DUT generates some spurious signals appearing at frequencies different than the one of the tone feeding it. These new spurious signals appear at frequencies multiple of the fundamental frequency ω_1, degrading the whole performance of the system. These spurious signals are known as harmonics (H).

In real communication systems, however, more complex signals are feeding those devices. In order to further illustrate that phenomena (move towards that direction), let's consider the case where the DUT is fed by 2 tones at ω_1 and ω_2: $v_1(t)$ and $v_2(t)$

$$v_{in}(t) = v_1(t) + v_2(t) = V_1 cos(\omega_1 t + \phi_1) + V_2 cos(\omega_2 t + \phi_2). \tag{2.34}$$

As previously done, the resulting output signal can be read as:

$$\begin{aligned}
v_{out}(t) &= a_0 + a_1 \cdot v_{in}(t) + a_2 \cdot (v_{in}(t))^2 + a_3 \cdot (v_{in}(t))^3 = \\
&= a_0 + \frac{1}{2}a_2V_1^2 + \frac{1}{2}a_2V_2^2 + \\
&+ a_1V_1cos(\omega_1t+\phi_1) + \frac{3}{4}a_3V_1^3cos(\omega_1t+\phi_1) + \frac{3}{2}a_3V_1V_2^2cos(\omega_1t+\phi_1) + \\
&+ a_1V_2cos(\omega_2t+\phi_2) + \frac{3}{4}a_3V_2^3cos(\omega_2t+\phi_2) + \frac{3}{2}a_3V_1^2V_2cos(\omega_2t+\phi_2) + \\
&+ \frac{1}{2}a_2V_1^2cos(2\omega_1t+2\phi_1) + \frac{1}{2}a_2V_2^2cos(2\omega_2t+2\phi_2) + \\
&+ \frac{1}{4}a_3V_1^3cos(3\omega_1t+3\phi_1) + \frac{1}{4}a_3V_2^3cos(3\omega_2t+3\phi_2) + \\
&+ a_2V_1V_2cos((\omega_1+\omega_2)t+\phi_1+\phi_2) + a_2V_1V_2cos((\omega_2-\omega_1)t-\phi_1+\phi_2) + \\
&+ \frac{3}{4}a_3V_1^2V_2cos((2\omega_1-\omega_2)t+2\phi_1-\phi_2) + \\
&+ \frac{3}{4}a_3V_1V_2^2cos((2\omega_2-\omega_1)t-\phi_1+2\phi_2) + \\
&+ \frac{3}{4}a_3V_1V_2^2cos((2\omega_2+\omega_1)t+\phi_1+2\phi_2) + \\
&+ \frac{3}{4}a_3V_1^2V_2cos((2\omega_1+\omega_2)t+2\phi_1+\phi_2).
\end{aligned} \tag{2.35}$$

The new output frequency components generated will be $m \cdot \omega_1 \pm n \cdot \omega_2$, where, m,n = 0, ±1, ±2, ±3... The order of a given intermodulation distortion product (IMD) is defined as $\mid m \mid + \mid n \mid$, whereas the order of a given H is defined as $\mid m \mid$ for ω_1 and $\mid n \mid$ for ω_2. Those new frequency components are located in the frequency spectrum as depicted in figure 2.3.

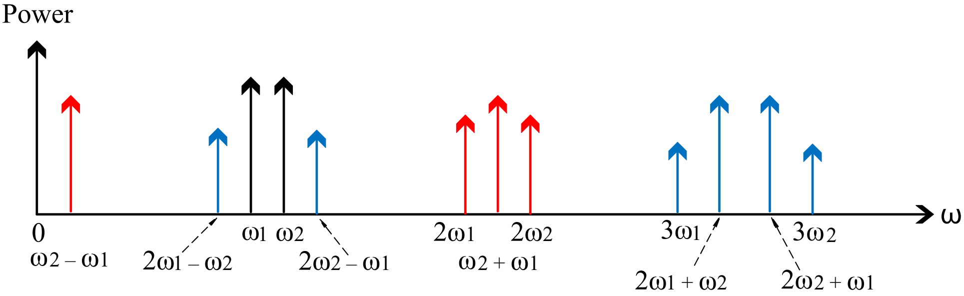

Figure 2.3: Frequency spectrum of second- and third-order nonlinear components at the output of a given nonlinear DUT. Red color indicate the spurious signals generated by a second-order nonlinear effect and the blue color indicates the spurious signals generated by a third order nonlinear effect.

2.4.2 Passive Intermodulation and Harmonic Generation

Although, mainly, nonlinear distortion is related with active devices, in some passive devices this could become quite relevant. This effect appearing in passive devices is known as Passive Intermodulation (PIM). PIM could be generated by different phenomena, such as, rusty materials in the device, bad contacts, temperature variations and the nonlinear physical properties of the materials.

As per equation (2.35), and only considering the spurious signals appearing at frequencies different than DC and the ones corresponding to the fundamental tones, the output voltage will be

$$\begin{aligned} v_{out,NL}(t) = {} & \frac{1}{2}a_2V_1^2cos(2\omega_1t+2\phi_1)+\frac{1}{2}a_2V_2^2cos(2\omega_2t+2\phi_2)+ \\ & +\frac{1}{4}a_3V_1^3cos(3\omega_1t+3\phi_1)+\frac{1}{4}a_3V_2^3cos(3\omega_2t+3\phi_2)+ \\ & +a_2V_1V_2cos((\omega_1+\omega_2)t+\phi_1+\phi_2)+ \\ & +a_2V_1V_2cos((\omega_1-\omega_2)t+\phi_1-\phi_2)+ \\ & +\frac{3}{4}a_3V_1^2V_2cos((2\omega_1-\omega_2)t+2\phi_1-\phi_2)+ \\ & +\frac{3}{4}a_3V_1V_2^2cos((\omega_1-2\omega_2)t+\phi_1-2\phi_2)+ \\ & +\frac{3}{4}a_3V_1V_2^2cos((2\omega_2+\omega_1)t+\phi_1+2\phi_2)+ \\ & +\frac{3}{4}a_3V_1^2V_2cos((2\omega_1+\omega_2)t+2\phi_1+\phi_2). \end{aligned} \tag{2.36}$$

Therefore, all the frequencies corresponding to the H and IMD products could be observed in equation (2.36). This generation of spurious signals, due to the nonlinear coefficients of the device (a_2 and a_3), is well known as PIM generation by direct effects.

In addition to the direct generation, PIM can also be predicted by what is known as remixing effects. This effect consist on a mix between an input signal with a spurious signal generated by a direct nonlinear effect, then producing new spurious signals. A clear example of that is when second-order directly generated spurious signals are mixed to the fundamental, giving rise to spurious signals at frequencies “corresponding” to a third order nonlinear effect.

This phenomena, quite important in communications, is further illustrated in figure 2.4, where two different examples are detailed. In red arrow, is depicted the spurious signal falling in $3\omega_1$ (H3 frequency), appearing due to the remixing effect between ω_1 and $2\omega_1$. Another example shown in blue arrow, is the spurious signal falling in $2\omega_2 - \omega_1$ (IMD3 frequency), appearing due to the remixing effect between ω_1 and $2\omega_2$.

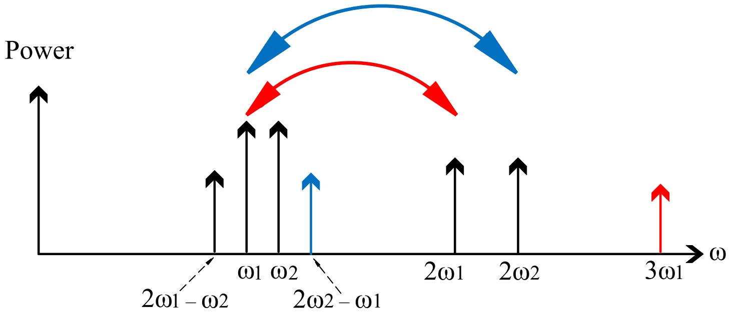

Figure 2.4: Frequency spectrum showing spurious signals generated by remixing effects frequencies.

2.4.3 Saturation

In active devices, one common effect of the nonlinear behavior is the gain compression or saturation. Physically, this effect occurs when the output power has surpassed some specific value. Once this power has been overpassed, the device cannot supply more gain, and starts saturating.

In order to quantify the range in which the device is working in the quasi-linear zone, the 1dB compression point is defined. This point, observed in figure 2.5, defines the output power 1 dB less than the one working in the linear zone.

This effect is also related with the nonlinear phenomena occurring inside some, active or passive, devices [22]. In the case of one tone feeding the device, the output signal generated will be the one mentioned in equation (2.33). The voltage gain of this will be the output voltage divided by the input voltage for the fundamental tone:

$$G = \frac{v_{1,out}(\omega_1)}{v_{1,in}(\omega_1)} = \frac{a_1 V_1 + \frac{3}{4} a_3 V_1^3}{V_1} = a_1 + \frac{3}{4} a_3 V_1^2. \tag{2.37}$$

Taking into account that the a_3 nonlinear coefficient must have the opposite sign than the a_1 coefficient of the linear term, as the input voltage increases, the gain tends to be reduced.

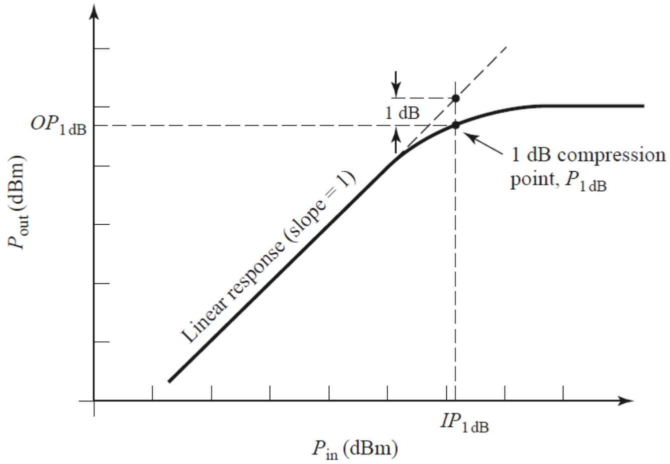

Figure 2.5: Definition of the 1dB compression point for a nonlinear amplifier [22].

2.4.4 Shift of Bias Point

Another effect of the nonlinear phenomena is the shift of bias point. This is provoked by the nonlinear terms of equation (2.35) appearing at DC frequency

$$v_{out,NL}(\omega_{DC}) = a_0 + \frac{1}{2}a_2V_1^2 + \frac{1}{2}a_2V_2^2 + ... \tag{2.38}$$

The appearing DC-component, is one of the nonlinear components known as out-of-band distortion defined with this name in [21].

Detuning under DC Bias Voltage in an Acoustic Medium

In addition to the nonlinear manifestations commented above, it could appear another nonlinear spurious signals due to, for example, external DC sources feeding the device. In this subsection, particularized to a piezoelectric slab, it will be presented the detuning of the device under the application a DC bias voltage.

Regarding the constitutive equations that model only the acoustical and electrical properties of the piezoelectric layer, the relation between the T and the S was defined by,

$$T = c^E S - eE + \Delta T_{NL}, \tag{2.39}$$

where the nonlinear interaction between electrical and acoustical domain, simplified for the hypothesis considered in [10] and [12], is defined by,

$$\Delta T_{NL} = \frac{1}{2}c_2^E S^2 + \frac{1}{6}c_3^E S^3 + \varphi_5 SE, \tag{2.40}$$

so, we can write

$$T = c^E S - eE + \frac{1}{2}c_2^E S^2 + \frac{1}{6}c_3^E S^3 + \varphi_5 SE. \tag{2.41}$$

In order to characterize the DC feed contribution, the S can be modeled as the sum of the contributions of the strain produced by the DC voltage, S_{DC}, and the strain produced by the harmonic frequency

$$S = S_{DC} + S_0 cos(\omega t), \tag{2.42}$$

and the contributions to the T for second- and third-order nonlinearities are,

$$S^2 = S_{DC}^2 + 2S_{DC}S_0 cos(\omega t) + \frac{1}{2}S_0^2 cos(2\omega t) + \frac{1}{2}S_0^2, \tag{2.43}$$

$$\begin{aligned} S^3 = S_{DC}^3 + 3S_{DC}^2 S_0 cos(\omega t) + \frac{3}{2}S_{DC}S_0^2 cos(2\omega t) + \frac{3}{2}S_{DC}S_0^2 + \\ + \frac{3}{4}S_0^3 cos(\omega t) + \frac{1}{4}S_0^3 cos(3\omega t). \end{aligned} \tag{2.44}$$

The Electric field can also be modeled as the sum of the contribution of the static electric field and the electric field produced by the fundamental signal with peak amplitude E_0,

$$E = E_{DC} + E_0 cos\left(\omega t\right). \tag{2.45}$$

Matching the relation between T and S in equation (2.41) with equations (2.42), (2.43) and (2.44) we obtain:

$$\begin{aligned} T = c^E(S_{DC} + S_0 cos(\omega t)) - eE + \frac{1}{2}c_2^E(S_{DC}^2 + 2S_{DC}S_0 cos(\omega t) + \frac{1}{2}S_0^2 cos(2\omega t) + \\ + \frac{1}{2}S_0^2) + \frac{1}{6}c_3^E(S_{DC}^3 + 3S_{DC}^2 S_0 cos(\omega t) + \frac{3}{2}S_{DC}S_0^2 cos(2\omega t) + \frac{3}{2}S_{DC}S_0^2 + \\ + \frac{3}{4}S_0^3 cos(\omega t) + \frac{1}{4}S_0^3 cos(3\omega t)) + \varphi_5 E(S_{DC} + S_0 cos(\omega t)). \end{aligned} \tag{2.46}$$

Rewriting equation (2.46), in order to separate the terms affecting the S produced by the fundamental frequency from the terms not affecting it, we obtain,

$$\begin{aligned} T = {} & c^E S_{DC} - eE + \varphi_5 S_{DC} E + \frac{1}{2} c_2^E S_{DC}^2 + \frac{1}{4} c_2^E S_0^2 + \frac{1}{6} c_3^E S_{DC}^3 + \frac{1}{4} c_3^E S_{DC} S_0^2 + \\ & + S_0 \left(c^E + c_2^E S_{DC} + \frac{1}{2} c_3^E S_{DC}^2 + \frac{1}{8} c_3^E S_0^2 + \varphi_5 E \right) cos(\omega t) + \\ & + S_0 \left(\frac{1}{4} c_2^E S_0 + \frac{1}{4} c_3^E S_{DC} S_0 \right) cos(2\omega t) + \frac{1}{24} c_3^E S_0^3 cos(3\omega t). \end{aligned} \tag{2.47}$$

The saturation term $(1/8)c_E^3 S_0^2$ that does not depend on the DC bias voltage can be neglected for low-power levels. Then the stiffness constant due to the contribution of DC voltage, considering only in E the contribution of the static field E_{DC} only, is defined by,

$$c^{E,DC} = c^E \left(1 + \frac{c_2^E}{c^E} S_{DC} + \frac{1}{2} \frac{c_3^E}{c^E} S_{DC}^2 + \frac{\varphi_5}{c^E} E_{DC} \right), \tag{2.48}$$

and the piezoelectric constant modified by the DC voltage is,

$$e^{DC} = e \left(1 - \frac{\varphi_5}{e} S_{DC} \right). \tag{2.49}$$

The S produced by the DC voltage is

$$S^{DC} = \frac{e}{c^E} E_{DC} = \frac{e}{c^E} \frac{-V_{DC}}{d}, \tag{2.50}$$

being d the thickness of the piezoelectric layer. Therefore, we can define an effective elastic $c^{E,DC}$ and piezoelectric e^{DC} constants under DC bias voltage as

$$c^{E,DC} = c^E \left(1 - \frac{c_2^E e}{(c^E)^2 d} V_{DC} + \frac{1}{2} \frac{c_3^E e^2}{(c^E)^3 d^2} V_{DC}^2 - \frac{\varphi_5 e}{c^E d} V_{DC} \right), \tag{2.51}$$

$$e^{DC} = e \left(1 + \frac{\varphi_5}{c^E d} V_{DC} \right). \tag{2.52}$$

The contribution of the nonlinear term ε_2^S can be taking into account straightforward just replacing

$$\varepsilon^{S,DC} = \varepsilon^S \left(1 - \frac{\varepsilon_2^S}{\varepsilon^S d} V_{DC}\right). \tag{2.53}$$

The modified terms of (2.51), (2.52) and (2.53) can be used instead of c^E, e, and ε^S in linear simulations. So, with that we can observe how applying a DC bias voltage to the piezoelectric layer, the physical properties of that will change. The variation of the elastic constant produces a variation in the phase velocity of the acoustic wave and the acoustic impedance, resulting in a detuning of the device.

2.4.5 Self-Heating Effects in an Acoustic Medium

It is well known that self-heating effects can also produce IMD3. The heat generated by the instantaneous dissipated power of a signal formed by two tones spaced $\Delta\omega = \omega_2 - \omega_1$ will follow time fluctuations at this frequency [23]. If the frequency spacing between tones is small (few tenths of kHz or less), those fluctuations are very slow, being the material able to follow the dynamic variations of the temperature, changing the material properties that are temperature dependent. The $\Delta\omega$-varying material properties will modulate the fundamental signals producing IMD3 distortion. The slower the variation, the higher the IMD3 because of the specific heat of the material, which determines the capability of the material to change its temperature under a dynamic heat flux.

For sake of clarity, some equations will be introduced. If the voltage of a signal formed by two tones at ω_1 and ω_2 is

$$V = V_{\omega_1} cos(\omega_1 t) + V_{\omega_2} cos(\omega_2 t), \tag{2.54}$$

the power dissipated by that will be proportional to the square of the voltage

$$\begin{aligned}P_d(\omega) &= (V_{\omega_1}cos(\omega_1 t) + V_{\omega_2}cos(\omega_2 t))^2 = \\ &= \frac{1}{2}V_{\omega_1}^2 + \frac{1}{2}V_{\omega_2}^2 + \frac{1}{2}V_{\omega_1}^2 cos(2\omega_1 t) + \frac{1}{2}V_{\omega_2}^2 cos(2\omega_2 t) + \\ &+ V_{\omega_1}V_{\omega_2}cos((\omega_1+\omega_2)t) + V_{\omega_1}V_{\omega_2}cos((\omega_2-\omega_1)t), \end{aligned} \tag{2.55}$$

where this produces variation of the temperature at different frequencies, including $\Delta\omega$.

For the case of a mechanical wave, the T was defined as

$$T = c^E S, \tag{2.56}$$

where the stiffness constant including the thermal dependence, could be described as

$$c^E = c_0^E + \varphi_6\theta, \tag{2.57}$$

being the nonlinear term φ_6 the temperature derivative of the elastic constant (see equation (2.29)). Now, substituting equation (2.57) in equation (2.56)

$$T = c_0^E S + \varphi_6\theta S. \tag{2.58}$$

If the S is formed by the contribution of two different acoustic signals as

$$S = S_0 cos(\omega_1 t) + S_0 cos(\omega_2 t), \tag{2.59}$$

and knowing that those signals will dissipate power at $\omega_2 - \omega_1$, the temperature could be written as

$$\theta = \theta_0 + \theta_{\omega_2-\omega_1}cos((\omega_2-\omega_1)t). \tag{2.60}$$

Then, the final T provoked by those signals is defined as

$$T = c_0^E(S_0 cos(\omega_1 t) + S_0 cos(\omega_2 t)) + \varphi_6\theta(S_0 cos(\omega_1 t) + S_0 cos(\omega_2 t)), \tag{2.61}$$

where the nonlinear terms depending on temperature are

$$\begin{aligned}\Delta T_\theta &= \varphi_6(\theta_0 + \theta_{\omega_2-\omega_1} cos((\omega_2-\omega_1)t))(S_0 cos(\omega_1 t) + S_0 cos(\omega_2 t)) = \\ &= \varphi_6(\theta_0 S_0(cos(\omega_1 t) + cos(\omega_2 t)) + \\ &\quad + \theta_{\omega_2-\omega_1} S_0(cos((\omega_2-\omega_1)t)cos(\omega_1 t) + cos((\omega_2-\omega_1)t)cos(\omega_2 t))),\end{aligned} \tag{2.62}$$

and then, by removing the terms that do not depend on the temperature $\theta_{\omega_2-\omega_1}$, the simplified equation reads:

$$\begin{aligned}\Delta T_\theta = \varphi_6(\theta_{\omega_2-\omega_1} S_0(\frac{1}{2}cos(\omega_2 t) + \frac{1}{2}cos((2\omega_1-\omega_2)t) + \frac{1}{2}cos(\omega_1 t) + \\ + \frac{1}{2}cos((2\omega_2-\omega_1)t))).\end{aligned} \tag{2.63}$$

Now, equation (2.63) reveals how the power dissipated and therefore, the temperature changes occurring in the material by this signal, are generating some spurious signals at the IMD3 frequencies.

Heat propagation could be modeled as a lattice RC (thermal resistance and heat capacity) circuit as depicted in figure 2.6, in which current and voltage are equivalent to heat flow and temperature, respectively [23]. This electric circuit model is based in a T-network circuit formed by two thermal resistances R_{th} and one thermal capacitance C_{th}. The temperature θ is modeled as the voltage dropped in the thermal capacitance, while the heat flow is the current flowing by the thermal resistance.

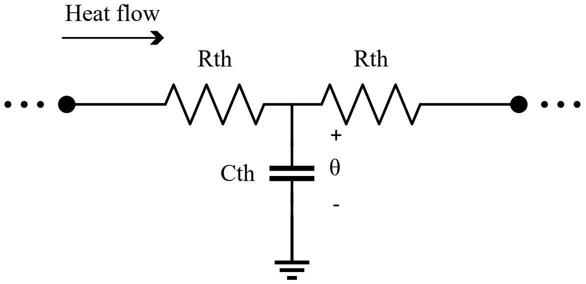

Figure 2.6: RC thermal network modeling the thermal domain.

This distributed RC network acts as a low-pass filter eliminating the higher frequency components and therefore the IMD3 has a clear dependence with $\Delta\omega$. This dependence allows to discern between intrinsic nonlinearities or self-heating mechanisms if proper experiments are conducted [23].

2.4.6 Frequency Defined Nonlinear Equations

The nonlinear equations presented previously could have their representation in the frequency domain. By using the frequency domain, the computational complexity when solving nonlinear equations in some specific cases and/or scenarios could be reduced.

In order to obtain the frequency defined domain nonlinear equations, the different nonlinear frequencies forming the signal of equation (2.35) will be identified, and transformed to the phasorial domain. So, for the harmonic distortion, the phasors of the second-order spurious signals are

$$V_{out}(2\omega_1) = \frac{1}{2}a_2 \mid V_1 \mid^2 e^{j2\phi_1} = \frac{1}{2}a_2 V_1^2, \tag{2.64}$$

$$V_{out}(2\omega_2) = \frac{1}{2}a_2 \mid V_2 \mid^2 e^{j2\phi_2} = \frac{1}{2}a_2 V_2^2, \tag{2.65}$$

and for the third order are

$$V_{out}(3\omega_1) = \frac{1}{4}a_3 \mid V_1 \mid^3 e^{j3\phi_1} = \frac{1}{4}a_3 V_1^3, \tag{2.66}$$

$$V_{out}(3\omega_2) = \frac{1}{4}a_3 \mid V_2 \mid^3 e^{j3\phi_2} = \frac{1}{4}a_3 V_2^3. \tag{2.67}$$

The intermodulation products defined in the frequency domain, will be for the second-order terms

$$V_{out}(\omega_2 - \omega_1) = a_2 \mid V_1 \mid\mid V_2 \mid e^{j(\phi_2-\phi_1)} = a_2 V_1^* V_2, \tag{2.68}$$

$$V_{out}(\omega_2 + \omega_1) = a_2 \mid V_1 \mid\mid V_2 \mid e^{j(\phi_1+\phi_2)} = a_2 V_1 V_2, \tag{2.69}$$

and for the third order terms

$$V_{out}(2\omega_1 - \omega_2) = \frac{3}{4} a_3 \mid V_1 \mid^2\mid V_2 \mid e^{j(2\phi_1-\phi_2)} = \frac{3}{4} a_3 V_1^2 V_2^*, \tag{2.70}$$

$$V_{out}(2\omega_2 - \omega_1) = \frac{3}{4} a_3 \mid V_1 \mid\mid V_2 \mid^2 e^{j(2\phi_2-\phi_1)} = \frac{3}{4} a_3 V_1^* V_2^2. \tag{2.71}$$

It can be easily observed in the phasorial domain how the power of the nonlinear components generated depends, in a greater or lesser extent, to the power of the fundamental signal. For example, regardless the nonlinear coefficients a_2 and a_3, it could be observed how the voltage of the second harmonic (H2) is equal to the square of the fundamental tone voltage multiplied by a factor $\frac{1}{2}$. If now, the H3 is considered, it could be observed how this product is multiplied by a factor $\frac{1}{4}$.

Furthermore, note how the conjugate voltage of the tone with negative signal is affecting to the voltage of the second-order intermodulation distortion (IMD2) $(\omega_2 - \omega_1)$ and IMD3 cases $(2\omega_1 - \omega_2$ and $2\omega_2 - \omega_1)$.

The power dependence of the nonlinear signals generated with the fundamental tone tend to a certain slope, being this a factor of 1:2 for the second-order nonlinear terms and 1:3 for the third-order nonlinear terms.

Chapter 3

Modeling of Bulk Acoustic Wave Resonators

3.1 Introduction

As briefly mentioned previously, BAW resonators consist in two parallel metal electrodes sandwiching a piezoelectric layer between them. The electric field is generated in the direction of the layer thickness, orthogonal to the piezoelectric layer. Due to the generation of electric field, the piezoelectric layer will be mechanically deformed, creating acoustic waves.

These waves must be confined in the acoustic cavity in order to create resonant modes into the structure. Depending on the technique used to confine the acoustic waves, two types of BAW resonators are considered: film bulk acoustic resonators (FBAR) and solidly mounted resonators (SMR) [24], [25]. Figure 3.1 left shows the basic structure of FBAR, in which an air cavity placed below the bottom electrode confines the acoustic waves, avoiding the propagation through the underneath layers. The free-stress boundary condition at the air, forces the reflection of the acoustic wave between the top and the bottom electrodes allowing the resonating modes. Figure 3.1 right shows the structure of SMR, in which a Bragg reflector is placed below the bottom electrode. The Bragg reflector is designed alternating low and high acoustic impedance sections by means of layers of different materials in order to confine the acoustic wave to certain conditions of reflection [26], [27], [28], [29]. Although other materials could be used, the Bragg reflector for BAW resonators is commonly based on a combination of tungsten (W) as the material with high acoustic impedance, with silicon dioxide (SiO_2) as the material with low acoustic impedance.

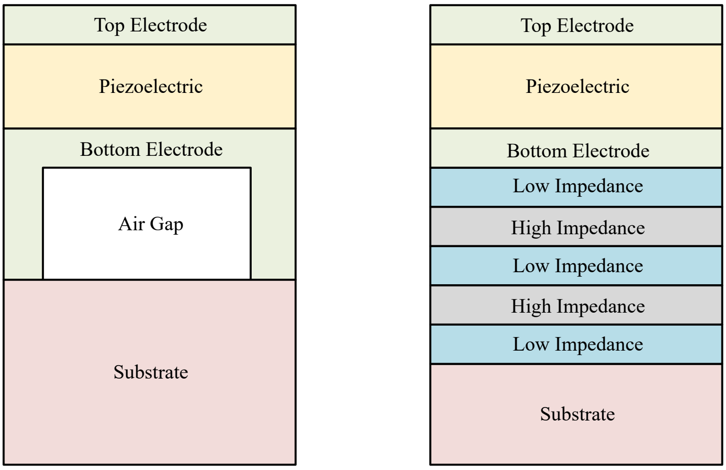

Figure 3.1: BAW resonator fabrication technologies. Left BAW resonator shows the FBAR configuration and right BAW resonator shows the SMR configuration.

This chapter details on the circuital modeling of BAW resonators. Although those devices could be simulated taking into account the whole resonator structure by using advanced design software tools, this chapter does emphasize in the one-dimensional nonlinear modeling. By only considering the propagation of the acoustic wave in the thickness direction of the resonator structure, the computational time required for solving the mathematical nonlinear equations is reduced remarkably, making this analysis suitable.

Many different circuital approaches have been published during the last decades. This chapter will outline some of those models.

3.2 Linear Models

As a first step to represent BAW resonators with a circuital model, a simple prototype resonator must be studied [20]. For that, the piezoelectric plate of thickness d shown in figure 3.2 will be considered.

This plate will generate an acoustic wave propagating in the thickness direction z, from z_1 to z_2, when an electric field E is applied to the material. The resonant frequencies of this plate are

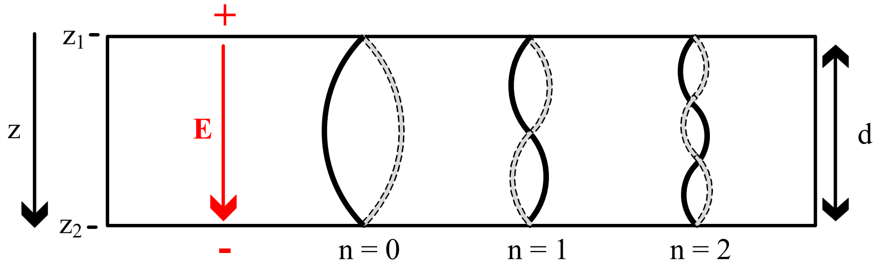

Figure 3.2: Mechanical resonances generated in a plate of thickness d when an electric field E is applied to the material.

$$\omega_n = (n+1)\cdot\pi\cdot\frac{v^D}{d}, n = 0,1,2..., \tag{3.1}$$

where the frequencies corresponding to the modes up to $n = 2$ can be observed in the figure.

The conditions assumed for that analysis are two. The first one assumes that the piezoelectric plate has lateral dimensions much larger than the thickness, in order to assume the one-dimensional case. The second one, considers that the electrodes covering the plate are mass less. Taking those considerations into account, and looking back to the wave equation (2.16),the displacement is assumed as a general Ansatz equation

$$u(z,t) = [a\cdot sin(kz) + b\cdot cos(kz)]\cdot e^{j\omega t}, \tag{3.2}$$

where k is the propagation constant, z the thickness direction, a the amplitude of the transmitted wave, and b the amplitude of the reflected wave.

For sake of clarity, an Ansatz is a method to establish the starting equations describing a mathematical problem, making assumptions to make the solution easier to find [20]. Through this point the term $e^{j\omega t}$ is neglected, as is explained in [20], to write it with the phasorial expression.

The wave number depends on the acoustic velocity in a piezoelectric medium following

$$k = \frac{\omega}{v^D} = \frac{2\pi}{\lambda}. \tag{3.3}$$

Now, if the constitutive equation for a piezoelectric medium is retaken

$$T = c^D S - \frac{e}{\varepsilon^S} D, \tag{3.4}$$

the displacement defined in equation (3.2) could be inserted in equation (3.4), defining now T as

$$T(z) = c^D \cdot k \cdot (a \cdot cos(kz) - b \cdot sin(kz)) - \frac{e}{\varepsilon^S} D. \tag{3.5}$$

The constants a and b can be obtained considering that the boundary condition of vanishing stress at the upper and lower surfaces are T($\pm\frac{d}{2}$) = 0, and (3.5) becomes

$$T(z) = \frac{e}{\varepsilon^S} D \cdot \left(\frac{cos(kz)}{cos\left(k \cdot \frac{d}{2}\right)} - 1 \right). \tag{3.6}$$

3.2.1 Input Impedance

As the impedance is the ratio between the voltage and the current flowing by the device, those magnitudes must the calculated. The voltage along the piezoelectric layer is given by

$$V = -\int_{z_2}^{z_1} E(z) dz, \tag{3.7}$$

where, by solving the constitutive equations, E is

$$E = \frac{e}{\varepsilon^S \cdot c^D} \cdot T - \left(\frac{1}{\varepsilon^S} - \frac{e^2}{(\varepsilon^S)^2 \cdot c^D} \right) D. \tag{3.8}$$

The voltage is written as

$$V = \frac{d \cdot D}{\varepsilon^S} \cdot \left(1 - \frac{e^2}{c^D \cdot \varepsilon^S} \cdot \frac{tan\left(k \cdot \frac{d}{2}\right)}{k \cdot \frac{d}{2}} \right), \tag{3.9}$$

and the current at the terminals is written by

$$I = j\omega \cdot A \cdot D, \tag{3.10}$$

where A is the area of the device. Then, the impedance is calculated

$$Z = \frac{V}{I} = \frac{1}{j\omega \cdot A \cdot D} \cdot \frac{d \cdot D}{\varepsilon^S} \cdot \left(1 - \frac{e^2}{c^D \cdot \varepsilon^S} \cdot \frac{tan\left(k \cdot \frac{d}{2}\right)}{k \cdot \frac{d}{2}} \right) =$$

$$= \frac{1}{j\omega \cdot C_0} \cdot \left(1 - K_t^2 \cdot \frac{tan\left(k \cdot \frac{d}{2}\right)}{k \cdot \frac{d}{2}} \right), \tag{3.11}$$

where the term C_0 is the static capacitance present in the acoustic resonator. Finally, C_0 is given by the expression

$$C_0 = \frac{\varepsilon^S \cdot A}{d}. \tag{3.12}$$

Note that another electromechanical coupling factor K_t^2, has appeared here. This K_t^2, known as electromechanical coupling factor for the thickness-longitudinal vibration, related with the energy conversion between the mechanical and the electrical domain, is defined as

$$K_t^2 = \frac{e^2}{c^D \cdot \varepsilon^S} = \frac{K^2}{K^2 + 1}. \tag{3.13}$$

For some piezoelectric materials, like the AlN or the zinc oxide (ZnO), this new factor is relatively equal to the electromechanical coupling factor, defined in (2.22), being $K_t^2 \approx K^2$.

Once the equations of our model are defined, the resonant frequencies of the resonator can be obtained from equation (3.11).

The shunt resonance, commonly known as antiresonance frequency, appears when the input impedance of the acoustic device tends to infinite ($Z \rightarrow \infty$). This case is given in equation (3.11) when

$$k \cdot \frac{d}{2} = (2n+1) \cdot \frac{\pi}{2}, n = 0, 1, 2, ... \tag{3.14}$$

so, by using equation 3.3, the antiresonance frequency ω_a is defined as

$$\omega_{a,n} = (2n+1) \cdot \frac{\pi}{2} \cdot \frac{v^D}{d}, n = 0, 1, 2, ... \tag{3.15}$$

The resonant frequency of the device is produced when the current flowing through it is maximal. This means that the input impedance of the device is equal to 0 ($Z = 0$). Therefore, the resonant frequency ω_r is obtained from

$$K_t^2 = \frac{\pi}{2} \cdot \frac{\omega_r}{\omega_{a,0}} \cdot \frac{1}{tan\left(\frac{\pi}{2} \cdot \frac{\omega_r}{\omega_{a,0}}\right)} \cong \frac{\pi^2}{4} \cdot \frac{\omega_r}{\omega_{a,0}} \cdot \left(1 - \frac{\omega_r}{\omega_{a,0}}\right). \tag{3.16}$$

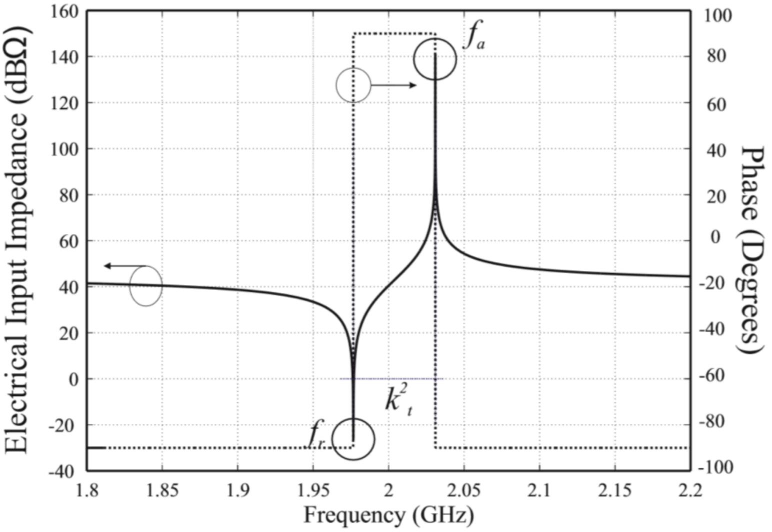

Figure 3.3: Electrical input impedance of an AW resonator. Left axis indicates the magnitude in $dB\Omega$ and right axis indicates the phase in degrees. [15]

The typical narrow-band input impedance of an acoustic resonator, and their characteristic resonant frequencies is observed in figure 3.3. The resonant frequency can be found as the frequency in which the electrical input impedance tends to zero. Close to the resonant frequency, at higher frequencies, can be observed the antiresonance frequency, in which the impedance tends to infinite. As is depicted in figure 3.3 too, and it can be demonstrated from equation (3.16), the frequency spacing between both, resonant and antiresonance frequencies, is determined by the K_t^2 coefficient.

3.2.2 Butterworth-Van Dyke Model

In 1928, the Butterworth-Van Dyke (BVD) model for piezoelectric resonators was presented [30]. This model emulates the main resonances of an AW resonator, being able to model properly the narrow band response for BAW resonators. This circuit model is the preferred one for acoustic filtering design, due to its simplicity. It's worth to mention at this point that the BVD circuit model is also useful to model the narrow band configuration of a SAW device.

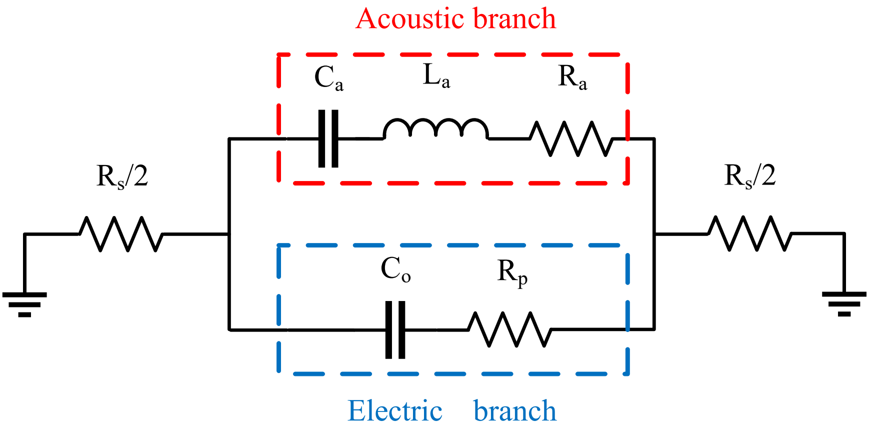

Figure 3.4: BVD circuit model.

The BVD model, depicted in figure 3.4, is characterized by its two different branches: the acoustic branch and the electric branch. The acoustic branch, depicted in red, is formed by a series resonant circuit formed by an acoustic capacitance C_a, an acoustic inductance L_a, and a resistance R_a modeling the losses appearing in the acoustic path. The electric branch, shown in blue, is formed by the static capacitance C_0 and the resistance R_p [31]. $R_s/2$ is the resistance due to the ohmic losses of the metallic pads.

The input impedance for the lossless case is written

$$Z(\omega) = \frac{j\left(\omega \cdot L_a - \left(\frac{1}{\omega \cdot C_a}\right)\right)}{1 - \omega^2 \cdot C_0 \cdot L_a + \frac{C_0}{C_a}}. \tag{3.17}$$

where it can be observed that neither the losses corresponding to the electrodes nor the losses corresponding to the acoustic part are considered.

Once the expression for the impedance is defined in this model, the characteristic resonant frequencies of an acoustic device could be obtained, as it has been mentioned before. The resonant frequency, appearing when $Z = 0$, will be

$$\omega_r = \frac{1}{\sqrt{L_a \cdot C_a}}, \tag{3.18}$$

and the antiresonance frequency ($Z \to \infty$) will be

$$\omega_a = \sqrt{\frac{C_a + C_0}{L_a \cdot C_a \cdot C_0}} = \omega_r \cdot \sqrt{1 + \frac{C_a}{C_0}}. \tag{3.19}$$

The quality factor (Q) is an important parameter to take into account in real devices. In resonant circuits theory, the Q is the ratio between stored energy and losses for a given frequency. This parameter quantifies the total amount of electrical and mechanical losses in acoustic devices. In the BVD model considering the resistive terms, the losses of the acoustic branch are modeled with the resistance R_a, while the losses of the electrodes are modeled through the term R_s. The resistance R_p, placed in the static capacitance branch, models the losses at the antiresonance frequency. The Q for the resonant frequency is then:

$$Q_s = \frac{\omega_r \cdot L_a}{R_s + R_a}, \tag{3.20}$$

and the Q for the antiresonance frequency is

$$Q_p = \frac{\omega_a \cdot L_a}{R_p + R_a}. \tag{3.21}$$

3.2.3 Mason Lumped

The BVD model is the preferred one if the main goal is to emulate the linear in-band behavior of a given acoustic resonator by reducing the complexity of the circuit. But if the main purpose of the model is to emulate the broadband behavior of the piezoelectric layer, altogether with the other layers forming the stack, more complex circuital models are required.

In 1950, Warren Perry Mason presented the Mason model [11]. This model was able to reproduce the one-dimensional electro-acoustic behavior of a uniform piezoelectric plate by taking into account the physical parameters of the materials used.

Although here the Mason model will be briefly described following [20], another references go deeper behind the physics involved in that circuital model [11], [15] and [32].

First of all, the thin film piezoelectric plate with thickness d, sandwiched between two metal plates located at z_1 and z_2, shown in figure 3.2, will be considered. This piezoelectric layer is described by the constitutive equations presented previously, so the E into the piezoelectric is

$$E = \frac{1}{\varepsilon^S} \cdot D - \frac{e}{\varepsilon^S} \cdot S = \frac{1}{\varepsilon^S} \cdot D - \frac{e}{\varepsilon^S} \cdot \frac{\partial u}{\partial z}. \tag{3.22}$$

The voltage, as it was defined in equation (3.7), is

$$V = -\int_{z2}^{z1} E(z)dz = \frac{d \cdot D}{\varepsilon^S} - \frac{e}{\varepsilon^S} \cdot \left[u(z_2) - u(z_1)\right]. \tag{3.23}$$

Knowing that the thickness of the plate d is equal to $z_2 - z_1$, the particle velocity (v) is the time derivative of the particle displacement, and D is equal to

$$D = \frac{I}{j\omega \cdot A}, \tag{3.24}$$

the voltage could be read as

$$V = \frac{d}{\varepsilon^S} \cdot \frac{I}{j\omega \cdot A} - \frac{e}{j\omega \cdot \varepsilon^S} \cdot \left[v(z_2) - v(z_1)\right]. \tag{3.25}$$

If now equation (3.25) is rewritten for I

$$I = j\omega \cdot C_0 \cdot V + \frac{e \cdot C_0}{\varepsilon^S} \left[v(z_2) - v(z_1) \right]. \tag{3.26}$$

Now, if the displacement defined in equation (3.2) is considered, and it is specified to the case of displacements $u(z_1)$ and $u(z_2)$, then

$$a = \frac{1}{sin(kd)} \cdot \left[u(z_2) \cdot cos(kz_1)) - u(z_1) \cdot cos(kz_2) \right], \tag{3.27}$$

$$b = \frac{1}{sin(kd)} \cdot \left[u(z_1) \cdot cos(kz_2)) - u(z_2) \cdot cos(kz_1) \right]. \tag{3.28}$$

The mechanical force appearing at the piezoelectric edges is minus A times the T applied to the device

$$F = -T \cdot A = -\left(c^D \cdot S - \frac{e}{\varepsilon^S} \cdot D \right) \cdot A. \tag{3.29}$$

Now, if equation (3.29) defining the force at the boundaries is rewritten, considering that the S is defined by the coefficients a and b of equations (3.27) and (3.28), we will obtain for the case $z = z_1$

$$F_1 = \frac{k \cdot c^D \cdot A}{sin(kd)} \cdot [u(z_2) - u(z_1)] - k \cdot c^D \cdot A \cdot tan(k\frac{d}{2}) \cdot u(z_1) + \frac{e \cdot D}{\varepsilon^S} \cdot A. \tag{3.30}$$

Finally, knowing that acoustic impedance is defined by

$$Z = \rho \cdot A \cdot v_a = \frac{k \cdot c^D}{\omega}, \tag{3.31}$$

where ρ is the material density, and remembering equation (3.24) and the relation between particle displacement and particle velocity $v = j\omega \cdot u$, we could rewrite equation (3.30) as

$$F_1 = \frac{Z \cdot A}{jsin(kd)} \cdot [v(z_1) - v(z_2)] + jZ \cdot A \cdot tan(k\frac{d}{2}) \cdot v(z_1) + \frac{e}{j\omega \cdot \varepsilon^S} \cdot I, \tag{3.32}$$

and for the other boundary ($z = z_2$) will be

$$F_2 = \frac{Z \cdot A}{jsin(kd)} \cdot [v(z_1) - v(z_2)] - jZ \cdot A \cdot tan(k\frac{d}{2}) \cdot v(z_2) + \frac{e}{j\omega \cdot \varepsilon^S} \cdot I. \quad (3.33)$$

The previous equations relate the force applied at the boundaries with the mechanical particle displacement generated, and with the electrical current generated, due to the piezoelectric phenomena inherent in those materials. All these equations are well represented in the aforementioned Mason based model, depicted in figure 3.5.

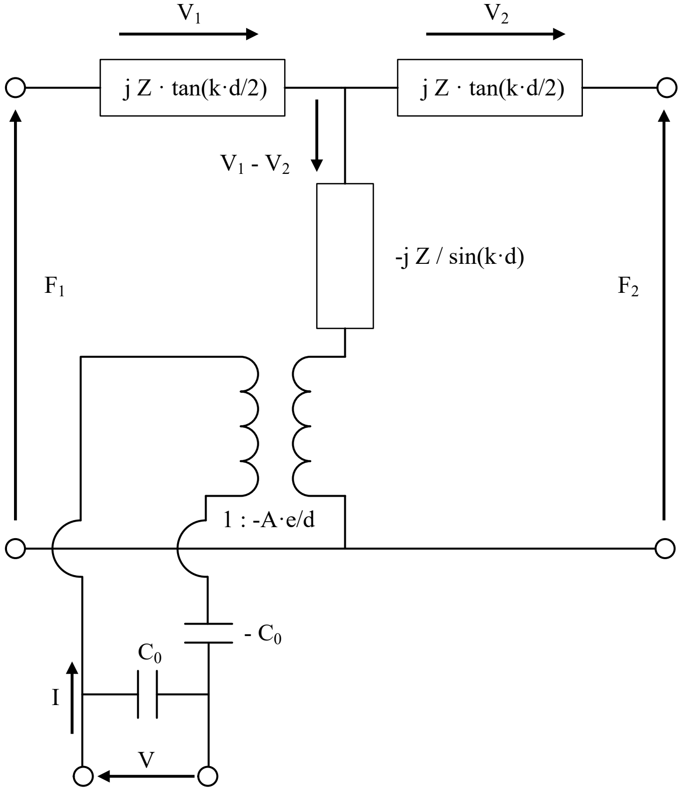

Figure 3.5: Lumped Mason model for a piezoelectric layer of thickness d.

It could be observed how this model is formed by a T-impedance circuit defining the acoustic domain and how the mechanical wave is propagating along the thickness direction. The electrical transformer models the electro-acoustic conversion. Finally the electric domain is represented by the input port, in which the electric field is applied, and the static capacitance C_0 present in acoustic resonators.

For the non-piezoelectric material case, the equations relating the force at the boundaries with the mechanical displacement are similar to the ones corresponding to the piezoelectric case, without considering the electrical fields, that are not present in those layers. So, those equations will be defined as, for the boundary $z = z_1$

$$F_1 = \frac{Z \cdot A}{jsin(kd)} \cdot [v(z_1) - v(z_2)] + jZ \cdot A \cdot tan(k\frac{d}{2}) \cdot v(z_1), \tag{3.34}$$

and for the other boundary ($z = z_2$) will be

$$F_2 = \frac{Z \cdot A}{jsin(kd)} \cdot [v(z_1) - v(z_2)] - jZ \cdot A \cdot tan(k\frac{d}{2}) \cdot v(z_2). \tag{3.35}$$

The circuital model for non-piezoelectric materials is the one depicted in figure 3.6, in which it could be observed how this is similar to the piezoelectric Mason model removing the transformer and the electrical part.

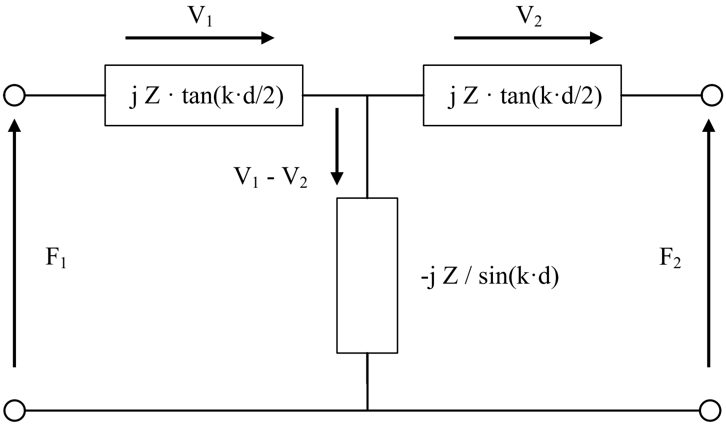

Figure 3.6: Lumped Mason model for a non-piezoelectric layer of thickness d.

Losses could be included in those models by using the complex propagation constant γ instead of the phase constant k

$$\gamma = \alpha + jk, \tag{3.36}$$

where the losses added in the term α are produced by

$$\alpha = \frac{1}{2} \cdot \eta \cdot \omega^2 \cdot \frac{\sqrt{\rho \cdot c}}{c^2}, \tag{3.37}$$

being η the viscosity, ρ the density and c the elasticity of the material [16], [17]. By adding this complex propagation constant, the terms $j \cdot sin(k \cdot d)$ and $j \cdot tan(k \cdot d/2)$ appearing in figures 3.5 and 3.6, will be substituted by $sinh(\gamma \cdot d)$ and $tanh(\gamma \cdot d/2)$ respectively.

In order to simulate a given acoustic resonator, each material layer must be represented with the proper model, cascading the different layers forming the resonator. Figure 3.7 depicts the full modeling of a SMR BAW resonator. This figure shows how the piezoelectric layer, sandwiched between the electrodes, is modeled by using the Mason Lumped Model. The top electrode, the bottom electrode and the layers below that, forming the acoustic reflector are modeled with acoustic transmission lines. The air above the electrode is modeled with an acoustic short circuit, while the substrate is modeled with an acoustic terminating impedance.

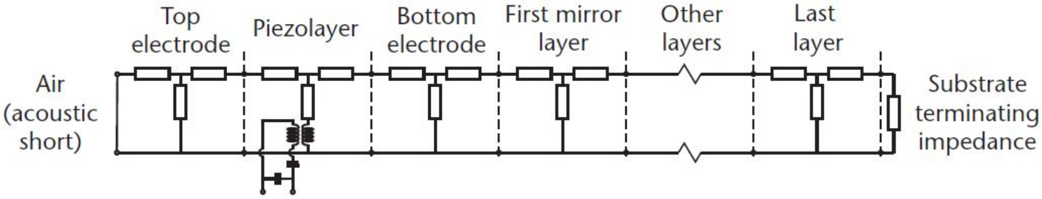

Figure 3.7: Mason model for a multilayer resonator. [20]

3.2.4 Distributed Mason Model

Advanced modeling of acoustic devices could require the discretization of the material in many different cells. The main reason of that is to properly know the intensity of a given field magnitude in the different points along the layer thickness for a local description of the phenomena. This is important for distributed nonlinearities, where the nonlinear effects are locally produced depending of the local field magnitudes.

The Distributed Mason Model is a variation of the lumped one, in which a given layer can be discretized in many elemental cells. Those cells account for electroacoustic interactions and the acoustic wave propagation in the thickness direction. Considering that a given piezoelectric layer of thickness

d is divided in N elemental cells, then the thickness of each elemental cell will be

$$d_z = \frac{d}{N}, \tag{3.38}$$

Every elemental cell has their representation by using this model, depicted in figure 3.8.

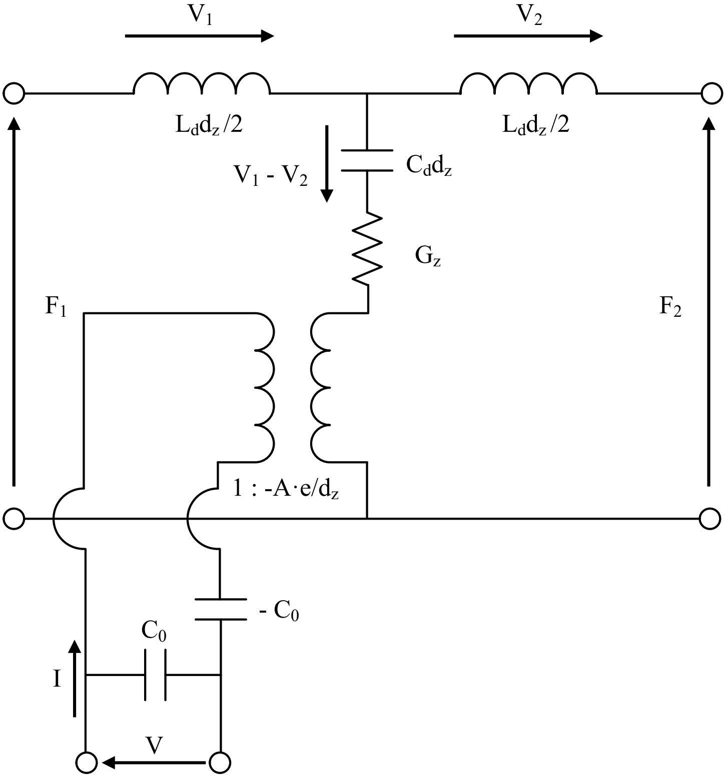

Figure 3.8: Distributed Mason model for a piezoelectric cell of thickness d_z.

Each elemental cell of the distributed Mason model obeys the Telegrapher's equations for an acoustic transmission line with distributed parameters L_d and C_d:

$$L_d = \rho \cdot A, \tag{3.39}$$

$$C_d = \frac{1}{c \cdot A}. \tag{3.40}$$

The material losses are modeled with a conductance G_z, depending on the section of the corresponding cell thickness, the physical area A and the viscosity η

$$G_z = \frac{d_z}{A \cdot \eta}. \tag{3.41}$$

At this point, is important to remark that the C_0 is also scaled by the thickness of each elemental cell

$$C_0 = \frac{\varepsilon^S \cdot A}{d_z}. \tag{3.42}$$

For non-piezoelectric layers, the model is the same but removing all the electrical part, as only a mechanical wave flows through their structure. The model for non-piezoelectric layers is the one depicted in figure 3.9.

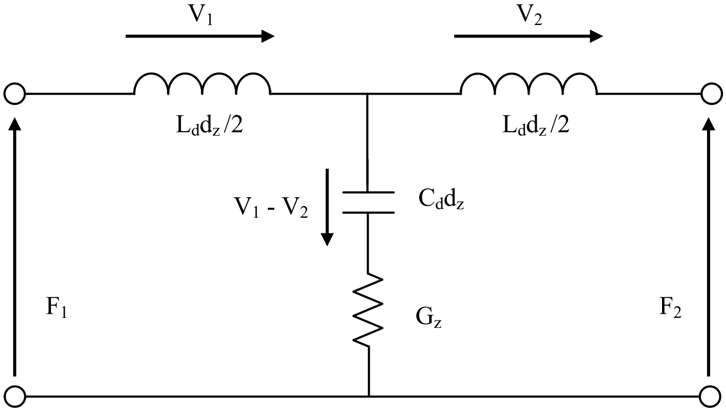

Figure 3.9: Distributed Mason model for a non-piezoelectric slab of thickness d_z.

In order to model the whole layer of a given material, the different elemental cells must be cascaded. Figure 3.10 shows, as an example, the circuital modeling of the piezoelectric layer discretized in N elemental cells.

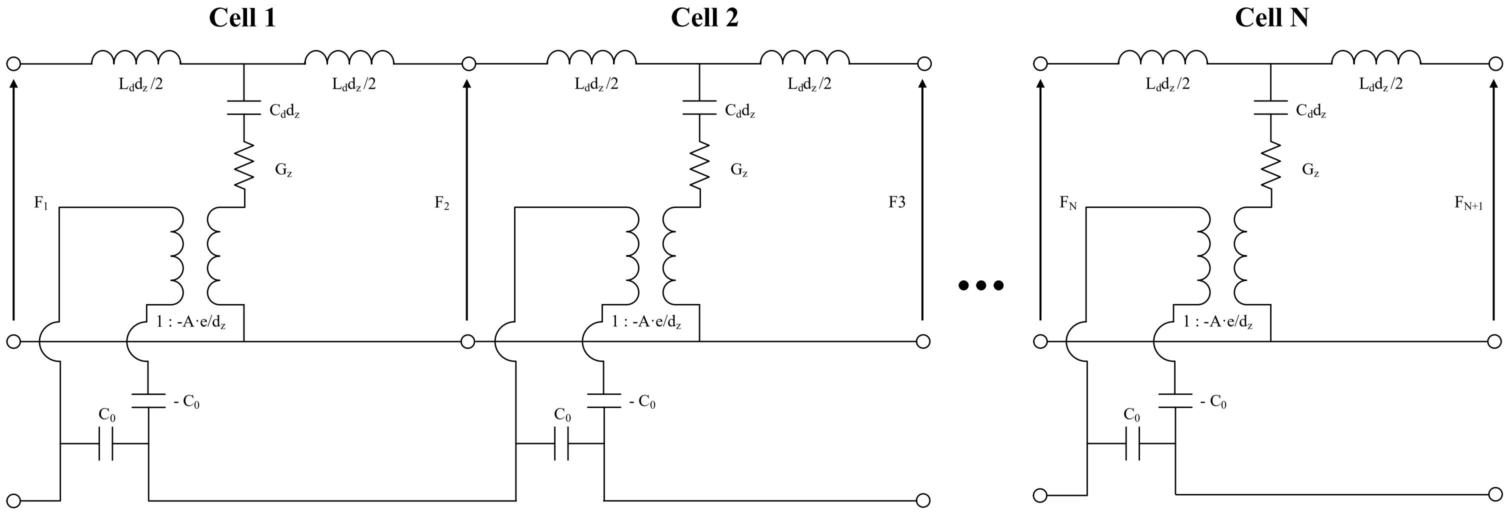

Figure 3.10: Distributed Mason model for a piezoelectric layer of thickness d formed by N elemental cells of thickness d_z.

3.3 Nonlinear Distributed Mason Model

Comprehensive circuital models that account for both linear and nonlinear performances are mandatory for the full modeling of acoustic devices. Past studies proposed different nonlinear distributed models for acoustic devices. In 2010 was published a nonlinear Mason based model applied to piezoelectric resonators [9], [10]. This nonlinear model extended the linear response of the Distributed Mason Model including its nonlinear response. This was made by adding distributed nonlinear voltage sources along its acoustic arm, and one lumped source in the electric terminal. Another variation of the Nonlinear Distributed Mason model exists, in which the electric branch and its nonlinear source is implemented in a distributed form, as seen in figure 3.11. This model can well characterize broadband second- and third-order intrinsic nonlinear responses for any BAW resonator.

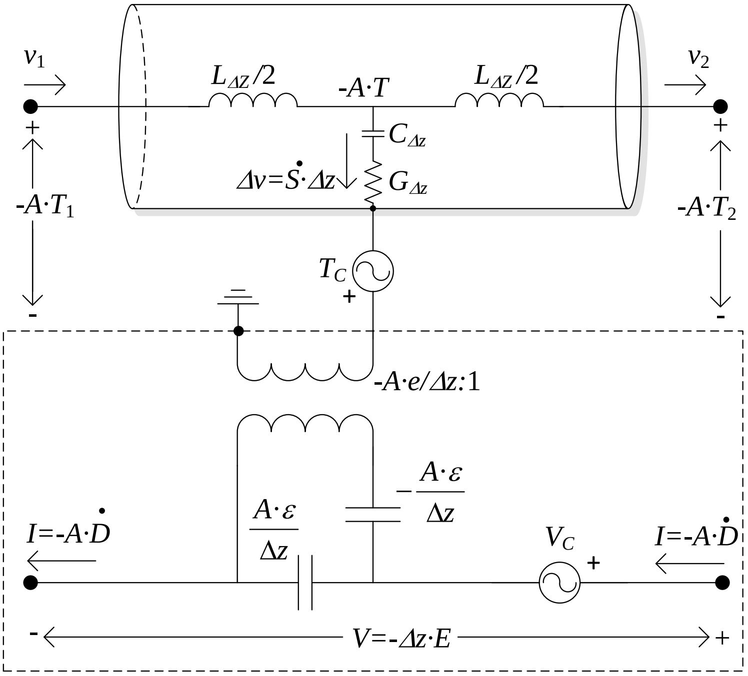

Figure 3.11: Nonlinear unit cell of the piezoelectric layer. [12]

As this model does not take into account the thermal domain, the nonlinear constitutive equations presented in chapter 2 must be simplified only for the mechanical and the electrical domain. The constitutive equations are

$$T = c^E S - eE + \Delta T_{NL}, \tag{3.43}$$

$$D = eS + \varepsilon^S E + \Delta D_{NL}, \tag{3.44}$$

where the intrinsic nonlinear coefficients truncated to a third-order polynomial are

$$\Delta T_{NL} = \frac{1}{2}(c_2^E S^2 - \varphi_3 E^2 + \chi_7 S E^2 - \chi_9 S^2 E) + \varphi_5 S E + \frac{1}{6}(c_3^E S^3 - e_3 E^3), \tag{3.45}$$

$$\Delta D_{NL} = \frac{1}{2}(\varepsilon_2^S E^2 - \varphi_5 S^2 - \chi_7 S^2 E) + \varphi_3 S E + \frac{1}{6}(\varepsilon_3^S E^3 + \chi_9 S^3). \tag{3.46}$$

As it is detailed in [9], the constitutive equations (3.45) and (3.46) can be rewritten for T and E as a function of S and D, which is more appropriate for a Mason implementation

$$T = c^D S - \frac{e}{\varepsilon^S} D + T_c, \tag{3.47}$$

$$E = \frac{D - eS}{\varepsilon^S} - V_c. \tag{3.48}$$

The nonlinear sources T_c and V_c appearing in equations (3.47) and (3.48) are defined by the equations

$$T_c = \Delta T_{NL} + \frac{e}{\varepsilon^S} \Delta D_{NL}, \tag{3.49}$$

$$V_c = \frac{1}{\varepsilon^S} \int_d \Delta D_{NL} dz = \frac{\Delta D}{\varepsilon^S} \Delta d, \tag{3.50}$$

where Δd, for the nonlinear nomenclature, is the thickness of an elemental cell. Those new nonlinear sources T_c and V_c are the consequence of rewriting the constitutive equations for T and E as a function of S and D.

These circuital models have been implemented with Keysight Advanced Design System (ADS). This software provides very interesting components for simulating nonlinear sources. The selected one, is the Symbolically-Defined Devices (SDD). The SDD components are equation-based multi-port components, in which one specifies the time-domain relations between currents, voltages and their derivatives at each port. The nonlinear circuit is solved by using Harmonic Balance (HB) techniques.

Figure 3.12:

3.4 Nonlinear Lumped Mason Model

Figure 3.13:

Figure 3.14:

3.4.1

(3.51)

(3.52)

(a) (b)

Figure 3.15:

Figure 3.16:

(a) (b)

Figure 3.17:

(a) (b)

Figure 3.18:

3.5 Nonlinear BVD Model

Figure 3.19: .

Figure 3.20:

Figure 3.21:

Figure 3.22:

(3.53)

(3.54)

(3.55)

(a) (b)

Figure 3.23:

3.6 Electro-thermo-mechanical Mason Model

In 2013, [12] included the thermal domain in the Nonlinear Distributed Mason Model adding thermal dependent variables to the constitutive equations. Reference [12] obtained the nonlinear relations between the 3 different physical domains (electro-thermo-mechanical) for a piezoelectric material, and then, simplifying it for non-piezoelectric dielectrics and metals. With this model, [12] simulated nonlinear distortion produced by intrinsic effects and thermal effects. This work only makes the basic overview of this model and further information could be found in [12].

The heat wave propagating along the stack is only considered vertically through the thickness direction until it reaches the substrate. In the substrate, commonly Silicon (Si), the heat propagation is considered

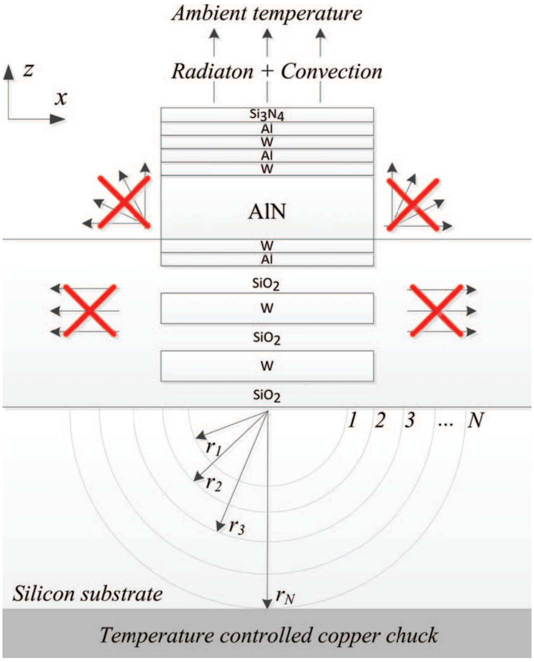

Figure 3.24: Cross-section of a solidly mounted resonator (SMR). The figure also illustrates the thermal considerations for the modeling. The figure is not to scale, and is intended for illustrative purposes only. [12]

semi-spherical, as it can be observed in figure 3.24. At the same time, the model also considers the heat propagated through convection and radiation, although those could be neglected at reasonable power levels.

The electro-thermo-mechanical nonlinear model is the one depicted in figure 3.25. The thermal network, as it has been explained in the previous chapter, is modeled as a lattice RC network. This RC network is the electrical analogy of the heat equation. The thermal resistivity is modeled as a distributed series resistance

$$R_{\theta,\Delta z} = \frac{\Delta z}{A \cdot k}, \tag{3.56}$$

and the heat capacity is modeled as a distributed capacitance

$$C_{\theta,\Delta z} = A \cdot c_p \cdot \Delta z, \tag{3.57}$$

where k is the thermal conductivity and c_p the heat capacity.

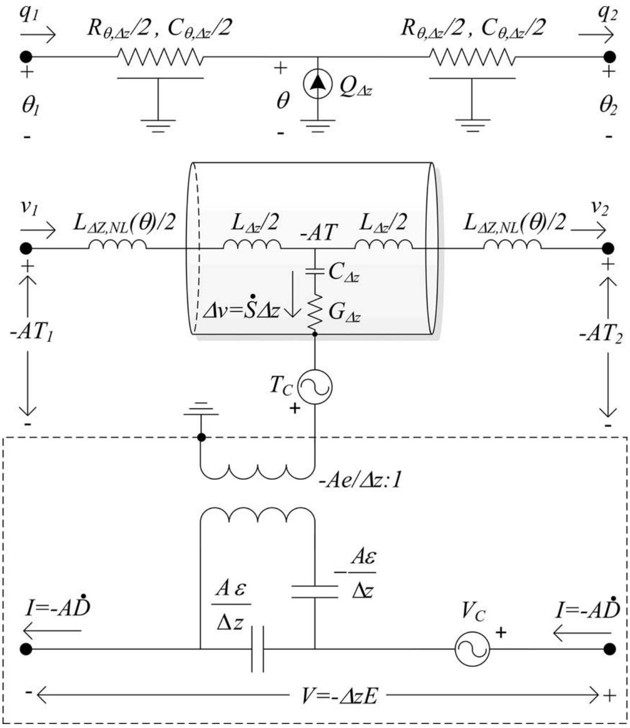

Figure 3.25: Nonlinear unit cell of the Electro-thermo-mechanical Mason model for the piezoelectric layer. [12]

This network allows to make the analogy between the thermal and the electrical domain, where the temperature θ is modeled as a voltage, and the heat rate q as a current. The acoustic losses produced by the viscosity of the material are taken into account, as the main responsible of heat generation. This heat generated inside the device, will be modeled by the thermal source $Q_{\Delta z}$. This makes possible that the model can simulate properly the resonator behavior with temperature changes, including the self-heating effects explained in the previous chapter.

3.7 Concluding Remarks

This chapter has presented one-dimensional models of BAW resonators. It has started by presenting the two preferred ones for the design-stage of acoustic devices: the BVD model and the Mason model.

First of all, the nonlinear models based on the Mason one have been presented:

Finally, the Electro-thermo-mechanical Mason Model described in [12], has been introduced. In this chapter, the basis of the thermal domain in BAW resonators, and how to model it with a circuital model have been introduced.

Chapter 4

Bulk Acoustic Wave Nonlinear Characterization Process

4.1 Introduction

Due to the complexity of the piezoelectric effect and the different materials composing an electro-acoustic device, the origin of the nonlinear effects might be several and it is not straightforward to discern it without a comprehensive circuit modeling and accurate and extensive measurements.

This chapter details the nonlinear characterization process for BAW resonators. To guarantee a unique and comprehensive solution of the nonlinear behavior of BAW devices the main steps required are:

- The use of a distributed circuit model that accounts for the field and nonlinear sources distribution at each layer forming the resonator. Details of those are extensively detailed in chapter 3.
- Broadband measurements of the nonlinear response in order to obtain clues about the origin of the nonlinearities.
- Measurements of different resonators with different characteristics and layer thicknesses. All the measurements must be consistent with a unique set of nonlinear material parameters.

This chapter starts by outlining the nonlinear characterization procedure.

An unavoidable initial step for an unified nonlinear modeling is to accurately emulate the linear broadband response of the resonator. The matching of the measured and simulated input impedances by means of a distributed model is crucial to emulate the field distributions at any point along the stack at the fundamental frequencies, f_1 and f_2, and therefore the distribution of the nonlinear sources along the stack according to [7], [8], [9], [10], [12] and [33]. Those nonlinear sources create spurious signals at given mixed frequencies (for example, $2f_1$ (H2), $3f_1$ (H3), and $2f_1 - f_2$ (IMD3)), whose output powers depend on how their field distributions couple to the load [35].

The characterization process requires different high power measurement systems, in order to measure the different nonlinear spurious signals under study (H2, H3, IMD3). The measurement systems must work at the frequency range of the commercial resonators under study in this work, which have been provided by the company Qorvo, Inc. This chapter details the different designed, implemented and tested nonlinear measurement systems.

The eight different resonators under study in this thesis will be presented. Their linear and nonlinear frequency responses have been measured and modeled for obtaining clues of which nonlinear materials are involved in H2, H3 and IMD3 generation. Those resonators were designed for working at frequencies corresponding to LTE B30 band, LTE B7 band and the Wi-Fi 2.4 GHz band, which correspond to different wireless communication services. These resonators differ on their areas, shapes, and layer thicknesses.

4.2 Nonlinear Characterization Process

Accurate and comprehensive characterization of the linear and nonlinear response on BAW resonators, is indeed a crucial point in order to identify the contribution to the harmonic and intermodulation products generation. In order to do that, several steps must be taken into account for a carefully analysis on the generation of those undesired spurious signals.

The use of a distributed circuit model modeling the propagation of the acoustic wave in the direction of the thickness, is required. The Nonlinear Mason Model, presented in chapter 3, is the best candidate for that purpose, and concretely the Nonlinear Distributed Mason Model in which the nonlinear equations are defined in the time domain. All the nonlinear analysis done in the following chapters, has been carried out by using this model, discretizing the piezoelectric layer in 60 elemental cells and the non-piezoelectric layers in 100 cells.

Another crucial step is to make broadband measurements of the nonlinear response in order to obtain clues about the origin of the nonlinearities. This work will confirm later the importance of that step, by demonstrating that some spurious resonances appearing in the linear response at higher frequencies, could have some impact in the narrowband nonlinear response of the resonator. Undesired signals generated in other layers than the piezoelectric layer could be enhanced by the presence of spurious resonances in the linear response at higher frequencies. Identification of the material involved and the layer generating those out-of-band resonances is a must in the nonlinear characterization process for a full-modeling of BAW resonators.

The last significant step when modeling nonlinearities in BAW devices is to perform measurements of different resonators with different characteristics and layer thicknesses and configurations. This step is crucial, and reveals that some of the spurious signals are enhanced depending on the thicknesses of certain layers. By looking at the different characteristics between them, we could have a first idea on where the harmonics and PIM are generated, giving this some clues of the problem. In this work, different resonators with different characteristics have been analyzed.

Once the resonators under study are measured, the next step is to identify, by using the nonlinear models implemented in ADS, the materials producing some degree of nonlinearity in the resonator. For that, the procedure will consist on the following steps.

1. Assume a narrowband characterization of a test resonator. The general consensus in [9], [10] and [12], states that the most important parameter in the generation of H2 around the main resonance is the term φ_5 (in 3.50). We will analyze if this parameter is suitable to properly model nonlinearitiries around resonance, including some strange spurious resonances appearing near that frequency for some resonators.
2. Then, by the use of a broadband characterization, we will discern between different sources of nonlinearities. We will check what materials are involved in the generation of spurious nonlinear signals by activating their nonlinear parameters and comparing the out-of-band H2 with the broadband measurements.
3. Once the possible candidates are identified as potential nonlinear sources, we will discern between them using the values obtained in different measurements of different resonators. The candidates reproducing H2, H3 and IMD3 measurements for all the resonators will

tell us which material is the one producing some degree of nonlinearity at a given frequency range.

This procedure has allowed us to achieve new relevant conclusions about the nonlinear sources contributing to different observable.

4.3 Nonlinear Measurement Systems

In order to characterize the nonlinear behavior of BAW resonators different high power measurement systems are required. This is mandatory to properly measure the different type of nonlinearities, like H2, H3 and IMD3 among others.

4.3.1 H2 Measurement System

Figure 4.1 shows the configuration of the measurement system designed for measuring the H2 response.

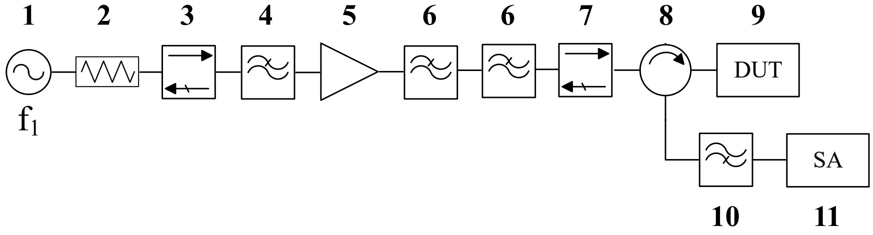

Figure 4.1: H2 measurement system scheme.

This architecture is composed by the following devices:

1. Signal source controlled with MATLAB.
2. 10 dB Attenuator. In order to protect the power amplifier input.
3. Isolator. In order to protect the signal source from reflections.
4. 2.85 GHz Low Pass Filter (LPF). In order to filter the harmonic distortion generated by the source.
5. Power Amplifier (PA). In order to create the high power signal to drive the DUT.

6. 3 GHz LPF. In order to filter the harmonic distortion generated by the PA.
7. Isolator. In order to protect the amplifier output from reflections.
8. Circulator (from 2 GHz to 6 GHz). In order to guide the high power signal to the DUT and the reflected signal coming from this to the spectrum analyzer.
9. DUT. In our case, is the BAW resonator.
10. 2.85 GHz High pass filter (HPF). In order to filter the fundamental signal, allowing only the pass of the H2 through the path.
11. Spectrum Analyzer (SA). In order to measure the harmonic distortion power level.

In order to measure harmonic distortion accurately, the measurement system has been calibrated and characterized properly. For that, the system characterization has been done in 2 steps. Firstly, a 3 ports S-parameters measurement of part of the system, from the circulator until the DUT and the SA, has been obtained. This characterization has been realized with a vector network analyzer (VNA), and the S-parameters have been obtained in a touchstone file format, represented in ADS with a 3 port data item. Figure 4.2 (a) shows the insertion losses (IL), where the main contribution of this arises from the circulator and the transitions used. Figure 4.2 (b) shows the IL from the DUT to the SA, where the attenuation of the HPF starting from 2.85 GHz can be observed.

In the second step, a calibration of the input power at port 1 has been done. This calibration accounts for the other components not included in the measured S-parameters. Therefore, a power characterization from the signal source to the LPF output has been realized. In ADS, this part has been simulated with a 2 port data item. One port is connected to an ideal source (with the same power level) in order to simulate different frequency input signals, and the other to the first input of the 3 port data item containing the S-parameters. Figure 4.3, shows the measured power at the input of the 3 port S-parameters system measured as a function of frequency. The power of the signal generator is set to 0 dBm.

In order to perform H2 measurements, the nonlinearities of the own system must be characterized. Figure 4.4 shows the H2 measured at the SA, where the x-axis of the figure is the central frequency of the fundamental tone. The maximum H2 level is less than -75 dBm in a given

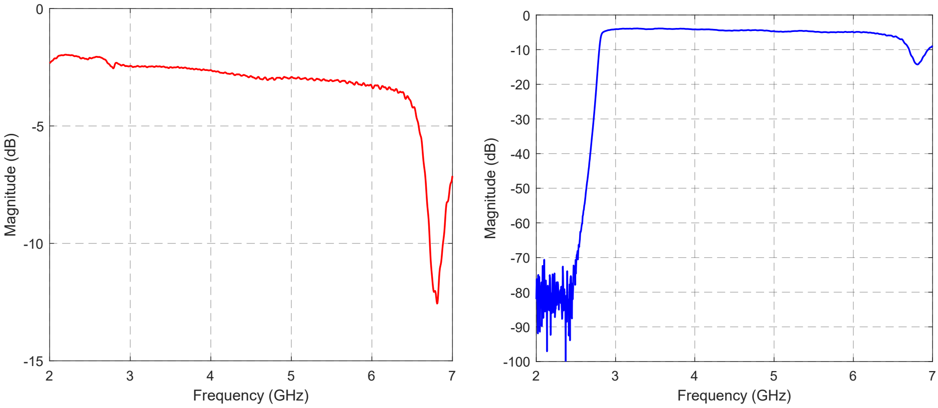

(a) Insertion Losses from Circulator Input to DUT (S21) (b) Insertion Losses from DUT to SA (S32)

Figure 4.2: Scattering Parameters Measured of the H2 Measurement System

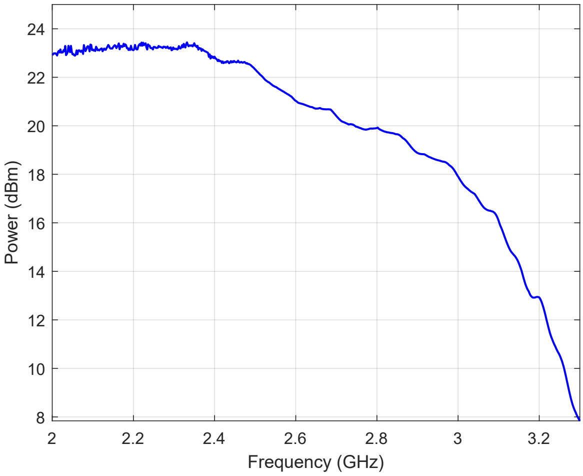

Figure 4.3: Measured power for the fundamental tone at LPF input.

spurious frequency, but the H2 mean power level for the measurement system is around -85 dBm. With this H2 level, the system is prepared for measurements, since H2 levels generated by the resonators will be higher than this.

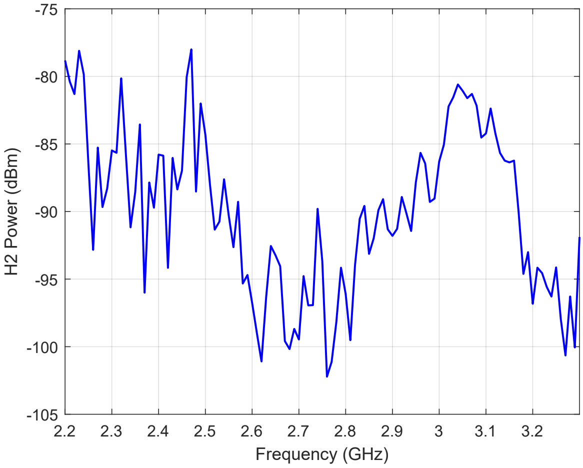

Figure 4.4: H2 measured power at the SA input, generated by the own measurement system.

4.3.2 IMD3 and H3 Measurement System

Figure 4.5 shows the implemented configuration in order to measure the third-order intermodulation products. In this case we cannot use HPF to filter the high power fundamental tones before they go into the SA because the IMD3 is too close to the fundamental signals. Therefore, is mandatory to guarantee than the measured IMD3 is coming from the DUT and not from the SA setting up the internal attenuator of the SA to high enough levels.

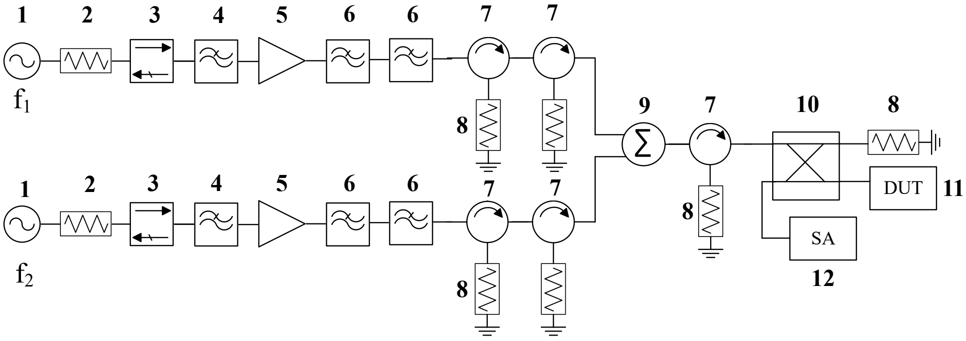

Figure 4.5: IMD3 and H3 measurement system scheme.

This architecture is composed by the following devices:

1. Signal sources controlled with MATLAB in order to generate the two fundamental tones f_1 and f_2.

2. 10 dB attenuator in order to protect the power amplifier input.
3. Isolator. In order to protect the signal source from reflections.
4. 2.85 GHz LPF. In order to filter the harmonic distortion generated by the source.
5. PA. In order to create the high power signal to drive the DUT.
6. 3 GHz LPF. In order to filter the harmonic distortion generated by the source.
7. Circulator. In order to guide the high power signal to the DUT and avoid the reflected high power signals to the previous devices.
8. 50 ohm load. In order to avoid undesired reflections in the system.
9. Combiner. In order to combine the signal coming from 2 different branches.
10. Hybrid. 90° Hybrid in order to guide the combined signal to the DUT, and then, the reflected signal to the SA.
11. DUT. In our case, is the BAW resonator.
12. SA. In order to measure the intermodulation distortion power level.

Accurate calibration and characterization of the measurement system is required. For that, a 4-port S-parameters of all the system, from the outputs of the signal sources of 1 (first port) and 2 (second port) until the DUT (third port) and the SA (fourth port), have been obtained. The S-parameters have been obtained in a touchstone file format to export the measured data to ADS, simulated with a 4 port data item.

Figure 4.6 (a) shows the return losses (RL) for the port 3 in blue line, and the IL from port 3 to 4, in order to know the loss of power in the signal path (hybrid and different cables and transitions) from the DUT to the SA. The ripple in the RL is due to mismatch of the broadband hybrid generating standing waves in the cables. Figure 4.6 (b), shows the IL in the signal path from port 1 to port 3 (S31) and port 2 to port 3 (S32). Also, it shows the good isolation between input ports 1 and 2 and the SA (S41 and S42).

In order to characterize the IMD3 and the H3 generated in the measurement system and the amount of reflected power coming from the DUT for the fundamental tones, the DUT is replaced by an open circuit.

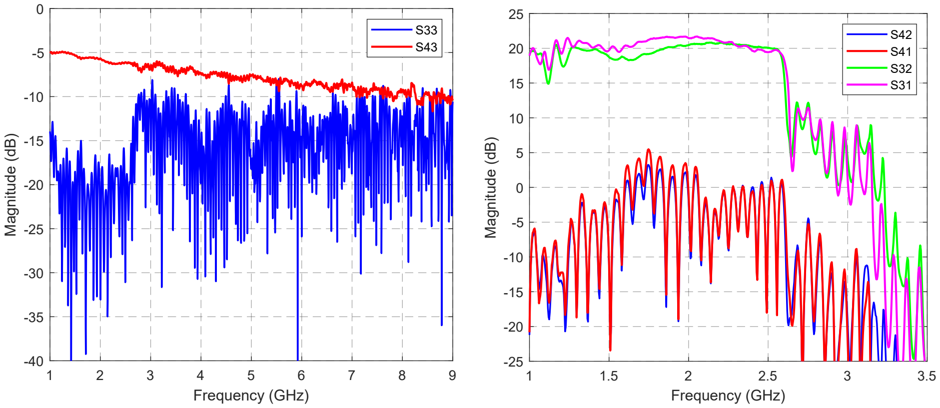

(a) Return Losses at DUT port (S33) and Insertion Losses from DUT to SA (S43)

(b) Isolation between signal sources (2 and 1) and SA (S42 and S41, respectively) Insertion Losses from signal sources 2 and 1 to DUT (S32 and S31, respectively)

Figure 4.6: Scattering Parameters Measured of the IMD3 and H3 Measurement System.

With this type of termination, the reflected power is maximum, similar to the resonator case, which is very reflective, with a reflection coefficient close to 1. Figure 4.7 shows the power level of the fundamental tones measured at the SA input. Setting an output power of 5 dBm at the signal sources, the mean power level at the SA input is around 21 dBm. This power is less than the maximum no damage input power for the SA, which is 30 dBm.

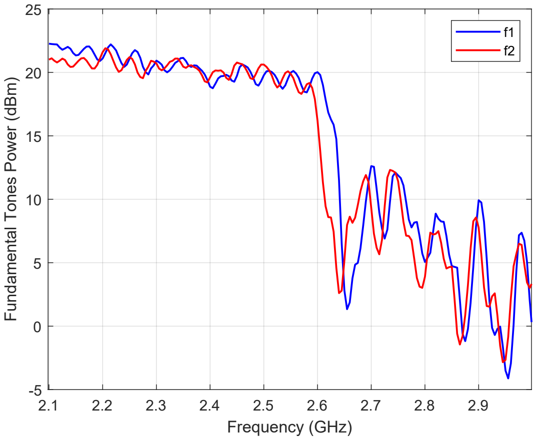

Figure 4.7: Fundamental tones measured power at the SA input.

Figure 4.8 (a) shows the measured IMD3 at the SA, where the x-axis of the figure is the central frequency of the two tones and the separation between them is set to 2 MHz. The maximum IMD3 level is around -75 dBm at specific frequencies, but the IMD3 mean power level for the measurement system is around -85 dBm. With this IMD3 levels, the system is ready to measure, since IMD3 levels generated by BAW resonators will be higher than this. For the H3 ($3f_1$), the mean power level generated by the own system is around -88 dBm. Although this power level is not quite good, it will be enough for measuring H3 around resonance in BAW devices.

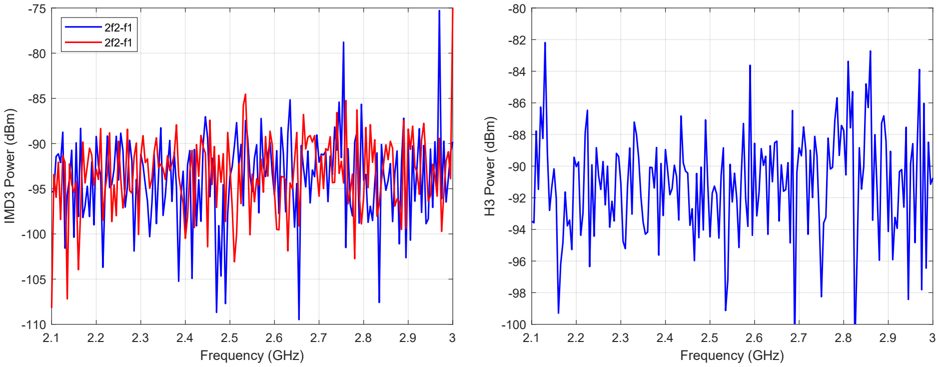

(a) IMD3 power level

(b) H3 power level

Figure 4.8: IMD3 and H3 measured power at SA input, generated by the own measurement system.

Thanks to this characterization process, we can conclude that this measurement system is able to measure IMD3 higher than -85 dBm and H3 above -88 dBm (for input power to DUT around 21 dBm) from 2.1 GHz up to 3 GHz. The implementation and assembly of the IMD3 measurement system in the UPC lab is the one observed in figure 4.9.

Figure 4.9: IMD3 measurement system configuration in the UPC RF laboratory, CSC-EETAC.

4.4 BAW Resonators Under Study

The results presented along the following sections correspond to eight different on-wafer BAW resonators. Those resonators, provided by the US company Qorvo Inc., differ between each other, not only in the layer thicknesses, but in other physical aspects, such as apodization, inclusion of Border Ring, conductor of the pads, etc.

Although being eight different SMR BAW resonators, all of them present equal material distribution along the stack with different thicknesses, accommodated to provide a proper linear response. The layer distribution of the resonators is outlined in figure 4.10. The physical properties of the different materials used along the stack are detailed in appendix B.

The eight resonators can be classified into three different groups. Each group consist of two resonators, which would correspond to a series and a shunt resonator of a ladder configuration filter. Each group of resonators has

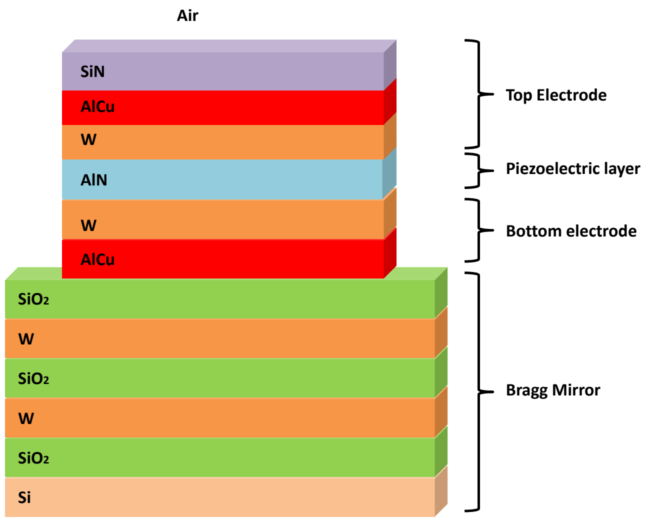

Figure 4.10: Stack configuration of the measured SMR BAW devices.

Table 4.1: BAW Resonators Characteristics

Resonators	Mode	Band	Series	Shunt
R1	Wi-Fi	2.4 GHZ	✓	
R2	Wi-Fi	2.4 GHZ		✓
R3	LTE-FDD	B7	✓	
R4	LTE-FDD	B7		✓
R5	LTE-FDD	30	✓	
R6	LTE-FDD	30		✓
RA	LTE-FDD	30	✓	
RB	LTE-FDD	30		✓

been designed to operate at different frequency ranges, which correspond to different communication services. Table 4.1 identifies each resonator with different names for the sake of clarity.

Figure 4.11 depicts the measured resonators. As it can be observed, those resonators differ on their areas and shapes. R1, R2, R3 and R4 are apodized, in order to avoid the typical lateral modes appearing in BAW devices [36] and [37]. Although the knowledge of the exact dimension and layer thicknesses of the resonators are mandatory for a proper modeling of the devices, those cannot be disclosed here for confidential reasons.

(a) R1 (b) R2 (c) R3

(d) R4 (e) R5 (f) R6

(g) RA (h) RB

Figure 4.11: BAW resonators under study, designed and manufactured by Qorvo, Inc.

As an example, figure 4.12 illustrates the agreement between the measured and modeled responses for resonator R5. Fine tuning within the manufacturing tolerances of layer thicknesses from the given nominal values has been performed in order to provide an accurate fitting through the whole measured frequency range. The broadband (from 1 to 9 GHz) input impedance phase demonstrates the accuracy of the modeling on following all the resonances appearing along the whole frequency range.

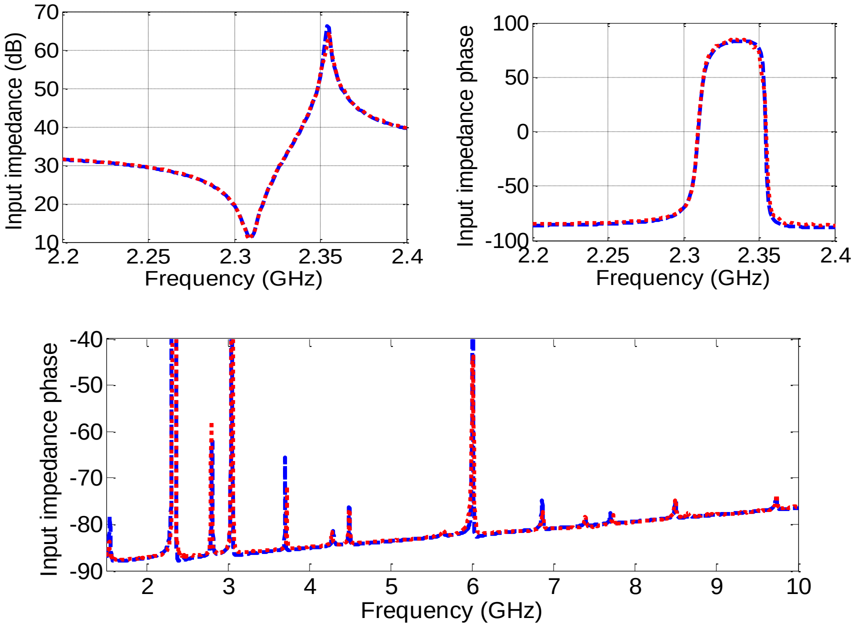

Figure 4.12: Simulated (blue dashed line) and measured (red dotted line) narrowband (top) and broadband (bottom) input impedance of R5.

It is worth mentioning that R5, R6, RA and RB significantly differ from the other four resonators in the thickness of the SiO_2 layers, which is set considerably thicker. The reason of that is because those resonators were designed as TC-BAW resonators. Mostly, temperature coefficients of the stiffness constant in materials used for designing AW technology are negative, as is explained in [20]. This means that, for that materials, as temperature rises, the stiffness constant of those materials decreases, because it is inversely proportional to temperature. Thus, the linear behavior of the resonator will change, suffering frequency shifting as temperature changes, and degrading the system performance of the whole communication chain. TC-BAW resonators are able to compensate those temperature changes by using oxide films in the stack of these devices. Oxide films (for example, SiO_2 films) have positive temperature coefficients of the elastic constant. By adding these films in AW devices, the frequency drift due to temperature changes will be improved, being the TC-BAW resonators able to cancel out all or most of them.

4.5 Second-Order Nonlinear Characterization

A main concern in BAW resonators is about the second-order nonlinearities, which are usually characterized by H2 generation. Broadband simulations of the H2 response exhibit different frequency pattern when sweeping the frequency depending on the material that is considered nonlinear. Such a difference allows to relate the H2 measurements to a given nonlinear material. Furthermore, the same nonlinear parameters may cause different nonlinear effects, such as H2 and DC detuning, and the measurements of those effects must be consistent with the simulations. In particular, an accurate analysis of the contribution of each layer of the stack on the nonlinear performance is presented, by means of three different experiments: narrowband H2, broadband H2, and DC detuning. These experiments will help, allowing a unique identification of the physical origin of the H2 generation.

Table 4.2: Nonlinear coefficients published in previous works

Nonlinear coefficient	Value
φ_5	$-17 \cdot e$
$c^E_{3,AlN}$	$-111 \cdot c^D$

The works published in [8], [9], [10], [12], [33] and [34] state that the main responsible for H2 generation was the nonlinear coefficient φ_5 (δ_1 in [9], [10]), which sets the strain-dependent piezoelectric constant, or the electric field-dependent elasticity due to equivalent second-order interactions between physical domains. In fact, despite φ_5 having an effect on V_c and T_c from equations (3.49) and (3.50), according to [7] [8], [9] and [33], the main contributor to the H2 level at this frequency is the nonlinear source V_c. On the other hand, those works stated too that the main responsible for IMD3 generation was the nonlinear coefficient $c^E_{3,AlN}$. Both nonlinear terms and their values are shown in table 4.2.

Figures 4.13 and 4.14 shows the measured and simulated H2 for resonators R1, R2, R2 and R4. The x-axis indicates the frequency of the fundamental signal, f_1, and the y-axis the power measured at the frequency corresponding to the H2, $2f_1$. As it could be observed, the nonlinear term φ_5 is able to reproduce with good agreement the H2 response around resonance for all of them.

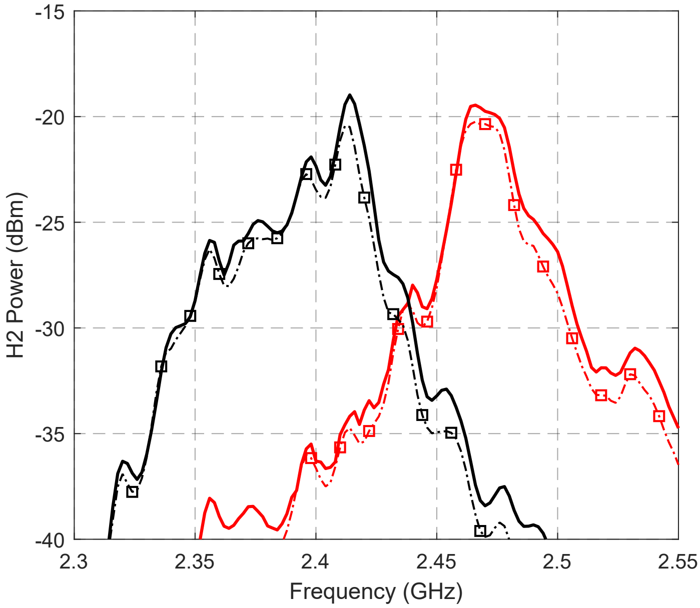

Figure 4.13: H2 ($2f_1$) measurements (thick lines) and simulations (dotted-dashed squared lines) for the Wi-Fi resonators. This includes R1 (red) and R2 (black).

4.5.1 Silicon Dioxide Role in the Second-Order Nonlinear Response

Figure 4.15 shows the measured H2 response for R5 resonator, with a DUT input power of 21 dBm. As expected, there is a maximum at a frequency above the series resonance of 2.32 GHz. At this frequency, the stress is maximum inside the piezoelectric layer [8].

The smooth ripple appearing is due to the measurement system and its measured effect is included in the simulation [34]. The simulation matches the measured response related to the main resonance (peak at 2.34 GHz), but fails to model the additional peak appearing at 2.245 GHz. To understand where this peak is coming from, we have to consider the out-of-band resonances present in the broadband input impedance of the resonator.

As it can be seen in figure 4.12 of the previous chapter, a small resonance appears at twice that frequency 4.49 GHz. There is an acoustic resonating mode at 4.49 GHz, which is able to interact with H2 of the driving tone at 2.245 GHz. As the mode couples to the electrical domain, the H2 measurement shows a high peak in figure 4.15. As the high frequency

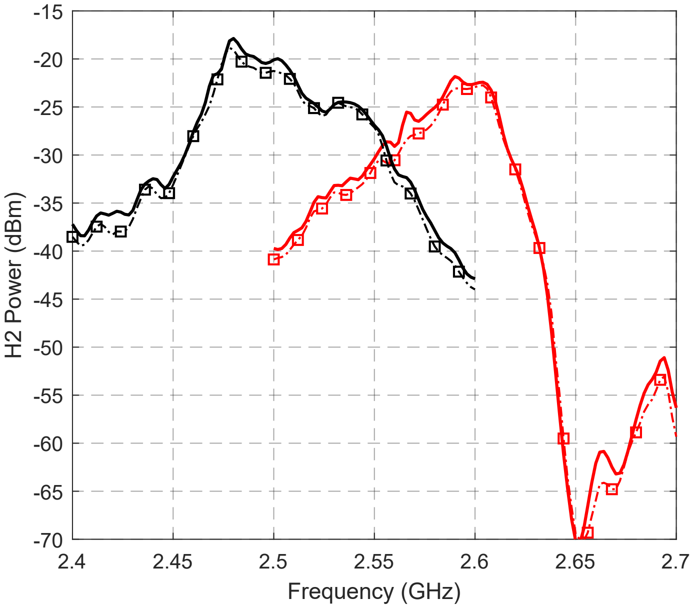

Figure 4.14: H2 ($2f_1$) measurements (thick lines) and simulations (dotted-dashed squared lines) for the B7 resonators. This includes R3 (red) and R4 (black).

out-of-band resonances are strongly dependent on the stack configuration, the linear response must be accurately modeled to reproduce this effect in simulations. At a first glance, the term c_2^E of the piezoelectric constant can produce this high peak, as shown in figure 4.15. The pair of values $c_{2,AlN}^E = -32.2 \cdot c_{AlN}^E$ and $\varphi_{5,AlN}^{'} = -23.8 \cdot e_{AlN}$ reproduce the measured frequency pattern.

Nevertheless, the nonlinear term of the elastic constant $c_{2,AlN}^E$ is not the unique able to produce this effect. A nonlinear elastic constant for the SiO_2 with $c_{2,SiO_2} = -6.4 \cdot c_{SiO_2}$ can produce the same effect, as shown in figure 4.15. In the latter case, the nonlinearities of the AlN are set to $\varphi_{5,AlN}^{''} = -18.7 \cdot e_{AlN}$ and $c_{2,AlN}^E = 0$. In this case, we have checked through simulations that the SiO_2 layer placed just underneath the bottom electrode is the predominant SiO_2 layer causing this H2 peak.

It is clear that additional measurements must be done to discern between those two working hypotheses: $(\varphi_{5,AlN}^{'}, c_{2,AlN}^E)$ and $(\varphi_{5,AlN}^{''}, c_{2,SiO_2})$.

Broadband H2 measurements can help since the standing wave pattern at higher frequencies changes considerably within the stack. Figure 4.16 shows the measured H2 from 2.1 to 3.2 GHz. As it can be seen, high

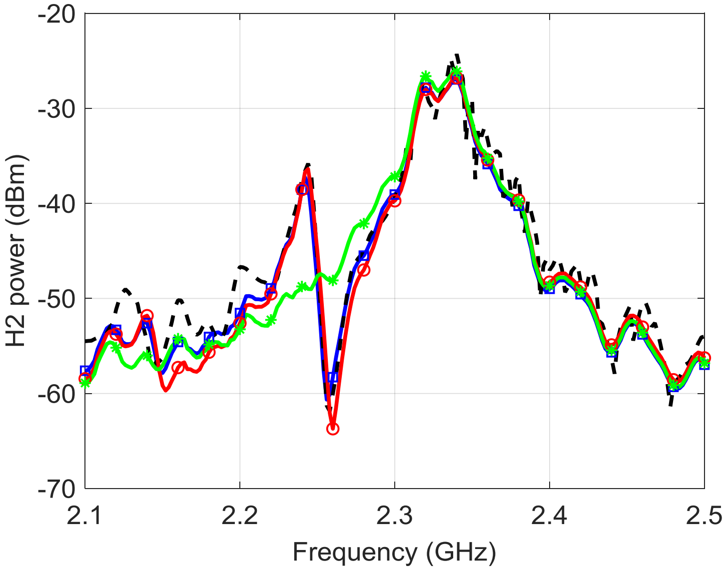

Figure 4.15: Measured (black dashed line) and simulated H2 for the R5 in the following cases: only $\varphi_{5,AlN}$ (green asterisks), $\varphi'_{5,AlN}$ and $c^E_{2,AlN}$ (red circles), and $\varphi''_{5,AlN}$ and c_{2,SiO_2} (blue squares).

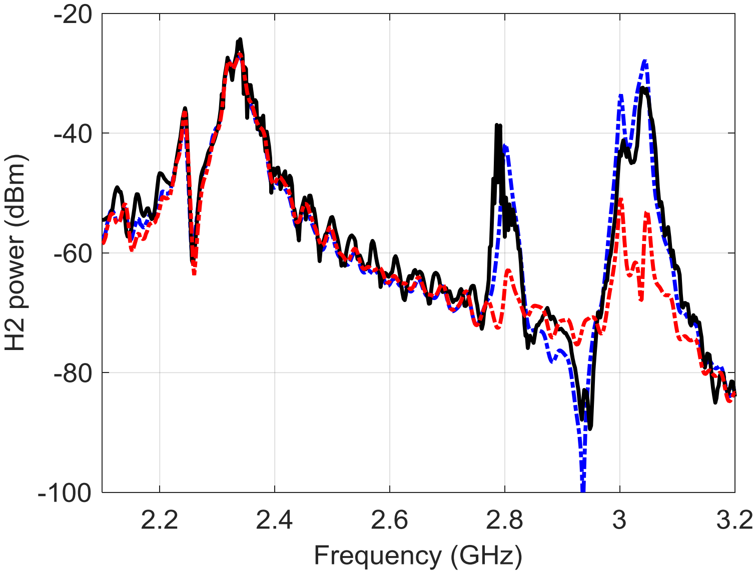

Figure 4.16: Measured (black solid line) and simulated broadband H2 for the R5 in the following cases: $\varphi'_{5,AlN}$ and $c^E_{2,AlN}$ (red dashed line), and $\varphi''_{5,AlN}$ and c_{2,SiO_2} (dotted blue line).

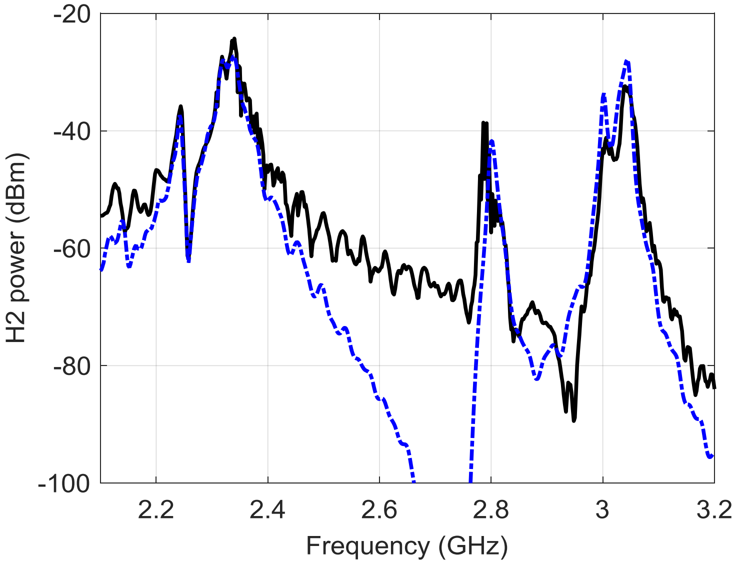

Figure 4.17: Measured (black solid line) and simulated broadband H2 for the R5 in the case $\varphi''_{5,AlN}$ and c_{2,SiO_2} without ε_2^S (dotted blue line).

H2 peaks appear at 2.8 and 3 GHz. Note that the AlN nonlinear term $c^E_{2,AlN}$ cannot reproduce them, and the SiO_2 term c_{2,SiO_2} creates excellent agreement with measurements. It is worth mentioning that in both scenarios we have introduced a nonlinear term for the AlN dielectric constant. The term $\varepsilon_2^S = 20 \cdot \varepsilon^S \cdot e_{AlN}/c^E_{AlN}$ must be taken in consideration to reproduce the out-of-resonance plateau of the H2, as shown in figure 4.17.

4.5.2 Resonator Detuning Applying a DC Signal

This experiment consists on S-parameters measurements while a DC bias voltage is applied at the electrodes. This must provide consistent results for the hypothesis of the H2 generation due to the SiO_2 layers. This experiment is of remarkable interest since the SiO_2 layers are not subject to the static electric field between electrodes.

Although the nonlinear model we are using is able to simulate the effects of a DC bias applied voltage, we have also derived new closed-form expressions, whose derivation is detailed in chapter 2. As a consequence, linear simulations may account for an applied DC voltage just by replacing the constants c^E_{AlN}, e, and ε^S by the terms

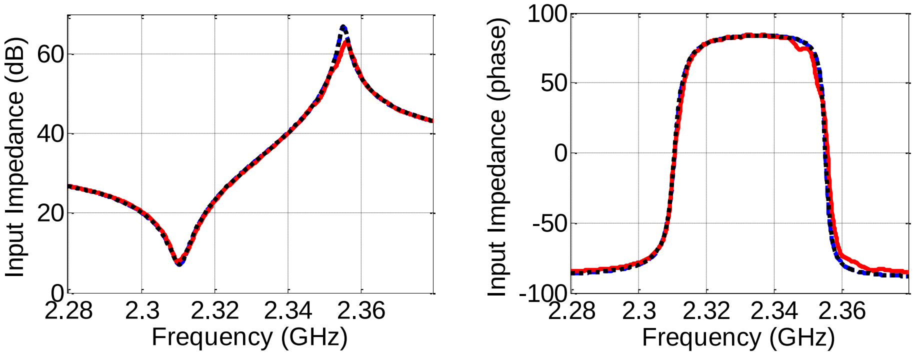

Figure 4.18: Input impedance with +25 V DC voltage for resonator R5: measured (red solid line), HB simulation (black dotted line), and closed-form expression (blue dashed line).

$$c^{E,DC} = c^E \left(1 - \frac{c_2^E e}{(c^E)^2 d} V_{DC} + \frac{1}{2}\frac{c_3^E e^2}{(c^E)^3 d^2} V_{DC}^2 - \frac{\varphi_5 e}{c^E d} V_{DC}\right), \tag{4.1}$$

$$e^{DC} = e\left(1 + \frac{\varphi_5}{c^E d} V_{DC}\right), \tag{4.2}$$

$$\varepsilon^{S,DC} = \varepsilon^S \left(1 - \frac{\varepsilon_2^S}{\varepsilon^S d} V_{DC}\right). \tag{4.3}$$

In order to validate the closed-form equations, figure 4.18 shows the measured and simulated input impedance for an applied voltage of +25 V to R5. HB simulations using the nonlinear model and linear simulations using the formulation described in equations (4.1) - (4.3) overlap perfectly.

Figure 4.19 shows the frequency shift of the series and shunt resonances in parts per million for a voltage ranging from -25 to 25 V, and simulations using (4.1) - (4.3) for both hypotheses. The hypothesis ($\varphi'_{5,AlN}$, $c^E_{2,AlN}$) overestimates the frequency shift in comparison with measurements. On the other side, when the hypothesis of ($\varphi''_{5,AlN}$, $c_{2,SiO2}$) is assumed, simulations and measurements perfectly overlap. This is the third and simplest independent experiment that confirms the hypothesis ($\varphi''_{5,AlN}$, $c_{2,SiO2}$). Using the provided formulation, a DC-experiment is a fast test to set

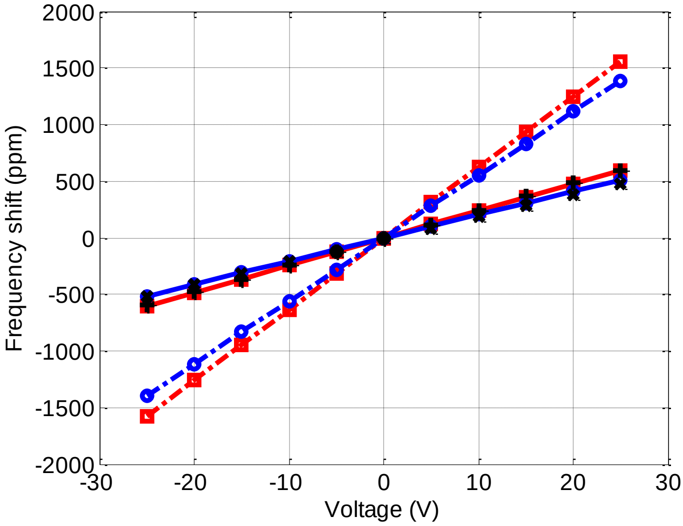

Figure 4.19: Frequency shift of series (red squares) and shunt (blue circles) resonances in parts per million of measured series resonance (black plus sign) and shunt resonance (black times sign), and simulations under $(\varphi'_{5,AlN}, c^E_{2,AlN})$ hypothesis (dashed lines) and $(\varphi''_{5,AlN}, c_{2,SiO2})$ hypothesis (solid lines) for R5.

the magnitude of $\varphi''_{5,AlN}$ and it does require neither complex measurements nor nonlinear simulations. However, this experiment by itself does not give any information about the nonlinearities coming from the SiO_2 layers, which play a significant role in the generation of harmonics and intermodulation products as shown earlier.

4.5.3 Impact of other Materials in Second-Order Nonlinear Response

Although the hypothesis of the second-order nonlinear stiffness constant is becoming stronger with the experiments carried out, other materials, such as the aluminum copper ($AlCu$) or the tungsten (W), could also contribute to the nonlinear generation. In order to analyze the contribution of these materials to the H2 response, the linear and nonlinear response for RA and RB resonators will be modeled. Although being very similar to R5 and R6 resonators, their linear responses differ due to the difference between their layer thicknesses.

Results of measurements and modeling of the linear response of both resonators, RA and RB, are shown in figure 4.20 (a) and 4.20 (b),

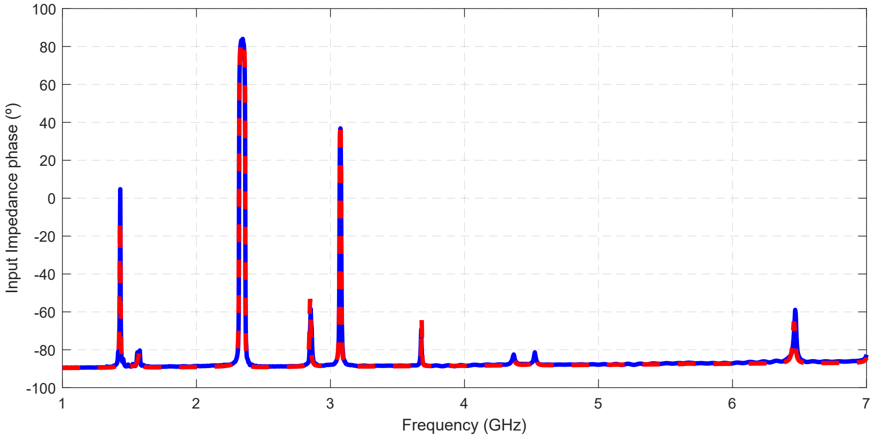

(a) RA

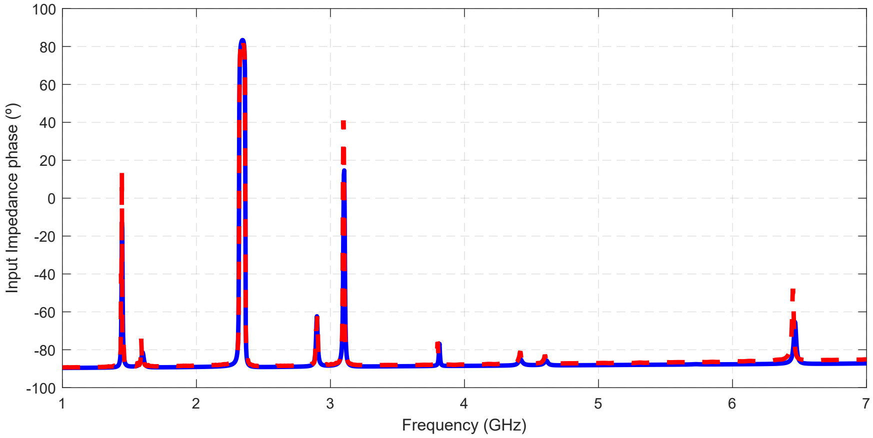

(b) RB

Figure 4.20: Broadband phase frequency response of the two test resonators. Red dashed line indicates to the measurement results and blue line indicates the modeled response.

respectively. Figure 4.20 depicts the phase frequency response from 1 GHz to 7 GHz, showing very good agreement between measurement and modeling over the whole frequency range. Additionally, figure 4.21 details on the frequency response of the two resonators around twice the resonance frequency (from 4.2 GHz to 4.8 GHz). Difference between the frequency response of both resonators in this frequency range will certainly affect the H2 response around the main resonance. In particular the spurious mode that exists just below twice the main resonance indicated with an arrow in

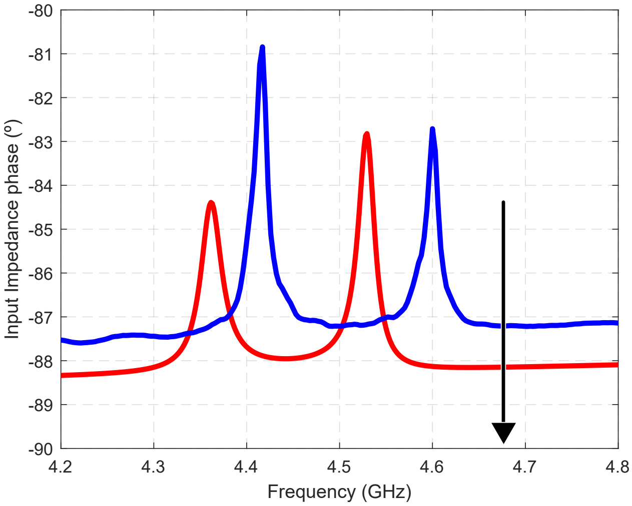

Figure 4.21: Detail response of both resonators RA (red line) and RB (blue line) around twice the fundamental resonance (indicated with an arrow).

figure 4.21 will require of special attention. This spurious mode appears at 4.52 GHz for RA and at 4.60 GHz for RB.

The two resonators are now characterized in terms of their narrowband nonlinear responses by means of measuring the H2, when the fundamental tone is swept from 2.2 to 2.5 GHz. The experiment consists on feeding the resonator with a fundamental tone, f_1, and measuring the output power at the second harmonic $2f_1$. Note that the driving fundamental frequency goes from way below the main resonant mode (at 2.34 GHz) to way above the main resonant mode.

Table 4.3: Second-Order coefficients for the different hypothesis

Hypothesis	ε_2^S	φ_5	$c^E_{2,AlN}$	c_{2,SiO_2}	$c_{2,W}$	$c_{2,AlCu}$
AlN	$20\cdot\varepsilon^S\cdot e_{AlN}/c^E_{AlN}$	$-23.8\cdot e_AlN$	$-32.2\cdot c^E_{AlN}$	0	0	0
SiO_2	$20\cdot\varepsilon^S\cdot e_{AlN}/c^E_{AlN}$	$-18.7\cdot e_AlN$	0	$-6.4\cdot c_{SiO_2}$	0	0
W	$20\cdot\varepsilon^S\cdot e_{AlN}/c^E_{AlN}$	$-5.07\cdot e_AlN$	0	0	$-320\cdot c_W$	0
$AlCu$	$20\cdot\varepsilon^S\cdot e_{AlN}/c^E_{AlN}$	$-18.7\cdot e_AlN$	0	0	0	$320\cdot c_{AlCu}$

When analyzing a potential contributing material NP, its parameter $c_{2,NP}$ is adjusted to match the H2 response around resonance. The parameter φ_5 of the *AlN* is also fine-tuned since the $c_{2,NP}$ also contributes to the level of H2. Figures 4.22 a and b show the adjustment of the narrowband H2 response for RA and RB resonators for the $c_{2,NP}$ values given in table 4.3. The resonator RB shows a higher undesired H2 peak around -30 dBm below resonance than the resonator RA (-40 dBm). The reason is that the first shows a spurious resonance at 4.6 GHz and the second at 4.52 GHz, as it has been mentioned before (see details in figure 4.21). Those resonances enhance the signal level coupled to the external circuitry. Being the spurious resonance of the RB closer to $2f_1$, the field magnitudes inside the resonator at that fundamental frequency, f_1, will be also higher and consequently the level of the H2.

As it can be seen in figures 4.22 a and b, any material is a potential contributor for this anomalous peak. This initial analysis reveals the limitations of no considering the whole frequency range, on the unique identification of the nonlinear sources.

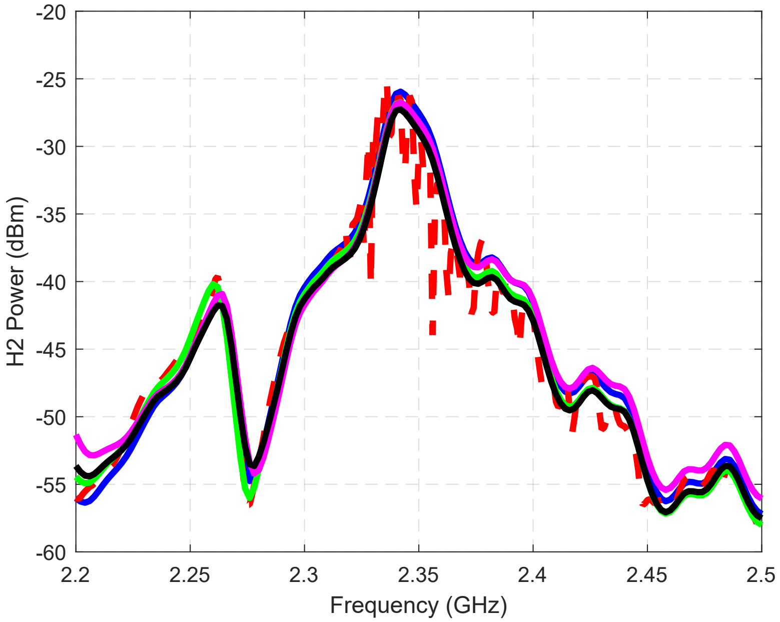

(a) RA

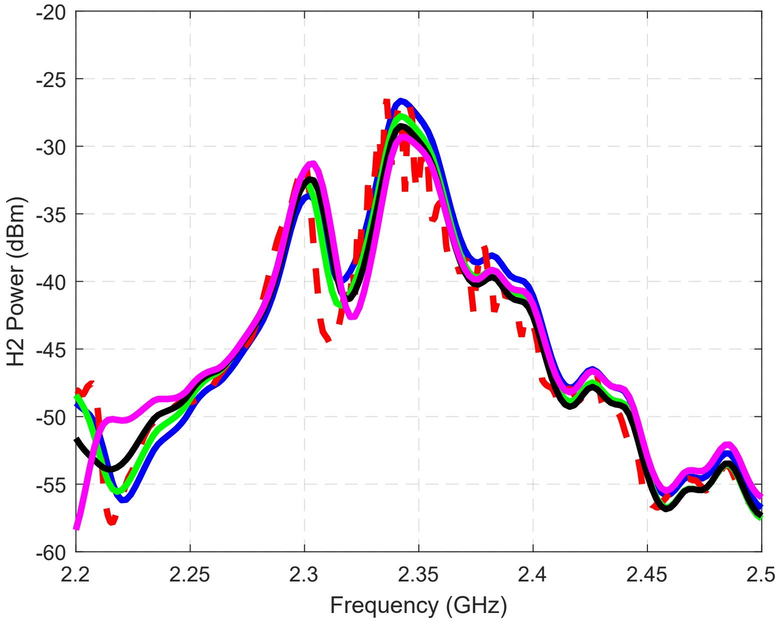

(b) RB

Figure 4.22: Narrowband H2 measurements and simulations. Measurements (dotted-red); $c^E_{2,AlN}$ (blue), $c_{2,W}$ (magenta), c_{2,SiO_2} (green), $c_{2,AlCu}$ (black).

Figure 4.23 shows the broadband H2 measurements for both resonators, when the fundamental tone is swept from 2.2 to 3.3 GHz. The input power was set to 20 dBm. Figure 4.23 depicts that the measured H2 frequency pattern significantly differs at higher frequencies, due to the variation of the field distribution along each of the stack layers. These features will be used to discern the origin of the nonlinearities, this is, the layer and material parameter.

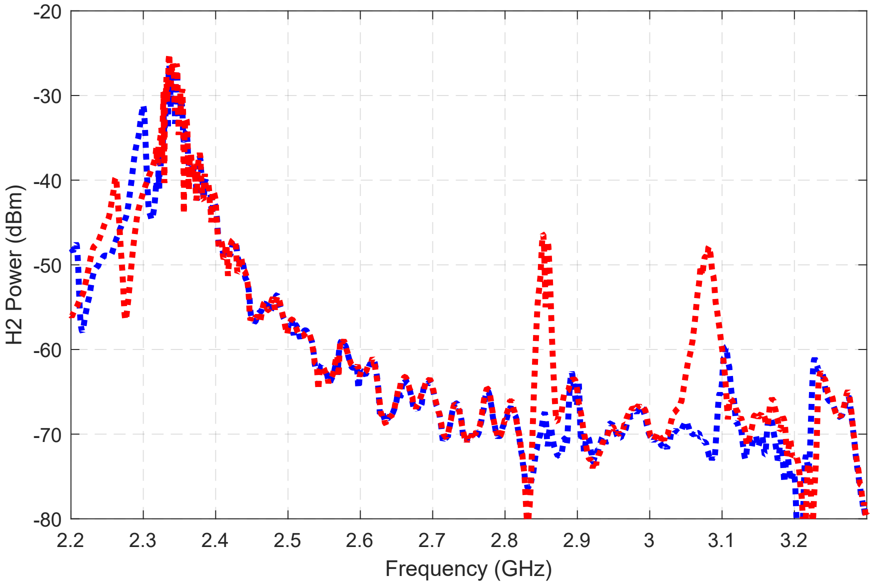

Figure 4.23: Broadband H2 response measured for RA(dotted blue)and RB (dotted red).

Figure 4.24 outlines the adjustment of the broadband H2 response for RA and RB for the nonlinear parameters of table 4.3. It is worth to mention that the term $\varepsilon_2^S = 20 \cdot \varepsilon^S \cdot e_{AlN}/c_{AlN}^E$ is considered in all the simulations. This term does not affect to the H2 peaks but it is required for a good matching out-of-resonances (for example between 2.4 GHz and 2.8 GHz), as it has been mentioned in the first experiment. Therefore, simulation and measurements reveal that the most accurate matching for these two resonators is achieved when nonlinearities are considered in the SiO_2 layers.

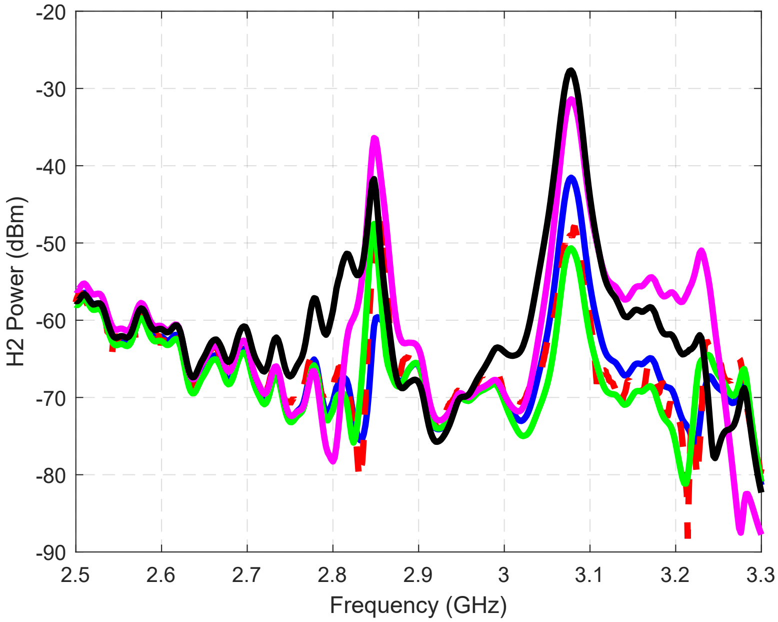

(a) RA

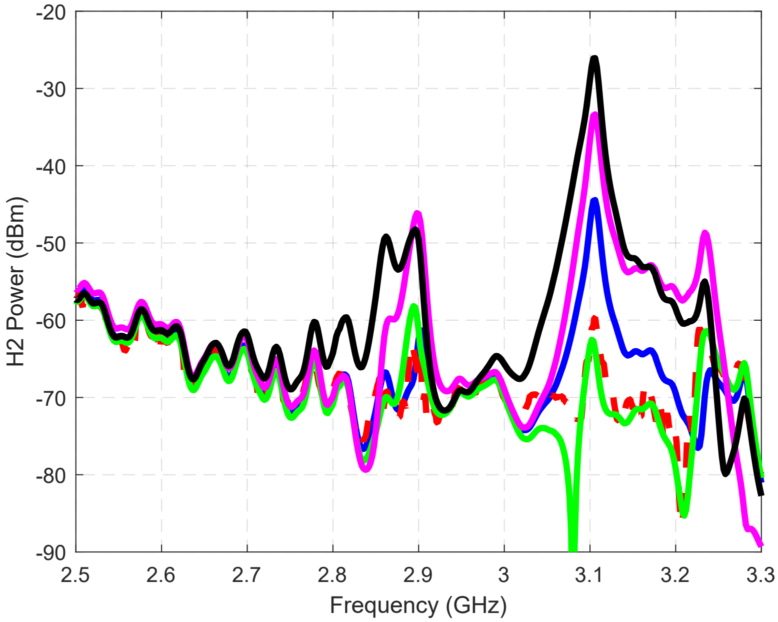

(b) RB

Figure 4.24: Broadband H2 measurements and simulations. Measurements (dotted-red); $c^E_{2,AlN}$ (blue), $c_{2,W}$ (magenta), c_{2,SiO_2} (green), $c_{2,AlCu}$ (black).

Simulations of the second harmonic considering the SiO_2 hypothesis have also been performed on the other resonators. The reason for that is simple: this confirms the contribution of SiO_2 layers on the generation of H2. Note that this statement was obtained from measurements of R5, RA and RB, and here is confirmed with additional simulations of R1, R2, R3, R4 and R6.

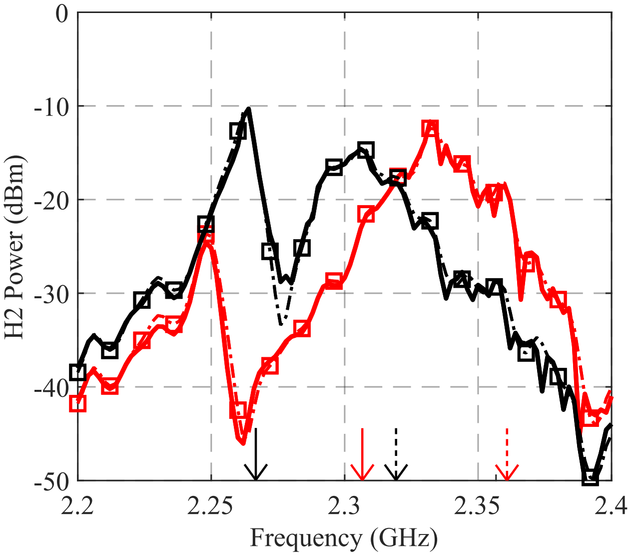

Figure 4.25: H2 measurements (thick lines) and simulations (dotted-dashed squared lines) for the B30 resonators. This includes R5 (red) and R6 (black). Continuous arrows (series resonance), dashed arrows (shunt resonance).

Figure 4.25 to figure 4.27 show how the second-order coefficients ($\varphi_5 = -18.7 \cdot e$, $\varepsilon_2 = 20 \cdot \varepsilon^S \cdot e/c^E$ and $c_{2,SiO_2} = -6.4 \cdot c_{SiO_2}$) explain with good agreement the H2 measurements of all the resonators. The input power level of the fundamental tone for these measurements is set to 25 dBm. As it is well known, the maximum H2 that appears between the series and shunt resonance (marked with arrows in the figures) is dominated by the term φ_5 for all the resonators.

The resonator R6 (as in the case of RA, RB and R5) shows too an anomalous high H2 peak at 2.26 GHz, just below their series resonances (2.33 GHz). This peak, as in the case of R5, RA and RB, is dominated by the second-order term of the elastic constant of the SiO_2 layers, c_{2,SiO_2}. At twice the high peak frequency (4.52 GHz) the generated H2 is enhanced by a high-order resonance. Note that this also demonstrates another time the usefulness of using a distributed model and the importance of having a good matching between simulations and measurements of the broadband linear response.

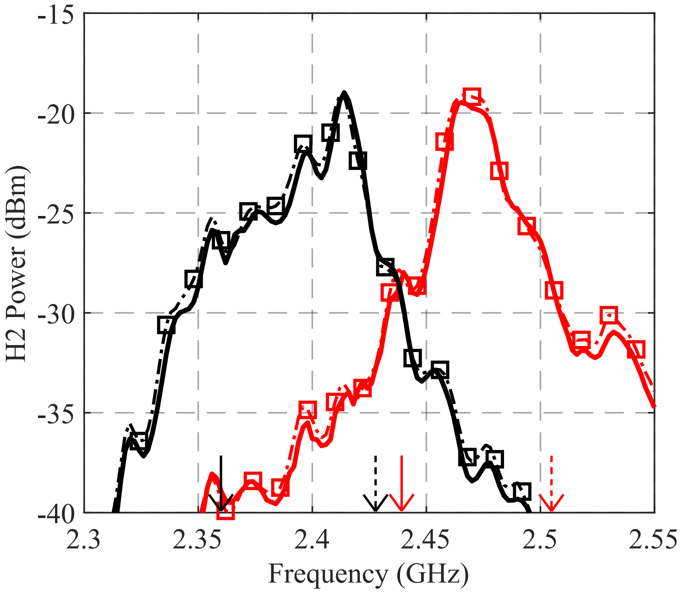

Figure 4.26: H2 measurements (thick lines) and simulations (dotted-dashed squared lines) for the Wi-Fi resonators. This includes R1 (red) and R2 (black). Continuous arrows (series resonance), dashed arrows (shunt resonance).

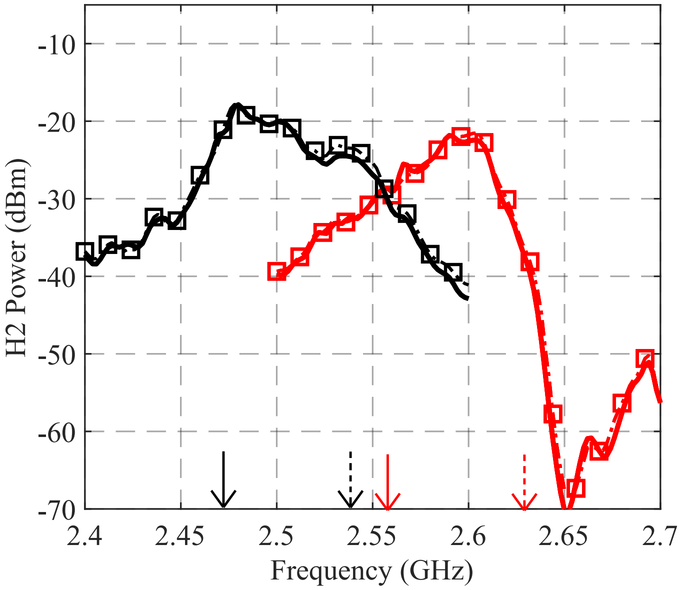

Figure 4.27: H2 measurements (thick lines) and simulations (dotted-dashed squared lines) for the B7 resonators. This includes R3 (red) and R4 (black). Continuous arrows (series resonance), dashed arrows (shunt resonance).

For an accurate agreement between measurements and simulations, the broadband measurement system effects have been included in all the simulations. The most common effect of the non-ideal measurement system is the ripple depicted in all the measurements and the reduction in the H2 output power at higher frequencies due to the limited bandwidth of the components used in the measurement system, which is specially relevant for the R3 resonator at frequencies higher than 2.6 GHz, as is depicted in figure 4.27.

4.6 Third-Order Nonlinear Characterization

The previous section has shown that the SiO_2 layers of the acoustic reflector may play a significant role on the generation of H2 in temperature-compensated resonators, where SiO_2 layers are thicker than in the nontemperature-compensated resonators. Full understanding of the origin of the nonlinear effects indeed requires the identification of all the sources contributing to the overall nonlinear manifestations.

To this aim, this section focuses on the third-order nonlinear manifestations, by performing a detailed characterization of H3 and IMD3 occurring in six different resonators (R1 - R6). The characterization process allows to identify the direct contribution and the remixing effects into the overall IMD3 and H3, and it provides a unique set of second- and third-order nonlinear constants of the AlN and SiO_2 that can explain all the measurements. Note that the fact of applying a unique model to emulate the behavior of several nonlinear manifestations and for different resonators supports the consistency and uniqueness of the solution.

4.6.1 IMD3 - Third-Order Nonlinear Response Analysis

The next step of the characterization consists on analyzing the IMD3 of all the resonators and discerns the contribution, if any, of the second-order nonlinear terms due to the remixing phenomena.

Figure 4.28(a) shows the measured IMD3 of the resonator R5 in thick red line. The x-axis corresponds to the central frequency of the two fundamental tones, i.e., $f_0 = (f_1 + f_2)/2$, which is swept from 2.2 to 2.4 GHz. These measurements correspond to the spurious signal at $2f_1 - f_2$, when the input power level of the two fundamental tones is set to 25 dBm and the frequency spacing between the two tones is kept to 10 MHz along the whole experiment.

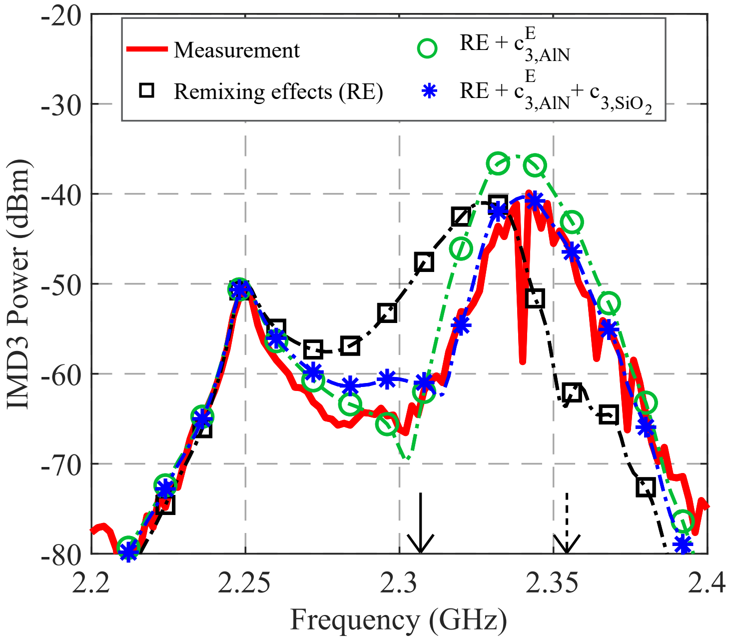

(a) R5

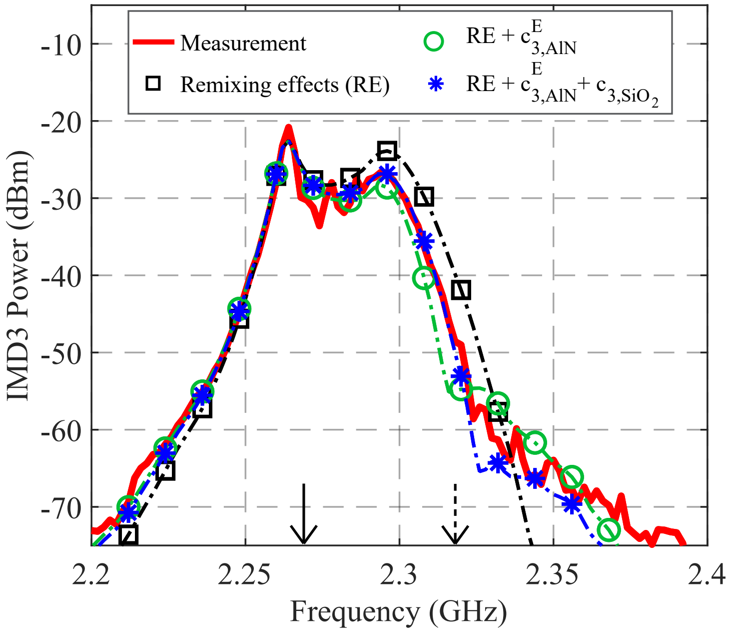

(b) R6

Figure 4.28: IMD3 ($2f_1 - f_2$) measurement and simulations for resonator R5 and R6. Continuous and dashed arrows indicate the series and shunt resonances respectively.

Figure 4.28(a) also shows, in squared dashed black line, the contribution to the IMD3 coming from the second-order nonlinear terms corresponding to AlN and SiO_2. Note that no additional third-order terms have been included. This IMD3 generation is coming from remixing effects, in which the second harmonics and IMD2 products in the two-tone experiment are remixed again with the fundamental signals producing IMD3 (see section 2.4.2 in chapter 2).

Therefore, third-order intermodulation products are coming from second-order nonlinear terms by remix of the second-order terms (φ_5'' and c_{2,SiO_2}) with the fundamental signals. But, as it could be observed in figure 4.28(a), remixing effects could not solely explain the measured IMD3 because in some frequency ranges the simulated IMD3 is higher than the measured value and in others lower. For sake of clarity, hereinafter the term φ_5'' will be named as φ_5.

For the R6 resonator, whose results are shown in figure 4.28(b), something similar happens and the simulated response overestimates the measurements at frequencies near the shunt resonance. Those experiments indicate that other nonlinear sources must exist beyond the remixing effects.

It is remarkable that the IMD3 for these R5 and R6 exhibit an additional peak, at 2.25 and 2.26 GHz respectively, below their series resonances. These peaks appear at the same frequencies than those appearing in their corresponding H2 (see figure 4.25). It is very likely then, that those peaks are generated by second-order remixing effects mainly due to the SiO_2 layers.

In contrast with the temperature-compensated resonators, the simulated IMD3 for resonators R1, R2, R3 and R4 due to remixing effects clearly underestimates the measured IMD3, as it is shown, in squared dashed black lines, in figures 4.29(a)-4.30(b). It is clear that the remixing phenomena cannot solely explain the IMD3 of all the resonators, enforcing again that other nonlinear sources have to exist.

Aluminum Nitride Third-Order Elastic Constant Role

In previous works based on SMR and BAW resonators [9], [10] and [12], it was stated that the IMD3 (with tone spacing large enough to avoid thermal effects) was due to the third-order stiffness constant of the AlN layer, $c_{3,AlN}^E$. Because the stack was different, the authors of these works did not entail the contribution of the SiO_2 layers on the nonlinearities and they postulated that the whole IMD3 was generated by a third-order nonlinear term $c_{3,AlN}^E =$

$-111 \cdot c^D_{AlN}$.

In this work, to identify the third-order nonlinear terms of the different layers that additionally could contribute to the IMD3, we start by assuming that only one layer contributes to the direct generation at a time. This is setting all third-order nonlinear constants to zero but one. We tested potential values of $c^E_{3,AlN}$, $c_{3,W}$, $c_{3,AlCu}$, etc., and note that for all these cases it is always considered the contribution of the remixing effect coming from the second-order terms of AlN and SiO_2. None of them adjusted all the measurements but the term $c^E_{3,AlN} = -110 \cdot c^D$ of the AlN layer.

This value, which completely agrees with the value previously reported in [9], [10] and [12], fits perfectly the IMD3 measured of the resonators R1, R2, R3 and R4, as it can be seen in green circles dashed lines in figures 4.29-4.30.

The simulated IMD3 of the R6 resonator (figure 4.28(b)) also presents a better fitting with the measurement when this term is included, lowering the IMD3 that the remixing effects overestimate. For the resonator R5, the adjustment of the IMD3 significantly improves (figure 4.28(a)) but including this term the IMD3 is overestimated by 5 dB around the resonance frequency.

To fully capture all the nonlinear contributors, we look for an additional direct contribution that could affect mainly to the R5 resonator and remain unchanged the IMD3 of the other resonators.

Silicon Dioxide Third-Order Elastic Constant Role

As it has been mentioned before, R5 and R6 have thicker layers of SiO_2 in comparison with the other resonators. Therefore, their third-order elastic constant is the best potential candidate. Adding a value of $c_{3,SiO_2} = 30 \cdot c_{SiO_2}$ the simulated IMD3 adjust the experimental data as it can be seen in blue asterisks dashed lines in figures 4.28(a) and 4.28(b).

Once identified this third-order nonlinear term, the other 4 resonators (R1, R2, R3 and R4) have been analyzed using the set of constants (φ_5, ε^S_2, c_{2,SiO_2}, $c^E_{3,AlN}$ and c_{3,SiO_2}). Figures 4.29(a)-4.30(b) show that this additional term has no impact at all into the IMD3 of those resonators, validating this hypothesis.

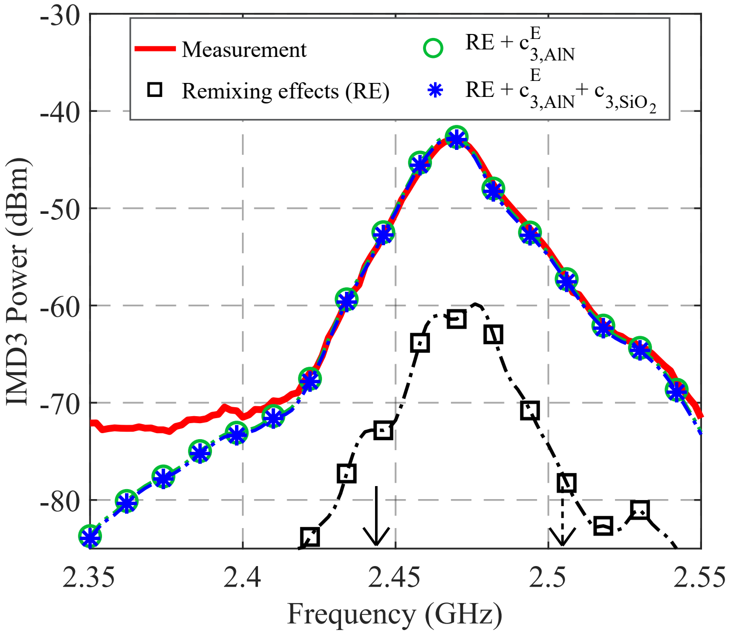

(a) R1

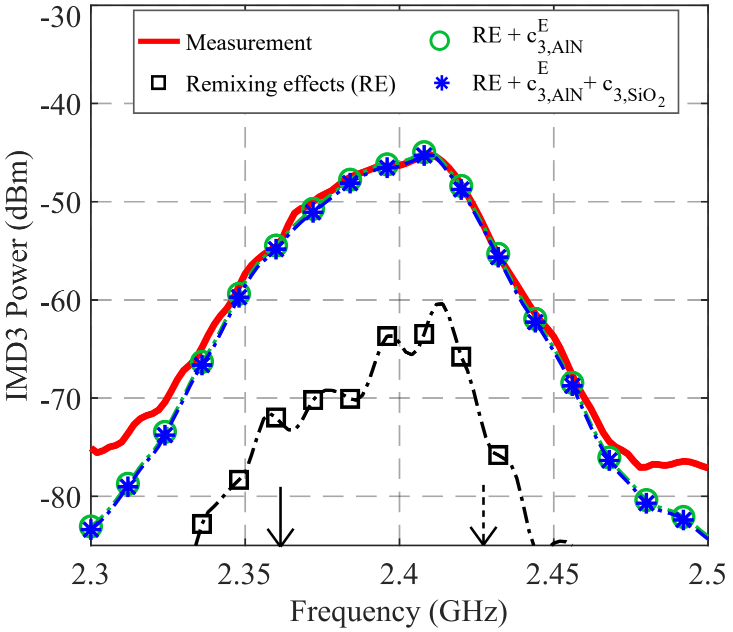

(b) R2

Figure 4.29: IMD3 ($2f_1 - f_2$) measurement and simulations for resonator R1 and R2. Continuous and dashed arrows indicate the series and shunt resonances respectively.

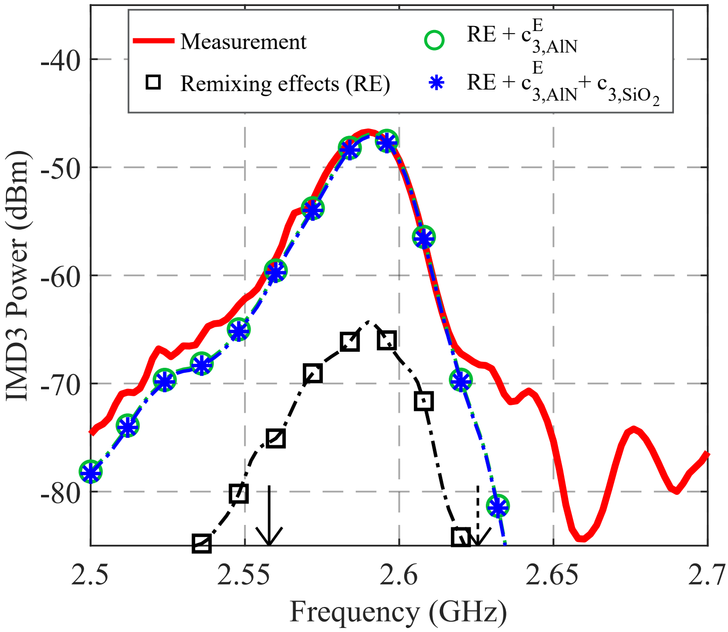

(a) R3

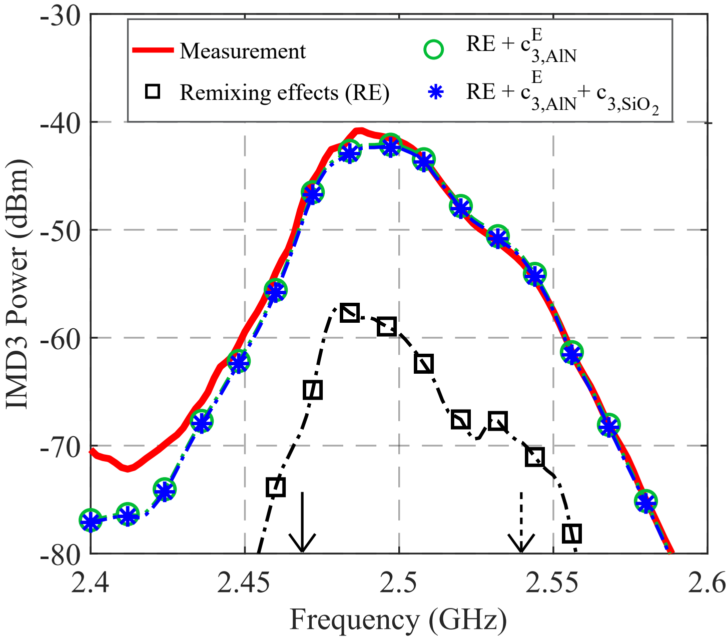

(b) R4

Figure 4.30: IMD3 ($2f_1 - f_2$) measurement and simulations for resonator R3 and R4. Continuous and dashed arrows indicate the series and shunt resonances respectively.

4.6.2 H3 - Third-Order Nonlinear Response Analysis

In previous works that stated the impact of the third-order elastic constant of the AlN layer in the IMD3 response, the H3 was not measured [9], [10] and [12]. For further confirmation of the hypothesis under consideration in this thesis, the H3 generation must be consistent with the set of nonlinear parameters described here.

Figures 4.31(a) and 4.31(b) compare the measured H3 (R5 and R6 respectively) with the simulated H3 due to remix effects (black squares) and the set of 5 parameters described previously (blue asterisks), where the x-axis represent the fundamental frequency, f_1.

It is clear that the H3 in the temperature-compensated resonators R5 and R6 is dominated by remixing effects. The lower frequency peaks appearing in figures 4.31(a) and 4.31(b) at 2.24 GHz and 2.26 GHz respectively, have the same origin that the peaks appearing at their counterparts H2 and IMD3. The highest peaks that appear at 2.27 GHz and 2.28 GHz for R5 and R6 respectively, are due to high-order resonances at 6.81 GHz and 6.84 GHz appearing in the linear response, and note that the H3 does not show a conventional frequency pattern with highest values around the resonance frequency; whereas a small hill appears around the resonance of R5, the H3 of R6 does not show remarkable values around its resonance frequency.

The measured H3 of the non-compensated resonators R1-R4 (figures 4.32(a)-4.33(b)) show a more conventional frequency pattern with maximum values around their resonance frequencies. The simulated H3 of these resonators have the same order of magnitude than the measurements when the third-order terms $c^E_{3,AlN}$ and c_{3,SiO_2} are considered (blue asterisks).

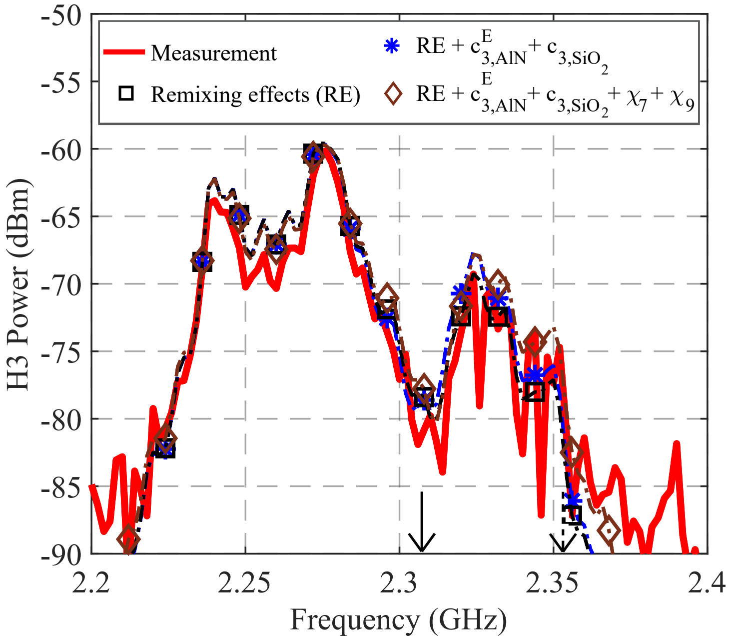

(a) R5

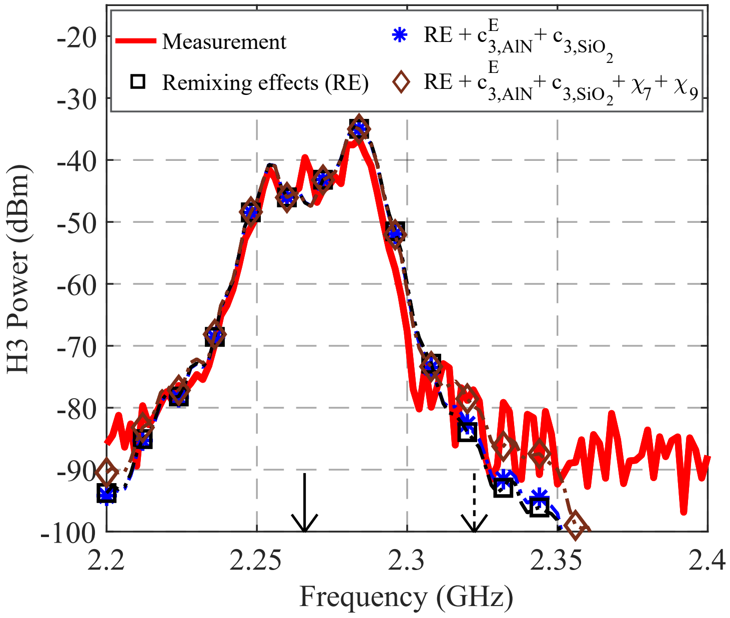

(b) R6

Figure 4.31: H3 ($3f_1$) measurement and simulations for the test resonators R5 and R6. Continuous and dashed arrows indicate the series and shunt resonances respectively.

Aluminum Nitride Role in H3 Generation

A better adjustment of the H3 of these four resonators can be achieved with the inclusion of additional third-order nonlinear constants $X_9 = 67 \cdot e$ and $X_7 = -4 \cdot 10^{-9}$ for the AlN layer (see equations (2.29) and (2.30)). The term X_9 is the extension up to a third-order of the term φ_5, which dominates the H2 generation around the resonance frequency, and it controls the maximum level of the H3 because X_9 multiplies S^3 in the ΔD equation (2.30). The term X_7 balances the frequency pattern at both edges of the resonance frequency since it always multiplies the electric field in ΔD and ΔT in equations (2.29) and (2.30).

Those two new terms X_9 and X_7 does not have an effect on the H3 of the R5 and R6 resonators (brown diamonds in figures 4.31(a) and 4.31(b)) since their H3 is dominated by remixing effects.

Table 4.4 summarizes all 7 nonlinear coefficients contributing to H2, H3 and IMD3 responses and their value. Finally, it is important to outline that the IMD3 response of all the resonators is not affected by these new two third-order terms. Simulations of IMD3 considering all the terms in Table 4.4 are not included in figures 4.28(a)-4.30(b) for the sake of clarity of the pictures since the simulated traces would overlap the blue asterisk traces.

This set of seven different nonlinear parameters have demonstrated, by performing a comprehensive characterization of 6 different BAW resonators, how they can reproduce with very good agreement all the nonlinear measurements presented in this work.

Table 4.4: Second- and third-order nonlinear coefficients for BAW resonators

Nonlinear coefficient	Value
φ_5	$-18.7 \cdot e$
ε_2	$20 \cdot \varepsilon^S \cdot e/c^E$
c_{2,SiO_2}	$-6.4 \cdot c_{SiO_2}$
$c^E_{3,AlN}$	$-110 \cdot c^D$
c_{3,SiO_2}	$30 \cdot c_{SiO_2}$
X_9	$67 \cdot e$
X_7	$-4 \cdot 10^{-9}$

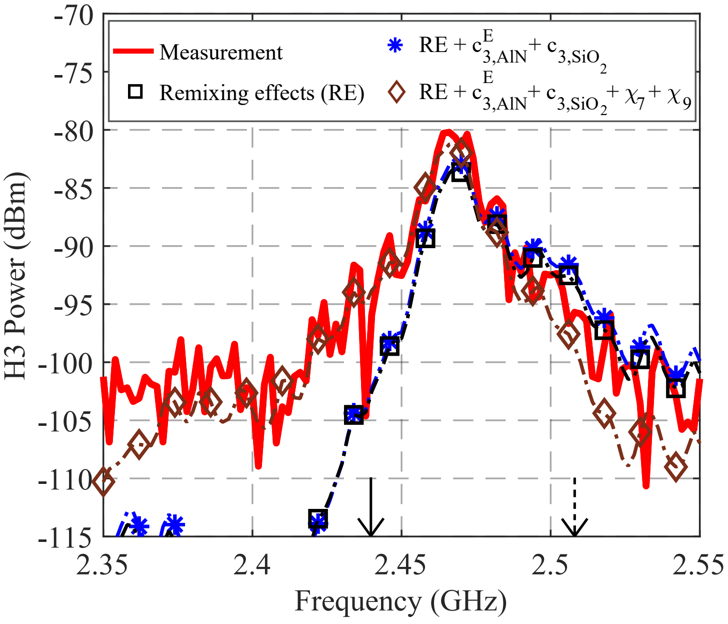

(a) R1

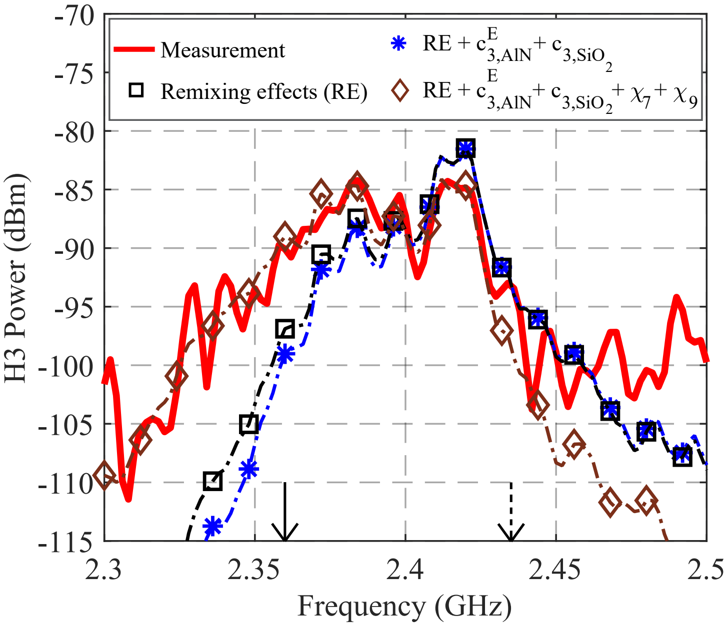

(b) R2

Figure 4.32: H3 ($3f_1$) measurement and simulations for the test resonators R1 and R2. Continuous and dashed arrows indicate the series and shunt resonances respectively.

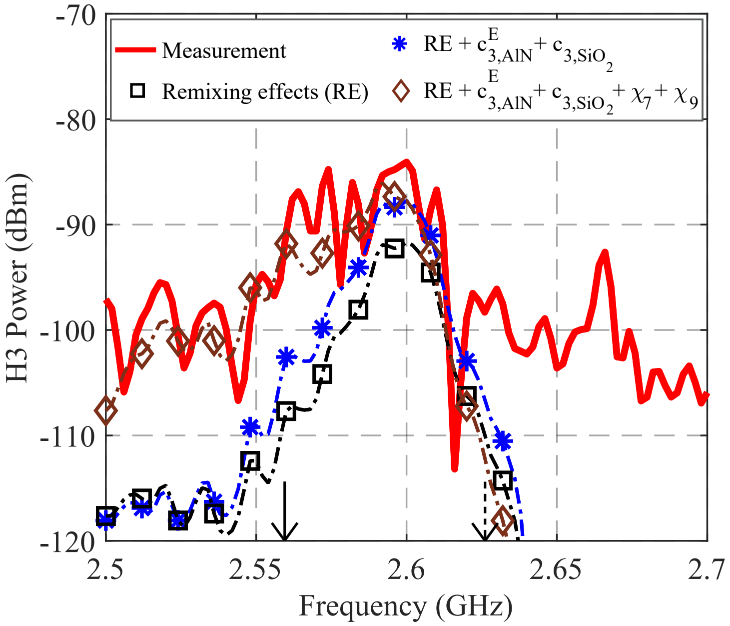

(a) R3

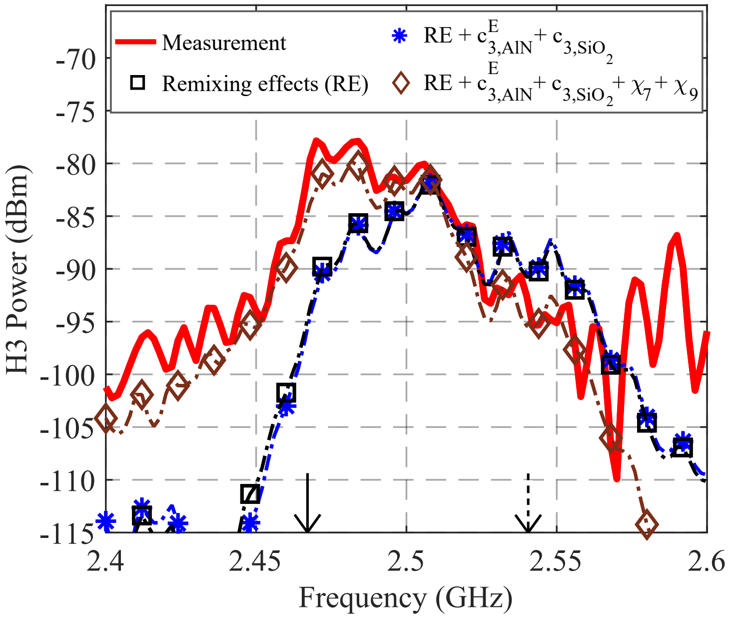

(b) R4

Figure 4.33: H3 ($3f_1$) measurement and simulations for the test resonators R3 and R4. Continuous and dashed arrows indicate the series and shunt resonances respectively.

4.6.3 Self-Heating Effects on TC-BAW Resonators

At this point, it is important to recall that the only material that has a positive nonlinear temperature-dependent coefficient φ_6, in equation 2.29 is the SiO_2. In TC resonators, SiO_2 thicknesses are designed in order to compensate the temperature derivative of the elastic constant of other layers. For this reason, SiO_2 layers are thicker than in other resonators, as it has been explained previously.

In this experiment, the central frequency of the two tones remains fixed at a given frequency, and the frequency spacing Δf between tones is swept, going from a few hertz up to 40 MHz. If the frequency spacing between tones is small (few tenths of kHz or less), the material is able to follow the dynamic variations of the temperature, changing the material properties that are temperature dependent. This experiment allows us to evaluate the IMD3 generation due to thermal effects (see section 2.4.5 in chapter 2).

First of all, we have measured the IMD3 of the resonator R5. The central frequency remains fixed at 2.33 GHz, frequency in which the intrinsic IMD3 is near to the maximum peak as seen in figure 4.34.

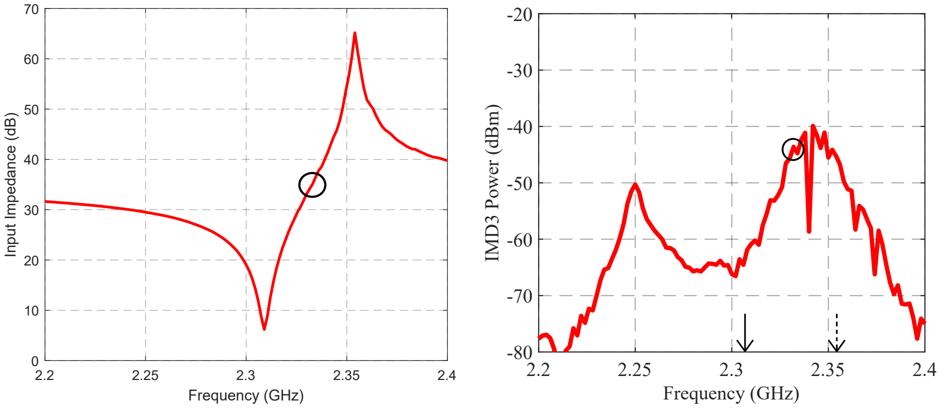

(a) Input Impedance

(b) IMD3 ($2f_1 - f_2$) Power

Figure 4.34: Measurements for resonator R5. Frequency of interest 2.33 GHz circled in both figures.

Figure 4.35 depicts the measured and simulated IMD3 (only the IMD3 at $2f_1 - f_2$ is shown for simplicity). The profile of the thermal RC network and its low-pass behavior can be clearly seen from few hertz$'$s up to 1 MHz. This indicates that the IMD3 comes from self-heating mechanisms. For tone spacing larger than 1 MHz, the IMD3 level generated by thermal effects is lower, and the intrinsic IMD3 dominates. The temperature derivatives considered for the AlN and for the other materials are shown in table 4.5 [12].

Table 4.5: Nonlinear thermal coefficients

Nonlinear coefficient	Value
$\varphi_{2,AlN}$	$195 \cdot 10^{-6} \cdot \varepsilon^{S\theta}$
$\varphi_{7,AlN}$	$10^{-6} \cdot e^{\theta}$
$\varphi_{6,AlN}$	$-119.4 \cdot 10^{-6} \cdot c^{E\theta}$
φ_{6,SiO_2}	$291.9 \cdot 10^{-6} \cdot c^{E\theta}$
$\varphi_{6,W}$	$-136.5 \cdot 10^{-6} \cdot c^{E\theta}$
$\varphi_{6,AlCu}$	$-727.5 \cdot 10^{-6} \cdot c^{E\theta}$

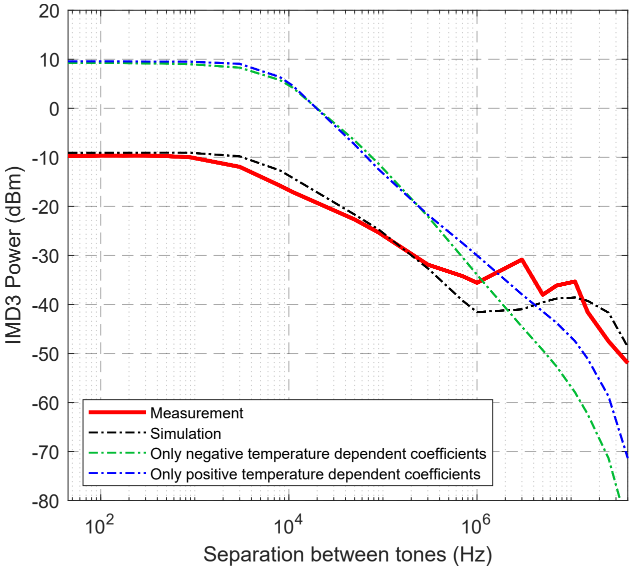

Figure 4.35: IMD3 $(2f_1 - f_2)$ measurement and simulations sweeping the separation between tones at the central frequency of 2.33 GHz for resonator R5.

Analyzing separately the IMD3 generated by thermal effects, this is, the IMD3 due to only the temperature-coefficient of the SiO_2 on one hand, and the one generated by all the other temperature derivatives on the other hand, it is observed that the simulated IMD3 levels are higher than the measured IMD3. It is clear then that the IMD3 due to thermal effects is canceled in the TC-BAW resonators. Note that designing the TC-BAW stack to compensate changes of the ambient temperature, does not necessarily implies that the IMD3 was canceled. The temperature profile through the stack of materials might be different for variations of the steady ambient temperature and for distributed heating sources (losses) through the stack.

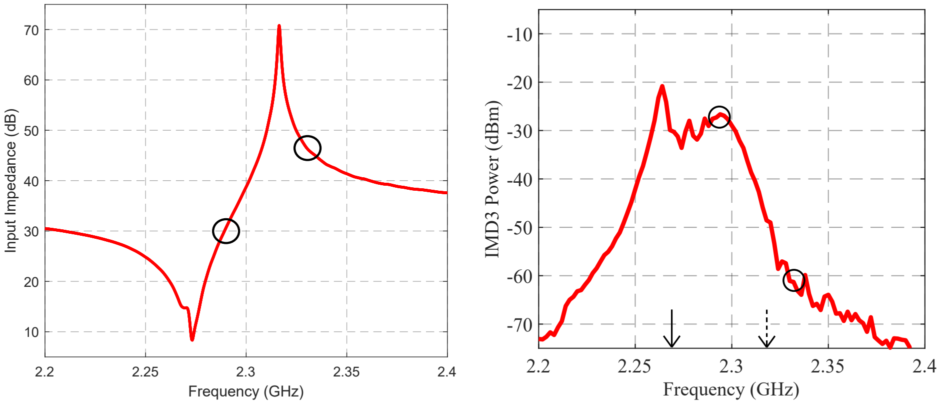

(a) Input Impedance (b) IMD3 ($2f_1 - f_2$) Power

Figure 4.36: Measurements for resonator R6. Frequencies of interest 2.29 and 2.33 GHz circled in both figures.

The same experiment has been carried out for the R6 resonator. The central frequency was fixed at 2.29 GHz and 2.33GHz, as is shown in figure 4.36. Figure 4.37(a) shows that the nonlinear temperature coefficients found in this work fits quite well the measurements also for this resonator. As in the R5 resonator, the isolated contribution of the SiO_2 and the other materials overestimates the measured IMD3. The cancellation in this case is even higher than in the previous case, being more than 30 dB. Figure 4.37(b) shows the IMD3 response for the R6 resonator when the central frequency is set up at 2.33 GHz (close to its shunt resonance). In that case, the measured IMD3 is 20 dB lower than in the previous case but still the cancellation effect is significant.

These simulations confirm that the SiO_2 layers, besides helping to avoid frequency shift in the linear response due to temperature changes, also could cancel the thermal IMD3 signals generated in the AlN layer.

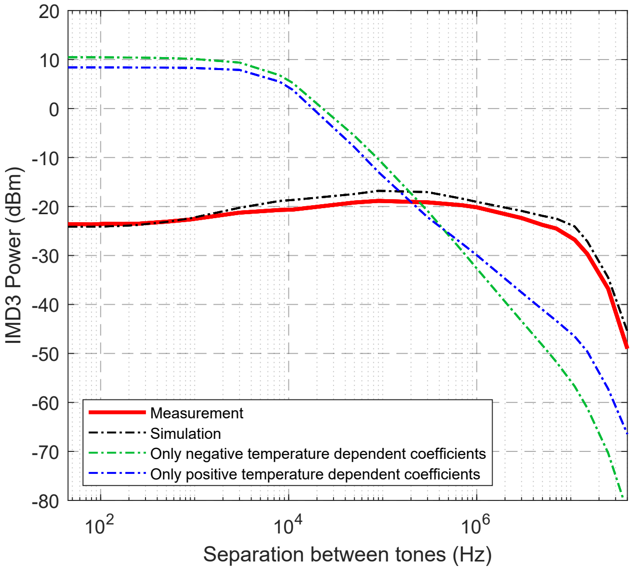

(a) $f_0 = 2.29GHz$

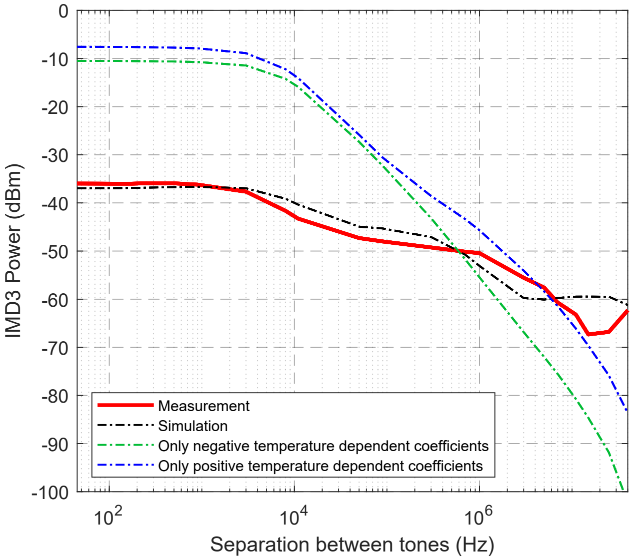

(b) $f_0 = 2.33GHz$

Figure 4.37: IMD3 ($2f_1 - f_2$) measurement and simulations sweeping the separation between tones at the central frequency of 2.29 GHz and 2.33 GHz for resonator R6.

4.7 Concluding Remarks

This chapter has presented the methodology for performing the nonlinear characterization procedure for BAW resonators. To guarantee a unique and comprehensive solution of the nonlinear behavior of BAW devices we could conclude that the main steps required are:

- The use of a distributed circuit model that accounts for the field and nonlinear sources distribution at each layer forming the resonator.
- Broadband measurements of the nonlinear response in order to obtain clues about the origin of the nonlinearities.
- Measurements of different resonators with different characteristics and layer thicknesses. All the measurements must be consistent with a unique set of nonlinear parameters.

This procedure is very useful and provides an accurate methodology to discern between the different materials involved in the nonlinear generation.

In order to do that, different nonlinear measurements of different resonators must be done. So, nonlinear measurement systems, being able to measure the different spurious signals for the different working frequency range of the resonators, must be designed and assembled in the laboratory. Here two different measurement systems have been presented: one for measuring the H2, and the second for measuring the third-order spurious signals, IMD3 and H3. These measurement systems, by making measurements of the S-Parameters, the power supplied to the DUT, and the degree of nonlinearities generated by the own system, have demonstrated to be valid for measuring the resonators under study.

Eight different resonators have been measured. Those resonators, designed for working at different frequency bands, are good candidates for a unique and comprehensive nonlinear characterization of BAW resonators, and study which materials produce some degree on nonlinear behavior.

The second part of this chapter, concludes that an accurate characterization requires of a broadband characterization of the linear response and a broadband characterization of the H2.

Unexpected H2 peaks may appear at some frequencies in TC-BAW. When the device is driven at a frequency close to the resonance frequency, such that an out-of-band resonance exists at twice that frequency, the resonating conditions enhance the H2 and the output H2 power may become significant. For the particular stack studied in this paper, we have unambiguously demonstrated that the SiO_2 layers below the bottom electrode are responsible for this effect by three different experiments: narrowband H2, broadband H2, and DC detuning. Once the origin of this anomalous effect is well established, it might be corrected by modifying the design of the Bragg reflector and electrodes slightly to avoid out-of-band resonances close to twice the main resonance.

The H2 experiments were also consistent with linear measurements of the input impedance of the resonator under a DC bias voltage. We also provide new closed form expressions which agree perfectly with the nonlinear simulations.

The third and last part of this chapter outlined on the major contributors into the nonlinear spurious manifestations at IMD3 and H3. The characterization process consists on a systematic procedure that allows to identify the different sources contributing to the nonlinear manifestation by sequentially adding different nonlinear contributors. This starts by the second-order nonlinear terms that explain the H2 values. Note that those terms also contribute to the H3 and IMD3 manifestations through a remixing phenomena. In particular, the role of the SiO_2 layers through the term c_{2,SiO_2} is crucial for the generation of IMD3 and H3 in the temperature-compensated resonators.

For the non-compensated resonators, our experiments confirm that the IMD3 around resonance is dominated by the term $c^E_{3,AlN}$. However, the H3 is dominated by remixing effects due to φ_5 and c_{2,SiO_2}, and two additional third-order terms (X_7 and X_9) have been included for a better adjustment of the H3 of all the resonators. These two additional terms do not affect to the IMD3 but additional measurements (other resonators and/or other experiments) should be performed to guarantee the uniqueness and consistence of the solution including these terms. Note that the fact of applying a unique model to emulate the behavior of several nonlinear manifestations and for different resonators supports the consistency and uniqueness of the solution.

Table 4.6 summarizes all 7 intrinsic nonlinear coefficients contributing to H2, H3 and IMD3 responses and their value.

Finally, this chapter demonstrates how SiO_2 layers, besides help to avoid frequency shift in the linear response due to temperature changes, also could cancel the IMD3 signals generated in the AlN layer by self-heating mechanisms, improving the performance of the resonators.

Table 4.6: Nonlinear coefficients and their manifestations

Nonlinear coefficient	Value	
φ_5	$-18.7 \cdot e$	H2 around resonance frequency
ε_2	$20 \cdot \varepsilon^S \cdot e/c^E$	H2 out of the resonance frequency
c_{2,SiO_2}	$-6.4 \cdot c_{SiO_2}$	H2 around resonance frequency and spurious peaks at higher frequencies
$c^E_{3,AlN}$	$-110 \cdot c^D$	IMD3 and H3 around resonance frequency
c_{3,SiO_2}	$30 \cdot c_{SiO_2}$	IMD3 and H3 around resonance frequency
$X9$	$67 \cdot e$	IMD3 and H3 around resonance frequency
$X7$	$-4 \cdot 10^{-9}$	IMD3 and H3 around resonance frequency

Chapter 5

Conclusions and Future Research Lines

5.1 Conclusions

As a general conclusion of this work, we can remark that we succeed with the objective and the different sub-objectives defined in the introduction, by designing properly nonlinear measurement systems and defining a systematic nonlinear characterization process by using different nonlinear models for AW technology.

The conclusions achieved with this work, listed for each chapter, are:

- Chapter 4 has emphasized in all the nonlinear characterization procedure for BAW resonators, presenting a comprehensive methodology for performing it. This methodology allows us to discern between the different materials involved in the nonlinear generation.

  One important step when characterizing nonlinear devices is to properly design nonlinear measurement systems. Those measurement systems must be able to measure nonlinearities of the different resonators under study in this dissertation, working in different frequency ranges. This work has proposed two different measurement systems: one for measuring the H2, and the second one for measuring IMD3 and H3. Those measurement systems have demonstrated to be valid for measuring the resonators under study here. This work has focused on eight different resonators, designed for working at different frequency bands, by using the same stack configuration, at the same time that they differ in their layer thicknesses, and other characteristics (four of them are TC-BAW resonators). This makes them good candidates for the nonlinear characterization procedure.

An accurate characterization and modeling of the H2 nonlinear response has been realized. Unexpected H2 peaks appearing at some frequencies in TC-BAW could give us clues about the origin of this undesired signal and the material generating it. It has been demonstrated that the SiO_2 layers below the bottom electrode are responsible for this effect. This conclusion has been possible thanks to three different experiments: narrowband H2, broadband H2, and DC detuning.

This chapter has outlined too on the major contributors into the IMD3 and H3 generation. The characterization process consists on a systematic procedure that allows to identify the different sources contributing to the nonlinear manifestation by sequentially adding different nonlinear contributors. This starts by the second-order nonlinear terms that explain the H2 values. Note that those terms also contribute to the H3 and IMD3 manifestations through a remixing phenomena. In particular, the role of the SiO_2 layers through the term c_{2,SiO_2} is crucial for the generation of IMD3 and H3 in the temperature-compensated resonators. It is also confirmed that the IMD3 around resonance is dominated by the term $c^E_{3,AlN}$. However, the H3 is dominated by remixing effects due to φ_5 and c_{2,SiO_2}, and two additional third-order terms (X_7 and X_9) have been included for a better adjustment of the H3 of all the resonators. These two additional terms do not affect to the IMD3.

Finally, this chapter demonstrates how SiO_2 layers, besides help to avoid frequency shift in the linear response due to temperature changes, also could cancel the IMD3 signals generated in the AlN layer, improving the performance of the resonators.

5.2 Future Research Lines

Although this thesis has achieved the goals defined, the work developed here is the starting point for design and manufacture a new generation of BAW devices with improved linear behavior. Therefore, the future work identified for this work is listed as follows:

- Define a procedure to tune the material properties that form the reflector of an SMR resonator. Materials forming the Bragg Mirror are a source of nonlinear distortion and contribute to degradation of the Q factor. If all of their undesired contributions are clearly identified, the next step is to define different procedures to tune those materials in order to improve both, linear and nonlinear responses.

- Study and identify new materials for improving the nonlinear response of BAW devices. It has been demonstrated how some materials could help to improve both linear and nonlinear responses. The SiO_2 layers, for example, help avoiding the frequency shifting with temperature changes, or help reducing around resonance frequencies the IMD3 generated by intrinsic properties of the material and/or self-heating effects due to temperature changes. New materials must be studied in order to identify if they could be good candidates for improving linear and nonlinear behavior of BAW devices.

- Characterize more complex structures based on BAW technology, such as filters and multiplexers (MUX). Once the nonlinear characterization procedure of BAW resonators has been done, this opens the possibility of study the nonlinear impact of those devices when forming more complex acoustic structures. For example, high-power signals feeding the filter input in multiplexers, can generate intermodulation and harmonics coming back to other filters input. If the spurious signal frequency falls on the in-band of the operating filter, interference and degradation on the QoS would occur. Reduce their impact on the overall communication chain is the next step, once the understanding of the origin of this signals has been achieved.

- Design new resonators and filters with optimized performance: nonlinearities and quality factor. With all material properties characterized and undesired contributions clearly identified, new resonators and filters can be designed in order to improve the linear response in these devices.

Appendices

Appendix A

List of Author's Contributions

This Ph.D. thesis has contributed to develop the tasks "T1. Modelado y diseño de resonadores" and "T3. Electrical characterization of resonators and sensors", of the TEC2017-84817-C2-2 project: "Sensores gravimétricos de gases basados en resonadores electro-acústicos de película delgada de AlN piezoeléctrico", project supported by the Spanish Government. With the support, in part, by the Universities and Research Secretary of the Generalitat de Catalunya, and in part by the European Social Fund under Grant 2018FI_ B_ 00448 and Grant 2017 SGR 813.

Besides, this thesis has been realized in collaboration with the US company Qorvo Inc. that provided the samples and has supervised this work.

A.1 Research Contributions

The different novelties of this Ph.D. dissertation have been published in several research contributions. The total number of publications are 2 journal papers, 6 conference papers and 1 patent.

Journal Papers

- D. Garcia-Pastor, C. Collado, J. Mateu and R. Aigner, "Third Harmonic and Intermodulation Distortion in Bulk Acoustic Wave Resonators", in *IEEE Transactions on Microwave Theory and Techniques*, pp. 1-8, 2019.

- C. Collado, J. Mateu, D. Garcia-Pastor, R. Perea-Robles, A. Hueltes, S. Kreuzer and R. Aigner, “Nonlinear Effects of SiO_2 Layers in Bulk Acoustic Wave Resonators”, in *IEEE Transactions on Microwave Theory and Techniques*, vol. 66, no. 4, pp. 1773-1779, April 2018.

Conference Papers

- C. Udaondo, C. Collado, J. Mateu and D. Garcia-Pastor, “An Equivalent Model for Lateral Modes on the H2 Response of Bulk Acoustic Wave Resonators”, in *2020 IEEE International Ultrasonics Symposium (IUS)*, Las Vegas (United States of America), 2020.
- D. Garcia-Pastor, C. Collado, J. Mateu and R. Aigner, “Role of SiO_2 Layers in Third-Order Nonlinear Effects of Temperature Compensated BAW Resonators”, in *2019 IEEE International Ultrasonics Symposium (IUS)*, Glasgow (United Kingdom), 2019.
- D. Garcia-Pastor, J. Mateu, C. Collado, R. Perea-Robles, M. Gonzalez-Rodriguez and J. M. Gonzalez-Arbesu, “Comprehensive Nonlinear Characterization and Modelling of a BAW Duplexer”, in *2019 IEEE/MTT-S International Microwave Symposium - IMS*, Boston (USA), 2019, pp. 857-860.
- R. Perea-Robles, D. Garcia-Pastor, J. Mateu, C. Collado and R. Aigner, “Fast Procedure for the Nonlinear Analysis of BAW Resonators”, in *2018 IEEE International Ultrasonics Symposium (IUS)*, Kobe (Japan), 2018, pp. 1-4.
- J. Mateu, C. Collado, A. Hueltes, R. Perea-Robles, D. Garcia-Pastor, M. Gonzalez-Rodriguez and J. M. Gonzalez-Arbesu, “Outline Process from the synthesis towards the nonlinear modeling of Bulk Acoustic Wave Filters”, in *2018 IEEE/MTT-S International Microwave Symposium - IMS*, Philadelphia (USA), 2018, pp.413-416.
- D. Garcia-Pastor, M. Gonzalez-Rodriguez, A. Hueltes, C.Collado, J. Mateu, S. Kreuzer and R. Aigner, “Nonlinear Effects of Electrode and Bragg Reflector Materials in BAW Resonators”, in *2017 IEEE International Ultrasonics Symposium (IUS)*, Washington (USA), 2017, pp. 1-4.

Patents

- C. Collado, J. Mateu, J. M. Gonzalez-Arbesu, A. Hueltes, M. Gonzalez-Rodriguez, D. Garcia-Pastor and R. Perea-Robles, "Método y sistema de medida de parámetros eléctricos de dispositivos de radiofrecuencia bajo condiciones de alta potencia", ES 2684570 A1, 2017-03-31.

A.2 Academic Contributions

This Ph.D. thesis has contributed to the academic environment with the realization of 2 bachelor's degree final thesis.

Bachelor's Degree Final Thesis

- A. Castan, *Simulations of Harmonics and Intermodulation Products in BAW Resonators Based on FDD Components*, Advisors: D. Garcia-Pastor, J. Mateu, September 2018.
- D. Paniagua, *Diseño y Fabricación de filtros paso bajo tubulares*, Advisors: C. Collado, D. Garcia-Pastor, July 2017.

Appendix B

Physical properties of the materials forming the stack of BAW resonators

This appendix presents in two different tables the physical properties of the materials forming the stack of the eight different resonators under study in this work. Table B.1 details the physical parameters of the *AlN* used as the piezoelectric layer. On the other hand, the physical properties of the non-piezoelectric materials forming the resonator stack, are shown in table B.2.

Table B.1: Physical properties of *AlN*

Table B.2: Physical properties of non-piezoelectric materials

Bibliography

[1] M. Experts, “Rf front ends for mobile devices 2017,” Tech. Rep., June 2017.

[2] Navian, “Focusing on front end modules for cellular terminals,” Tech. Rep., Nov. 2016.

[3] V. Chauhan, C. Huck, A. Frank, W. Akstaller, R. Weigel, and A. Hagelauer, “Enhancing RF bulk acoustic wave devices: Multiphysical modeling and performance,” *IEEE Microwave Magazine*, vol. 20, no. 10, pp. 56–70, oct 2019.

[4] R. Ruby, “A snapshot in time: The future in filters for cell phones,” *IEEE Microwave Magazine*, vol. 16, no. 7, pp. 46–59, aug 2015.

[5] S. Sethi, “Fbar gets excellent reception,” The Linley Group, Mobile Chip Report, Tech. Rep., July 2015.

[6] J. Verdu Tirado, “Bulk acoustic wave resonators and their application to microwave devices,” Ph.D. dissertation, Universitat Autonoma de Barcelona, 2010.

[7] Y. Cho and J. Wakita, “Nonlinear equivalent circuits of acoustic devices,” in *1993 Proceedings IEEE Ultrasonics Symposium.* IEEE, 1993.

[8] C. Collado, E. Rocas, J. Mateu, A. Padilla, and J. O. Callaghan, “Nonlinear distributed model for bulk acoustic wave resonators,” *IEEE Transactions on Microwave Theory and Techniques*, vol. 57, no. 12, pp. 3019–3029, dec 2009.

[9] D. S. Shim and D. A. Feld, “A general nonlinear mason model of arbitrary nonlinearities in a piezoelectric film,” in *2010 IEEE International Ultrasonics Symposium.* IEEE, oct 2010.

[10] ——, “A general nonlinear mason model and its application to piezoelectric resonators,” *International Journal of RF and Microwave Computer-Aided Engineering*, vol. 21, no. 5, pp. 486–495, jul 2011.

[11] W. P. Mason, *Piezoelectric Crystals and Their Application to Ultrasonics.* Princeton, NJ: Van Nostrand, 1950.

[12] E. Rocas, C. Collado, J. Mateu, N. Orloff, J. Booth, and R. Aigner, “Electro-thermo-mechanical model for bulk acoustic wave resonators,” *IEEE Transactions on Ultrasonics, Ferroelectrics and Frequency Control*, vol. 60, no. 11, pp. 2389–2403, nov 2013.

[13] E. D. Daniel Royer, *Elastic Waves in Solids I.* Springer Berlin Heidelberg, 1999.

[14] ——, *Elastic Waves in Solids II.* Springer-Verlag GmbH, 1999.

[15] J. Rosenbaum, *Bulk Acoustic Wave Theory and Devices.* ARTECH HOUSE INC, 1988.

[16] B. A. Auld, *Acoustic Fields and Waves in Solids, Volume I.* John Wiley & Sons, 1973.

[17] ——, *Acoustic Fields and Waves in Solids, Volume II.* John Wiley & Sons, 1973.

[18] E. Rocas, C. Collado, N. Orloff, and J. C. Booth, “Third-order intermodulation distortion due to self-heating in gold coplanar waveguides,” in *2010 IEEE MTT-S International Microwave Symposium.* IEEE, may 2010.

[19] R. Hooke, *Lectures de Potentia Restitutiva*, J. Martyn, Ed., 1678.

[20] K. ya Hashimoto, *Rf Bulk Acoustic Wave Filters for Communications.* Artech House, 2009.

[21] N. B. C. Jose Carlos Pedro, *Intermodulation Distortion in Microwave and Wireless Circuits*, A. House, Ed., 2003.

[22] D. M. Pozar, *Microwave Engineering.* John Wiley & Sons Inc, 2011.

[23] E. Rocas, C. Collado, N. D. Orloff, J. Mateu, A. Padilla, J. M. OCallaghan, and J. C. Booth, “Passive intermodulation due to self-heating in printed transmission lines,” *IEEE Transactions on Microwave Theory and Techniques*, vol. 59, no. 2, pp. 311–322, feb 2011.

[24] K. Lakin, “Thin film resonator technology,” *IEEE Transactions on Ultrasonics, Ferroelectrics and Frequency Control*, vol. 52, no. 5, pp. 707–716, may 2005.

[25] M.-A. Dubois, P. Muralt, H. Matsumoto, and V. Plessky, “Solidly mounted resonator based on aluminum nitride thin film,” in *1998 IEEE Ultrasonics Symposium. Proceedings (Cat. No. 98CH36102).* IEEE, 1998.

[26] K. Lakin, K. McCarron, and R. Rose, “Solidly mounted resonators and filters,” in *1995 IEEE Ultrasonics Symposium. Proceedings. An International Symposium.* IEEE, 1995.

[27] M.-A. Dubois, P. Muralt, and V. Plessky, “BAW resonators based on aluminum nitride thin films,” in *1999 IEEE Ultrasonics Symposium. Proceedings. International Symposium (Cat. No.99CH37027).* IEEE, 1999.

[28] S. Marksteiner, J. Kaitila, G. Fattinger, and R. Aigner, “Optimization of acoustic mirrors for solidly mounted BAW resonators,” in *IEEE Ultrasonics Symposium, 2005.* IEEE, 2005.

[29] R. Aigner, J. Ella, H.-J. Timme, L. Elbrecht, W. Nessler, and S. Marksteiner, “Advancement of MEMS into RF-filter applications,” in *Digest. International Electron Devices Meeting,.* IEEE, 2002.

[30] K. V. Dyke, “The piezo-electric resonator and its equivalent network,” *Proceedings of the IRE*, vol. 16, no. 6, pp. 742–764, jun 1928.

[31] J. Larson, P. Bradley, S. Wartenberg, and R. Ruby, “Modified butterworth-van dyke circuit for FBAR resonators and automated measurement system,” in *2000 IEEE Ultrasonics Symposium.* IEEE, 2000.

[32] V. M. Ristic, *Principles of acoustic devices*, . John Wiley & Sons Australia, Limited, Ed., 1983.

[33] D. A. Feld, D. S. Shim, S. Fouladi, and F. Bayatpur, “Advances in nonlinear measurement and modeling of bulk acoustic wave resonators (invited),” in *2014 IEEE International Ultrasonics Symposium.* IEEE, sep 2014.

[34] C. Collado, E. Rocas, A. Padilla, J. Mateu, J. M. O’Callaghan, N. D. Orloff, J. C. Booth, E. Iborra, and R. Aigner, “First-order elastic nonlinearities of bulk acoustic wave resonators,” *IEEE Transactions on*

Microwave Theory and Techniques, vol. 59, no. 5, pp. 1206–1213, may 2011.

[35] J. Mateu, C. Collado, O. Menéndez, and J. M. O'Callaghan, "A general approach for the calculation of intermodulation distortion in cavities with superconducting endplates," *Applied Physics Letters*, vol. 82, no. 1, pp. 97–99, jan 2003.

[36] "Bulk acoustic wave resonator with improved lateral mode suppression," U.S. Patent US6 215 375B1, April 2001.

[37] A. Link, E. Schmidhammer, H. Heinze, M. Mayer, B. Bader, and R. Weigel, "Appropriate methods to suppress spurious FBAR modes in volume production," in *2006 IEEE MTT-S International Microwave Symposium Digest.* IEEE, 2006.